THE UNIVERSITY *of* EDINBURGH

Modelling Nanoscale Kinetics of Radiation Damaged Surfaces

Terri Amos

Doctor of Philosophy
The University of Edinburgh
2014

Abstract

Materials in nuclear reactors and satellites experience continually damaging radiation which leads to their degradation over time. Currently, a materials safe working lifetime within these environments is estimated with a large, costly, safety margin. The work of this thesis aims to improve the usefulness of an optical technique known as reflection anisotropy spectroscopy (RAS), which once fully characterised could allow materials to be actively monitored in such environments.

The intrinsic optical anisotropy of the Cu(110) surface has been exploited to study nanoscale kinetics of ion bombarded surfaces. Within the Cu(110) RA spectrum the 2.1eV peak is particularly sensitive to surface defects and largely unaffected by the bulk of the substrate. Using the Poelsema-Comsa model (which assumes defects scatter surface electronic states within a patch centred on the defect) it can be demonstrated that at finite temperatures the decay of the 2.1eV peak contains information relating to the diffusion of surface defects. A kinetic Monte Carlo simulation has been created to model the destruction of this peak and allows further understanding of the diffusion processes involved.

The decay of the 2.1eV peak with ion bombardment has been successfully modelled for a range of temperatures using experimental RAS data for comparison. Through a novel way of analysing RAS data, it has been shown that the total scattering cross section per ion impact decreases with bombardment time, which it is believed to be due to surface diffusion. This could give a novel way of measuring surface diffusion directly from RAS measurements.

Clustering of ion induced surface defects has been analysed and the results found are consistent with STM images of the same surface obtained 30 minutes after bombardment. While molecular dynamics calculations have previously attempted to predict the surface topology and defect clustering nanoseconds after impact, using a kinetic Monte Carlo simulation improves on this, demonstrating that

diffusion on long time scales (currently inaccessible using molecular dynamics calculations) play an important role in predicting nano-surface topology.

2.1eV peak recovery after surface damage by ion bombardment was also investigated. The peak was found to recover at finite temperatures, which is also seen in experimental data. It was concluded that the surface diffusivity values in the literature are too high and a new value for diffusivity has been calculated by comparing simulation and experimental data.

Lay Summary

Materials in nuclear reactors and satellites experience continually damaging radiation which leads to their degradation over time. Currently, a material's safe working life time within these environments is estimated with a large, costly, safety margin. The work of this thesis aims to improve the usefulness of an optical technique known as reflection anisotropy spectroscopy (RAS), which once fully characterised could allow us to actively monitor materials in such environments.

In this thesis a specific copper surface which exhibits channels of atoms is studied. It has a high level of anisotropy (as it looks very different in the direction along the channels when compared to across the channels) and has been exploited to study nanoscale kinetics of radiation damaged surfaces. This is possible as a highly anisotropic surface, if damaged by radiation, becomes more isotropic. RAS is a non-destructive optical probe which has the ability to measure this anisotropy, and therefore the amount of damage on the surface.

We find that while damaging the surface with radiation, the amount of anisotropy measured is temperature dependent. At high temperatures the atoms are more mobile so that atoms, which were dislodged by the radiation damage, cluster together or fill holes where an atom once was. Both of these processes restore anisotropy to the surface, which can be measured using a feature in the RAS spectrum.

In this thesis I have created a model of the copper surface which simulates the radiation damage. This is done by creating impact sites with holes where atoms once were, and around the holes atoms which 'sit' on the surface; this is analogous to a crater where a stone has been dropped into sand. The atoms are then given energy to move over the surface (this is equivalent to increasing the temperature of the surface) and in doing so repair the damage. Using this method experimental RAS data has been successfully modelled. This helps us understand the key ways

the atoms behave on the surface as a function of temperature, and shows how RAS could be used in the future to monitor radiation damaged surfaces.

Declaration

I declare that this thesis was composed by myself, that the work contained herein is my own except where explicitly stated otherwise in the text, and that this work has not been submitted for any other degree or professional qualification except as specified.

(*Terri Amos, 2014*)

Acknowledgements

I would like to give thanks to a few people here, as if it weren't for them this thesis would never have been.

Firstly my supervisor, Dr. Jamie Cole, has been a huge support to me through out my Ph.D and writing of this thesis. This research would never have been completed without his expertise and encouragement. Thank you Jamie.

I would also like to thank my 2nd supervisor, Prof. Graeme Ackland, who provided me with golden nuggets of information regarding Monte Carlo simulations which greatly added to my understanding and speeded up my progress. I also had many productive discussions with Dr. Paul Lane, who took most of the experimental data which has been analysed in this thesis, and also proof read Chapter 2 which I am very grateful for.

Thank you to my family for their support and encouragement in undertaking a Ph.D, for always being there for me at the end of the phone when I needed a chat, and for always being so welcoming and happy to see me any time I visit. Moving 400 miles away hasn't always been the easiest, but it was made much better by all of your support.

Lastly I would like to thank Dan. He stood by me during the up's and down's of research, kept me on track, listened to me when I needed a sounding board, gave me new ideas, lots of encouragement, asked me to marry him in our first year, proof read my thesis, and was just amazing throughout! Thank you Dan.

Contents

List of Figures

List of Tables

Chapter 1

Introduction

Surfaces pose an interesting area of research as it is here that many physical and chemical processes occur. While solid state physics primarily deals with the bulk of a material, where structures are considered as infinite in all directions, surface science deals with conditions where this is not inherently the case [1–4]. This termination of the bulk structure leads to symmetry breaking, surface reconstructions, and formation of entirely new electronic states.

Studying surfaces on the nanoscale allows for in depth interpretation of the atomic arrangement. This is important for understanding processes such as chemical reactions, crystal growth, catalysis, and atomic diffusion. Continuing research into this area is important to further understand these processes and to develop new technologies which exploit the unique physics at the surface.

The work of this thesis aims to improve the usefulness of an optical technique known as reflection anisotropy spectroscopy (RAS) and by using our current understanding of it to develop a simulation which models the nanoscale surface kinetics of ion bombarded surfaces. Once fully characterised RAS may allow us to actively monitor materials within a nuclear reactor or on a satellite, both of which experience continually damaging radiation leading to degradation over time. Currently a material's safe working life time in these environments has a large, costly, safety margin. Further understanding could allow for a materials replacement closer to when it begins to fail, and not before.

1.1 Studying Surfaces using Light

Epioptics, a term first coined by John McGilp in 1995 [5], is the study of surfaces using the optical spectrum of light. At these wavelengths the penetration depth of electromagnetic radiation is much larger than the few monolayers needed to study the surface [6], and the processes that occur there, it therefore must be split into surface and bulk component signals. The non-trivial contribution from the surface, however, has been identified with improved techniques and instrumentation. Various epioptics techniques such as laser light scattering [7], surface differential reflectance [8], photoluminescence [9], and RAS [10] have been developed which isolate the surface contribution in the resulting spectra.

As the penetration depth of the optical wavelength is so long these epioptic techniques are non-destructive as the surface receives little of the energy of the impinging radiation. This is essential when studying time evolved phenomena on the surface, and also convenient for cases when samples are expensive or time consuming to produce. Also of advantage is the simplicity and ease of use of these techniques. Many surface probes require ultra high vacuum (UHV) environments, but this is not the case with epioptics as light is not significantly scattered by transparent media, such as air, and so can be used in non-specialised environments. This ability to be used in 'normal' ambient conditions means many epioptic techniques can be used in a number situations many other techniques cannot access. Their simplicity arises from the type of radiation used, where only optical spectra is utilised, and in many cases a standard lamp can be used to generate the radiation (or if a spectra is not desirable a small, cheap, laser can be utilised to produce a single wavelength instead). As these are cheap and readily available, epioptics becomes very accessible when compared to complex techniques such as scanning tunnelling microscopy (STM).

1.2 Simulating Surfaces

Simulating a physical system allows us to develop a unique insight into the processes which govern it. In modelling a system it might be thought that identifying every parameter, process, or perturbation that drives it is desired. This is, in fact, not usually so helpful as most real systems are extremely complex and actually can be described with a smaller number of key parameters which

dominate the behaviour. It is identifying these primary governing processes and parameters which is more interesting, as these tell us a lot about the physics of the system being modelled. This is further improved when coupled with experimental data, such that reproducing the observations can help determine if the key processes have been correctly ascertained and calculated.

This thesis examines the nanostructuring and kinetics of the Cu(110) surface and uses computational simulations to model experimental data already collected from the system.

To date, ion damaged crystals have been modelled using molecular dynamics (MD) and atomistic simulations [11–14]. This thesis builds on this work by using the results from MD simulations as input parameters in a kinetic Monte Carlo (KMC) simulation; this enables us to greatly increase the simulated time and length scales needed to model experimental observations.

1.3 Thesis Outline

The aims of this thesis are to further characterise the RAS spectrum of Cu(110) and to model the nanoscale kinetics of the ion bombarded Cu(110) surface. This is achieved through construction of a KMC simulation and analysis of experimental RAS and STM data to calibrate the model.

Chapter 2 introduces RAS and discusses the experimental techniques which are used to gain data analysed in this thesis. STM is also discussed here as it is a complimentary experimental technique used along with RAS to understand the nanostructuring of the ion bombarded surface.

Chapter 3 discusses Cu(110) which is the particular surface analysed in this thesis. The RA spectra of the surface is discussed in detail as well a review of the work already performed in understanding its surface kinetics.

Chapter 4 introduces the KMC simulation with explanations of the key algorithms used in the simulation, the input parameters, and the analysis techniques which allow for the comparison with experimental RAS and STM data. Preliminary results are also presented at the end of this chapter.

Chapter 5 gives results of simulation testing which was carried out to confirm that the program behaves sensibly, and to ascertain its robustness and sensitivity

to input parameters.

Chapter 6 presents results of simulating the Cu(110) surface during ion bombardment, using the KMC simulation. Simulations were carried out in order to replicate experimental conditions, where the aim was to understand defect kinetics of Cu(110) further. A new type of analysis is also presented in this chapter where the patch per ion impact is monitored over bombardment time. This method of analysis may give further insight into the diffusion mechanisms on the surface, and a direct way of measuring diffusion using RAS data.

Chapter 7 analyses the nanostructure of the ion bombarded Cu(110) surface after long diffusion periods of up to 30 minutes. STM images of the surface have been re-analysed and compared to KMC simulation results of the surface which are shown to improve on MD simulation results. The evolution of adatom clusters are also analysed giving an insight to the formation of surface clusters.

Chapter 8 presents results of studying the annealing process of a damaged surface using the KMC simulation. Results of the ion bombarded surface after long diffusion periods are presented and compared to experimental RAS results. Also calculated is a new value for the diffusion coefficient, D_0, by comparing the simulation and experimental results.

Chapter 9 present the conclusions of the work in this thesis and suggests areas of further study.

Appendix A contains residuals of data analysed in Chapter 6.

Chapter 2

Experimental Techniques

2.1 Introduction

In this chapter RAS is discussed in detail including the techniques used to gain experimental data analysed in this thesis, as well as a discussion of the optical system. Scanning tunnelling microscopy (STM) is also discussed here as it is a complimentary experimental technique which when used with RAS can help us understand the RA spectra in more detail and thus the nanostructure of the surface.

2.2 Reflection Anisotropy Spectroscopy

RAS is a non-destructive optical probe which provides information about a surface's electronic structure and surface modified bulk electronic structure [10]. This is achieved by measuring the difference between reflected light which polarised in orthogonal directions. This technique probes the anisotropy of the surface as a function of photon energy and is sensitive to transitions between electronic states near the Fermi level in semiconductors and metals. RAS has been shown to be sensitive to defect orientations [15, 16], atomic steps [17–19], surface alloying [20], surface reconstructions [15, 21], temperature [22–25], and molecular adsorption [22, 26, 27].

Conventional surface probes such as STM and LEED (low energy electron

diffraction) give a very detailed understanding of the surface as well as high spatial resolution. However, these techniques are often expensive due to the complex instrumentation needed, and require an ultra clean surface (and therefore a UHV environment). RAS, however, uses the reflection of visible light, as a consequence it can be applied to non vacuum environments and can achieve fast data collection. RAS is also simple to implement, relatively inexpensive, and robust, but interpretation of the RAS spectra is non-trivial. As a result, to fully understand the data complementary information is needed, either from other experimental techniques, theory or both.

In this section a history of RAS is given and the experimental technique explained with an overview of the theory.

2.2.1 A Brief History of RAS

RAS was first developed in the mid to late 1980s by Aspnes *et al.* [21, 28–31] as a novel way to investigate surfaces. RAS was first termed reflectance difference spectroscopy (RDS), but this was later changed to differentiate the method from a technique used to measure the reflectance of plane polarized light off a single crystal in separate experiments, although some groups still use the original name. In 1993 Borensztein *et al.* [32] became the first group to use the RAS technique to probe a single crystal metal surface. Prior to this RAS was mainly used in the monitoring of semiconductor growth in real time. The RAS technique is particularly useful here as semiconductor growth experiments are usually carried out in atmospheres of noble gasses, such that electron microscopy and spectroscopy would not be appropriate as the atmosphere would scatter the electrons. RAS, however, utilities EM radiation which is more weakly scattered in noble gas atmospheres.

2.2.2 Experimental Set Up

Experimental RAS data discussed in Chapters 6, and 8 of this thesis were carried out by Dr. Paul Lane (unless otherwise stated) with the equipment constructed by Dr. Brian Macdonald [33] as part of his Ph.D.

The simplest way of measuring an RA response is to measure the reflection of linearly polarised light which is incident on a sample, and then rotate the sample

or the polarisation of light while measuring reflectance, this set up is shown in Figure 2.1.

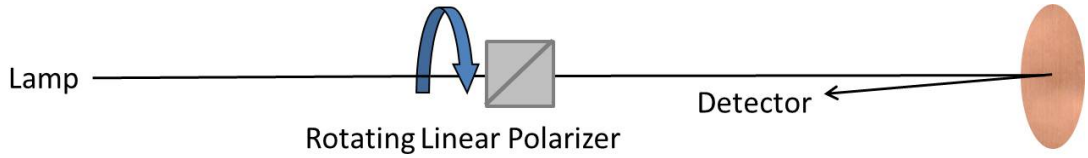

Figure 2.1 A schematic of a simple RAS setup with a rotating linear polariser.

By measuring the intensity of the reflected light as a function of the rotation an RA response can be extracted by dividing the AC output by the DC output which gives

$$\frac{I_{AC}}{I_{DC}} = \frac{R_x - R_y}{R_x + R_y}, \tag{2.1}$$

where R_x and R_y are the reflectivity of the sample in the different polarisation directions, I_{DC} is the measured reflected intensity of the DC signal and I_{AC} the measured reflected intensity of the AC signal. In this simple experimental design no phase information can be extracted from the output signal.

The spectrometer used in experiments analysed in this thesis follows the Aspnes *et al.* [21] set up, illustrated in Figure 2.2, which utilised a photoelastic modulator (PEM) instead of physically rotating the sample or polariser as used in earlier experiments by Aspnes and Studna [28].

In this set up the light originates from a Xenon lamp, passes through a polariser and is incident on a sample (if a vacuum is needed the light will pass through the window on to the sample, and then on reflection passes through the window again). The reflected light then passes through a PEM and an analyser before it is passed to the detector. An ion gun is also used to damage surfaces and create defects using argon ion bombardment.

The following sections contain more detail on how each of these components work and their main function.

The Xenon Lamp

A Xenon lamp is used for its broad spectral emission from the near infrared to near ultraviolet. It produces unpolarised light with wavelength range of ≈180nm to ≈1μm and acts as a point light source. To operate, a voltage is applied to an

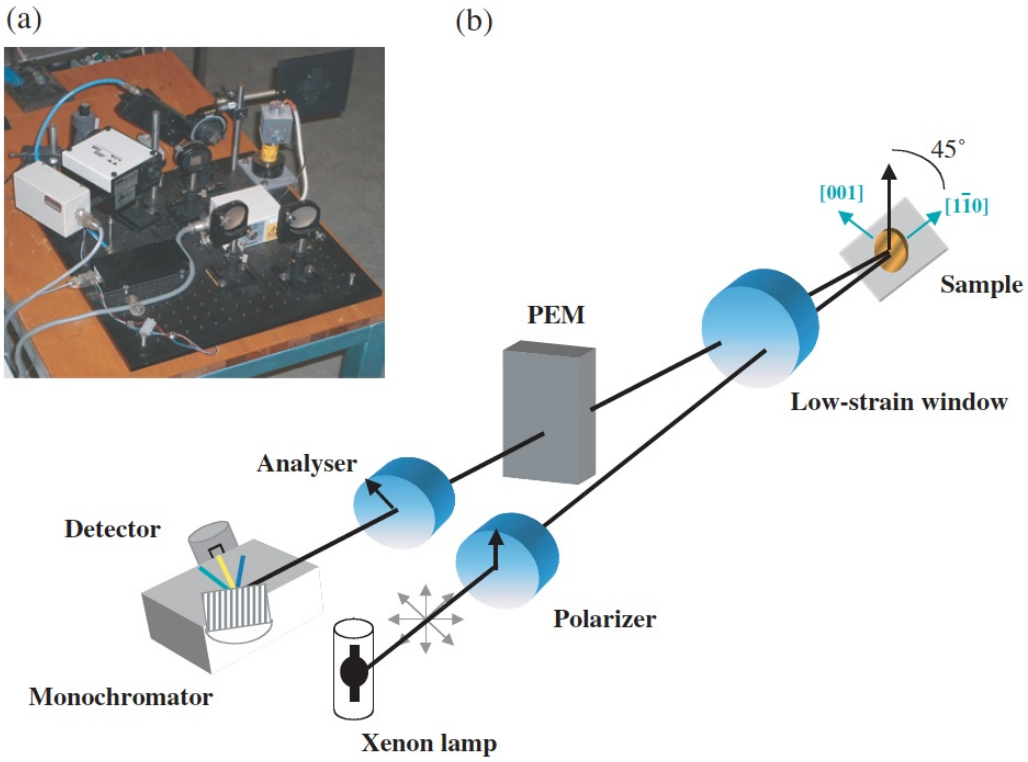

Figure 2.2 Images of the RAS apparatus using the Aspnes design [21]: (a) photograph of the setup (b) schematic showing the setup with the main components [10].

anode and cathode which is separated by a chamber of high pressure xenon gas.

The lamp has a small aperture (≈1mm) and produces an intense beam of light. Focusing mirrors are used to maintain the intensity and keep the light collimated.

The Polariser

The unpolarised light from the lamp passes through a Rochon prism which linearly polarises the light in a direction parallel to the plane of incidence.

The polariser works by utilising the interface between two prisms of birefringent material. When the light passes through the first prism there is no change in the refractive index such that all the light passes through undeviated. On entering the second prism any light that is not linearly polarised parallel to the plane of incidence will experience a change in refractive index causing it to deviate at an angle (this beam is called the extraordinary beam); this can be removed from the system. The linearly polarised light does not experience a change in refractive index (and as such is called the ordinary beam) and passes through the prism

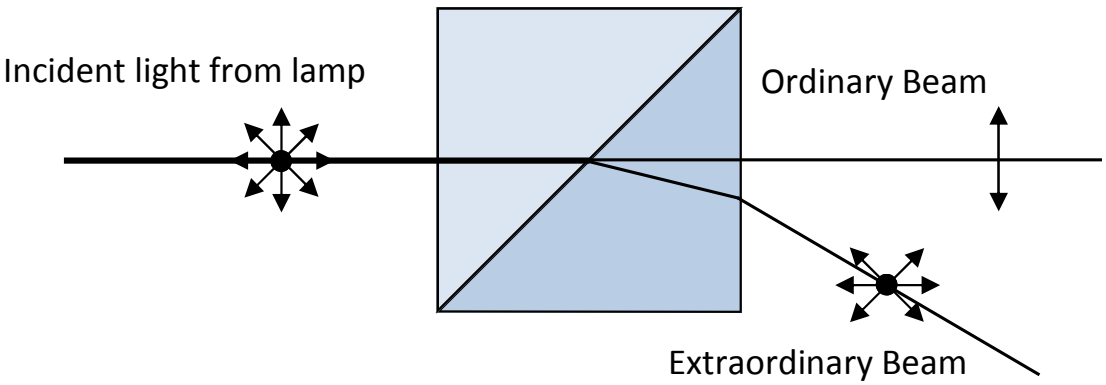

Figure 2.3 Schematic of the Rochon prism showing the deviating the extraordinary beam of light and the ordinary beam (linearly polarised light) passing through the prism undeviated.

with no change of path. A schematic of this system is shown in Figure 2.3. The linearly polarised beam is then reflected off a sample which is explained in more detail in Section 2.2.3.

The Photoelastic Modulator

The reflected light contains information about the surface anisotropy. In order to analyse the difference in the reflected x and y components, the light is passed through a PEM. The PEM modulates the retardation of one polarisation component of the transmitted light at frequency $\omega \sim 50$kHz. This has the effect of switching the reflected light into two elliptically polarised modes, one with its semi-major axis in the x direction and the other with its semi-major axis in the y direction.

The Analyser

The analyser consists of another Rochon prism which converts the phase modulated signal from the PEM into an amplitude modulated signal. The maximum amplitudes are a measure of reflectivity in the different directions. The difference in reflectivity Δr is $r_x - r_y$, and the average amplitude can be used to calculate the average reflectivity r, shown later in Equation 2.9.

The Diffraction Grating

To enable an RA spectrum to be obtained the light must be split into its individual wavelengths. This is achieved with a monochromator which uses a holographic diffraction grating. The grating has 1200 lines per mm, a spectral range of 200-750 nm, and a maximum resolution of 1nm. The light is reflected off the diffraction grating, with the wavelength of light having been selected by changing the angle of the grating, and is then incident on the detector.

The Photomultiplier Tube

A photomultiplier tube (PMT) is sensitive to the intensity of light which is impingent on it and is used to detect the RAS signal. The PMT has a spectral range of 185-900nm, which is larger than the monochromator so that it can detect all frequencies passed to it. It also has a high sensitivity, and can achieve a nanosecond response time and high signal to noise ratio. The produced signal is low current ($\sim$mA) which is converted into a voltage before being sent to the lock-in amplifier.

The Lock-In Amplifier

A lock-in amplifier is used to extract the difference in amplitudes of r_x and r_y light. To do this the PEM modulation frequency, ω, is used as a reference. The signal received by the amplifier has an AC component and an DC offset. The offset is proportional to the overall reflectivity of the sample, and the AC component contains the information about the surface anisotropy which we wish to measure.

The Vacuum Chamber

RAS can operate in a non-vacuum environment but a UHV (a pressure range of between 10^{-8} to 10^{-12}mbar [34]) is essential if precise control of the surface is needed. All experiments analysed in this thesis have been carried out in such conditions as a vacuum chamber is needed to keep the sample clean. The light, therefore, passes through a low-strain window, which has a small birefringence, into the vacuum chamber.

The chamber used in experiments can achieve an UHV of 10^{-11}mbar which is needed to keep the sample clean (for several hours at this pressure), allowing for nanoscale control of the surface.

2.2.3 The Sample

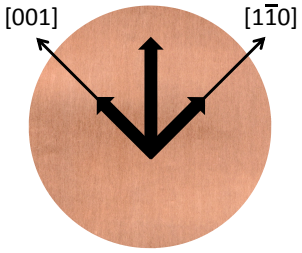

Figure 2.4 Schematic showing the incident linearly polarised light split into components in the [001] and [1$\bar{1}$0] directional axis.

As shown in Figure 2.2 the dielectric axes of the sample, assumed here to be an fcc(110) crystal, are oriented at 45 degrees to the plane of incidence of the light.

The incident light can be thought of as having equal components in the [1$\bar{1}$0] and [001] directions (x and y respectively) on the sample surface as illustrated in Figure 2.4. If there is a surface anisotropy (as there is on the fcc(110) surface) the two components of light will not reflect equally, such that after reflection the phase and/or magnitude of the two components will not be the same. Figure 2.5 shows the reflected light from the fcc(110) surface. The incident light interacts anisotropicaly with the surface which results in reflection of elliptically polarised light.

In order to obtain an RA response from the sample, the surface and/or the bulk must have some optical anisotropy in the way the light is reflected, or must undergo a process which creates this anisotropy. There must also be some long range order to the anisotropy as the beam of light has width of ∼1mm and the RAS signal is, essentially, an average over this area.

As the light penetrates some way into the bulk of the material, if the RA response is to be surface specific, the sample must have an optically isotropic bulk structure so that the contributions from the bulk cancel. Cubic crystals are therefore ideal for this type of study.

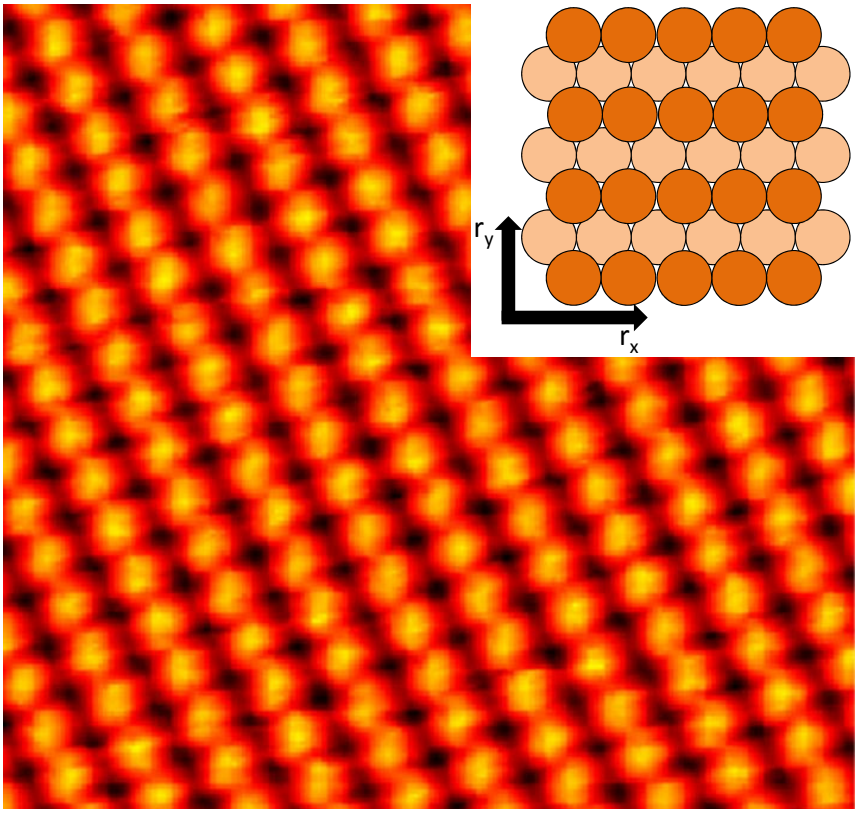

Figure 2.5 An STM image of the clean Cu(110) surface taken in constant current mode by Lane [35]. The area imaged corresponds to a 4nm × 4nm patch with the individual surface atoms visible. Inset schematic shows the reflected light from the Cu(110) surface. Vector arrows are not to scale.

The sample studied in this thesis is Cu(110) which is explained in more detail in Chapter 3.

2.2.4 The Ion Gun

An ion gun is used to bombard the sample with positively charged argon ions. This facility is needed to clean the surface by cycles of ion bombarding and annealing. The ion beam erodes the surface along with any contaminants, but this leaves the surface disordered. Annealing the sample encourages order leading to a structurally and chemically perfect surface.

The ion gun can also be used to prepare a surface with a quantified amount of radiation damage where the ion beam and plane of incidence of the light from the RA spectrometer are at 45° to each other; this enables ion bombardment and RAS measurements to be conducted at the same time.

The argon ions that are fired at the sample have a fixed energy between 100 - 3000eV and give a beam current of 10-12μA. They are created by leaking argon gas into a discharge chamber, and are then accelerated and focused onto the sample to create surface defects. The ion gun operates at typical input gas pressures of 2×10^{-5}mbar. To measure the beam current a drain current from the sample manipulator is monitored, and from this the beam size and flux can be estimated.

Ideally the gun would operate within a well defined area receiving the full flux of ions as show in Figure 2.6(a).

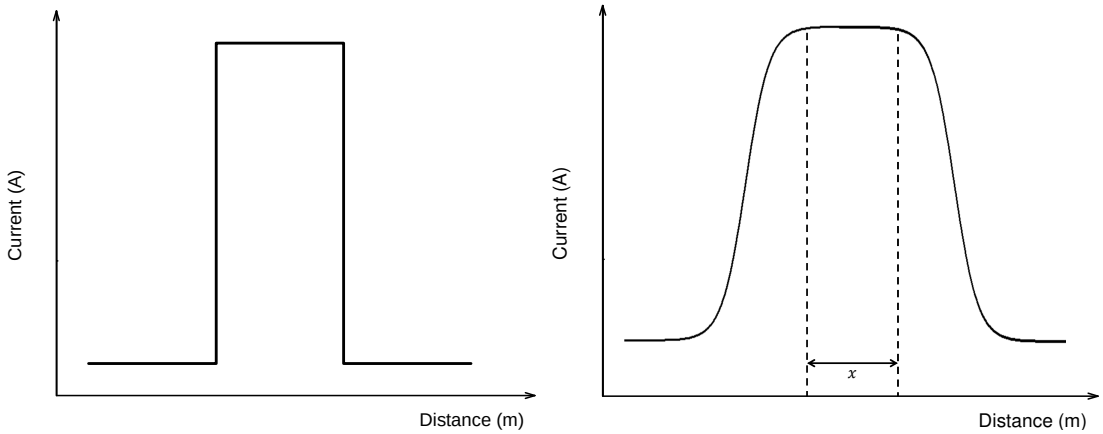

(a) Schematic of the ideal ion beam profile.

(b) Schematic of the beam profile in the experiment, where x is the approximate length and position of the sample.

Figure 2.6 Schematics of the ideal beam profile, and the profile achieved in experiment.

In reality the beam profile is closer to the distribution shown in Figure 2.6(b). This non ideal beam profile results in the sample receiving an inhomogeneous ion flux with the greatest intensity in the centre of the beam. To optimise the flux (as a homogeneous flux distribution is preferred) the ion beam is slightly de-focused so that it is wider than the sample. The sample is then moved in front of the beam until a maximum current is recorded on the sample. This then ensures the sample is within the most homogeneous and highest flux part of the beam.

The ion gun also requires time for the pressure and the filament current to stabilise, and so achieve a stable maximum flux. Ideally when the gun is switched on ions will be produced instantaneously with a stable flux as shown in Figure 2.7(a).

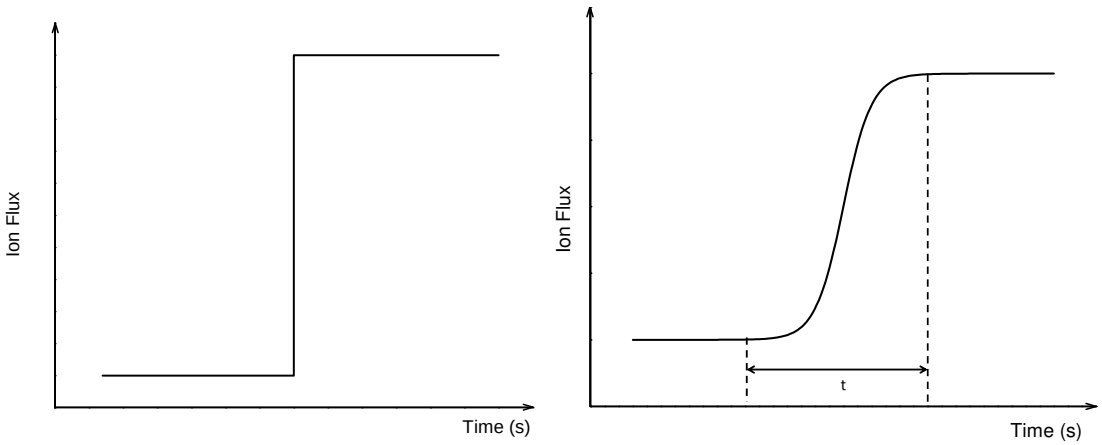

(a) Schematic of the ideal flux when the beam is switched on.

(b) Schematic of the flux when the beam is switched on which is unideal, where t is the time it takes the flux to become stable which is ≈0.3s.

Figure 2.7 Schematics of the ideal ion flux profile, and the profile achieved in experiment.

But again in reality the gun requires time for the pressure of the gas in the chamber to become stable, producing ions in the fashion shown in Figure 2.7(b). This is important to consider when bombarding a sample for a short period of time to create defects as the number of ions impacting the surface may not initially be stable. This becomes an important consideration in analysis presented in later chapters.

2.2.5 Optics of the System

To understand the optics of the system we need to consider the amplitude of the reflected light from the sample surface, which is most conveniently studied using Jones algebra,

$$E_f = \begin{pmatrix} E_x \\ E_y \end{pmatrix} . \tag{2.2}$$

By the time the light reaches the detector it is of the following form [35](described by Jones calculus in the reference frame of the analyser),

$$\begin{aligned} E_f &= \begin{pmatrix} 1 & 0 \\ 0 & 0 \end{pmatrix} \begin{pmatrix} \cos(\theta_{M-A}) & \sin(\theta_{M-A}) \\ -\sin(\theta_{M-A}) & \cos(\theta_{M-A}) \end{pmatrix} \begin{pmatrix} \exp i\delta_M & 0 \\ 0 & 1 \end{pmatrix} \\ &\quad \times \begin{pmatrix} \cos(\theta_M) & -\sin(\theta_M) \\ \sin(\theta_M) & \cos(\theta_M) \end{pmatrix} \begin{pmatrix} 1 & 0 \\ 0 & \exp i\delta W_2 \end{pmatrix} \begin{pmatrix} r_x & 0 \\ 0 & r_y \end{pmatrix} \\ &\quad \times \begin{pmatrix} 1 & 0 \\ 0 & \exp i\delta W_1 \end{pmatrix} \begin{pmatrix} \cos(\theta_P) & \sin(\theta_P) \\ -\sin(\theta_P) & \cos(\theta_P) \end{pmatrix} \begin{pmatrix} 1 \\ 0 \end{pmatrix} \\ &= \begin{pmatrix} A \\ 0 \end{pmatrix}, \end{aligned} \tag{2.3}$$

where θ_{M-A} is the difference in angle between the PEM and analyser, θ_M is the angle of the PEM, δW_1 and δW_2 are small phase shifts caused by window birefringence, and θ_P is polariser angle, and $\theta_{M-A} = \theta_P = \theta_M = 45°$.

The matrices contained in Equation 2.3 correspond (in order) to the analyser, the output rotation, the PEM, the low strain window, the sample, the low strain window, the input rotation, and the polariser. It can be shown [10] that the light intensity at the detector, $I = |A|^2$, is of the form

$$I = I_0 + I_\omega \sin(\delta_M) + I_{2\omega} \cos(\delta_M)\,, \tag{2.4}$$

where

$$\delta_M = \delta_0 \sin(\omega t)\,, \tag{2.5}$$

and ω is the modulation frequency of the PEM.

By using Bessel functions and only considering the first order terms on the window strain the normalised frequency terms can be calculated to be

$$I_0 \sim \frac{(|r_x|^2 + |r_y|^2)}{2}\,, \tag{2.6}$$

$$\frac{I_\omega}{I_0} \sim Im\left(\frac{\Delta r}{r}\right) - (\delta W_1 + \delta W_2)\,, \tag{2.7}$$

$$\frac{I_{2\omega}}{I_0} \sim Re\left(\frac{\Delta r}{r}\right)\,, \tag{2.8}$$

such that at a frequency of 2ω the signal is proportional to the real part of $\frac{\Delta r}{r}$. As

this is sensitive only to second order window strain (which is very small), most studies use the $Re\left(\frac{\Delta r}{r}\right)$ part of the RAS signal shown in Equation 2.8 to measure the anisotropy of a crystal surface.

2.2.6 Origins of the RAS Signal

A typical sample consists of an isotropic substrate and a thin overlayer with one dielectric axis parallel to the surface normal. The incident EM radiation interacts with the surface layer and also with the atoms deep within the crystal since the optical penetration depth is much greater than an atomic diameter. If the bulk of the material is optically isotropic any difference in the reflectivity of x and y polarised light can be attributed unambiguously to the surface region. If there is an anisotropy in the surface geometry, for example the fcc(110) crystal surface, then the interaction of the polarised light will depend on the direction of polarisation. It is then the difference in the reflectivity, Δr, normalized to the mean reflectance, r, which is analysed;

$$\frac{\Delta r}{r} = \frac{2(r_x - r_y)}{r_x + r_y}\,. \tag{2.9}$$

For standard samples, evaluation of the Fresnel reflection coefficients for x and y polarisation leads to the expression [36]

$$\frac{\Delta r}{r} \approx \frac{4\pi i d}{\lambda}\frac{\Delta\epsilon}{\epsilon_b - 1}\,, \tag{2.10}$$

where d is the optical thickness of the surface layer, $\Delta\epsilon$ is the dielectric anisotropy in the plane of the surface (*i.e.* $\epsilon_x - \epsilon_y$), and ϵ_b is the substrate dielectric function. The approximation is valid when d is much smaller than the wavelength of light, λ. Thus in measuring the RAS signal $(\frac{\Delta r}{r})$ $d\Delta\epsilon$ can also be deduced, which provides information about the anisotropy of the surface. This can reveal, for example, the extent of damage a surface has undergone through ion bombardment, or the alignment of molecular adsorbates.

2.3 Scanning Tunnelling Microscopy

STM, a surface probe which utilises quantum tunnelling between a sharp conductive tip and a sample, was first introduced by Gerd Binnig and Heinrich

Rohrer in 1981 [37, 38] earning them a Nobel prize in 1986.

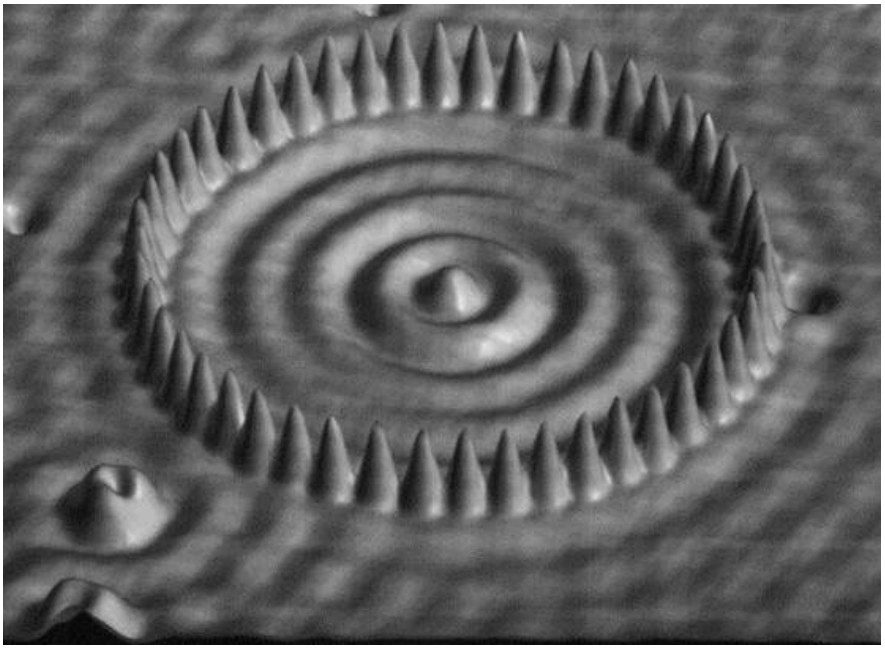

Figure 2.8 An STM image of a quantum corral [39]

To operate the tip is given a voltage bias, and when bought close to the surface (≈1nm) a tunnelling current is measured. The current is a function of the local density of states of the sample, the distance between the tip and the surface, and the voltage bias of the tip. The tip is passed over the surface, and by either keeping the tunnelling current fixed (known as constant current mode) or keeping the hight fixed (known as constant height mode) a three dimensional map of the surface can be obtained.

In constant current mode a topographical map is achieved by keeping the tunnelling current fixed and varying the height of the tip. The height in the z plane with the x and y position of the surface is recorded. In constant height mode the tip is kept at a fixed distance above the surface and the tunnelling current, which is dependent on the surface height, is used to create a 3D image of the surface.

STM imaging can give a very accurate image of the nanostructure of the surface, however, to achieve optimal resolution the surface needs to be at a low temperature and be in UHV conditions. This is to ensure the surface is contaminant free and the defects which are present on the surface are static enough for the STM tip to be sensitive to them. An example of an STM image of the Cu(110) surface collected by Lane [35] is shown in Figure 2.5.

2.3.1 Imaging Surface States using STM

It has been shown by Crommie *et al.* [39–41] that surface electronic states can be imaged using STM. Figure 2.8 is an image of a 'quantum corral'. This was created by using the STM tip to manipulate individual iron atoms and place them on a Cu(111) surface in a circle. The resulting image clearly shows the electronic states within the circle interfering and creating a standing wave. This shows us that defects influence the surface states over a large surrounding area and has recently become the focus for many groups who are interested in the phenomena experimentally and theoretically [42].

Chapter 3

The Copper(110) Surface

3.1 Introduction

The Cu(110) surface is an ideal sample to use for both configuring RAS, as it exhibits a high level of orthogonal anisotropy, as well as to study the diffusion mechanisms that govern the surface at finite temperatures. It is, therefore, the surface used in experiments analysed in this thesis, and also the subject of simulations carried out.

Copper has a face centred cubic (fcc) structure with the bulk terminated (110) surface shown in Figure 3.1. The clean Cu(110) surface adopts an unreconstructed arrangement[1] and assumes a surface configuration very similar to that shown in Figure 3.1. The lattice parameter of the unit cell (equal to the distance between atoms in the [001] direction) is 3.61Å, and the nearest neighbour distance (equal to the distance between atoms in the $[1\bar{1}0]$ direction) is 2.55Å.

This chapter gives a review of the work already performed to understand the Cu(110) RAS signal and surface kinetics.

[1] when the surface of a crystal assumes the same structure to that of the bulk.

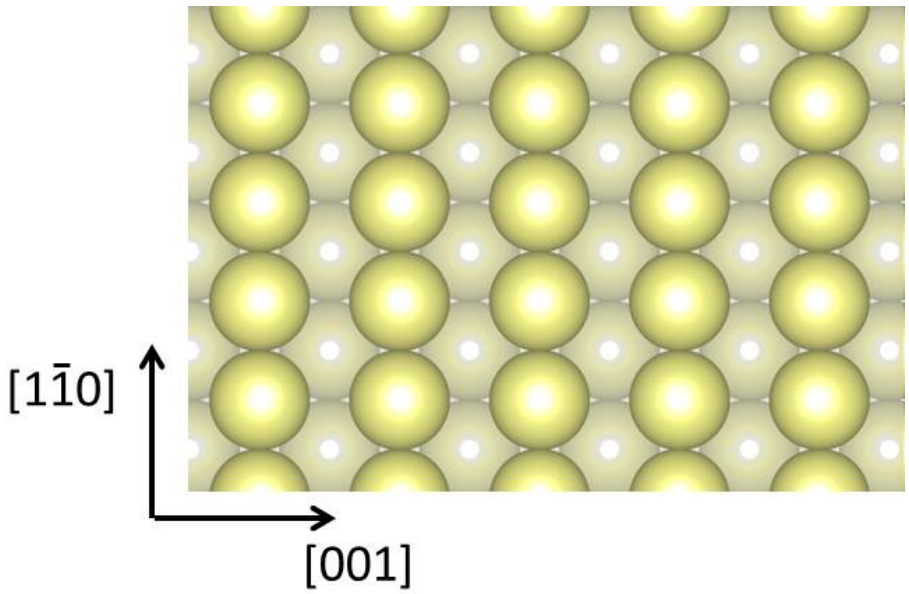

Figure 3.1 A schematic of the Cu(110) surface showing the anisotropy present in the arrangement of surface atoms, with the [001] and [1$\bar{1}$0] directions indicated.

3.2 RAS spectra of Copper(110)

The RAS spectrum of the Cu(110) surface was first studied by Hoffman *et al.* [43] in 1995 who reported the spectrum of the clean surface as well as the effects of surface adsorbates on the spectrum. It has since become well studied, with the RAS signal analysed by several groups making it reasonably well understood, this makes it possible to correlate changes in the RAS spectrum to modifications on the surface.

The RAS spectrum of clean Cu(110) at room temperature, shown in Figure 3.2, has two distinct features; these occur at photon energies of ≈2.1eV and the region of ≈4eV. The presence of these features is not obvious and arise from different effects, which are discussed in more detail in the following sections.

3.2.1 The 4eV Region

The 4eV region contains two inverted peaks, one at ≈3.9eV and the other at ≈4.2eV as visible in the spectra (Figure 3.2). One of the first attempts to explain this region was made by Sun *et al.* [44] where it was suggested that the 3-5eV range in the spectrum is due to the surface anisotropy of the d-band electron

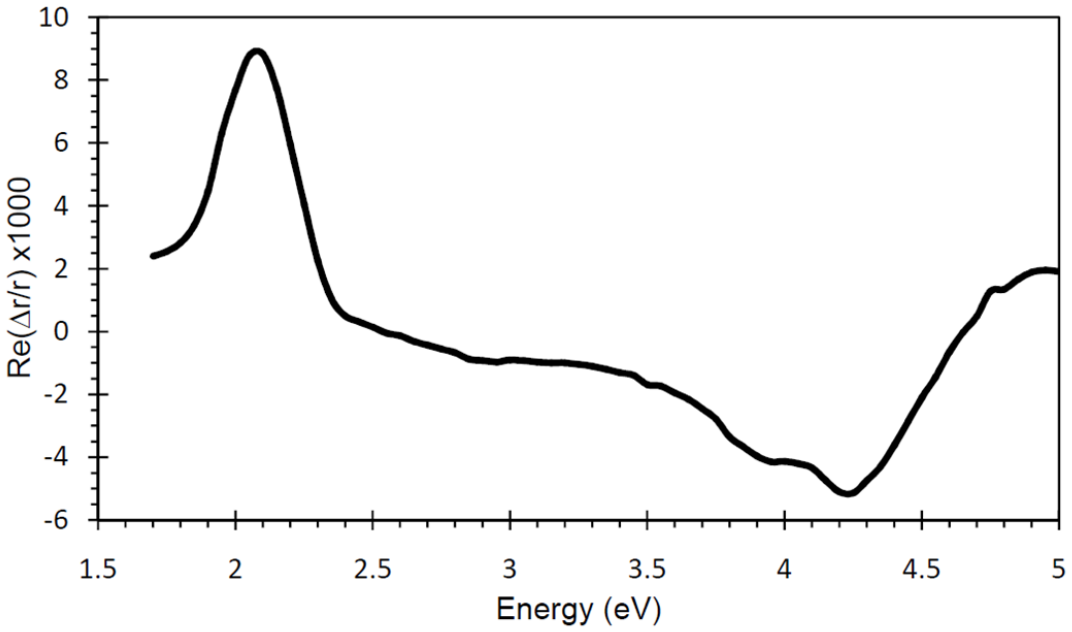

Figure 3.2 The RAS spectrum of clean Cu(110) at room temperature [35], where $\Delta r = r_{[1\bar{1}0]} - r_{[001]}$.

states. This was modelled using the derivative model, which uses an observation by Rossow *et al.* [36] that the RA spectra is proportional to the derivative of the bulk dielectric function, ϵ_b, with respect to the photon energy, E, such that

$$\frac{\Delta r}{r} \propto \frac{d\epsilon_b}{dE}\,. \tag{3.1}$$

In this study Sun *et al.* [44] also explain that the surface atoms have fewer nearest neighbours than the bulk atoms leading to a smaller overlap of d-band electrons in this region, and attribute the RAS signal to this anisotropic narrowing of the bands.

Recently Sun *et al.* [45] used the evolution of the 4eV region during and after ion bombardment to monitor the creation and healing of defects on the surface and also in the substrate bulk. This part of the spectrum evolves on a much longer time scale to the 2.1eV peak [46].

3.2.2 The 2.1eV Peak

Hofmann *et al.* [43] produced the first RAS signal of clean Cu(110) under UHV conditions. The spectrum obtained clearly shows the 2.1eV peak, though inverted

due to a sign error. The peak is due to the transitions between two states on the surface Brillouin zone, shown in Figure 3.3 [47], occurring at the $\bar{Y}$ symmetry point. This is based on a study by Jiang *et al.* [48] where they explain that as

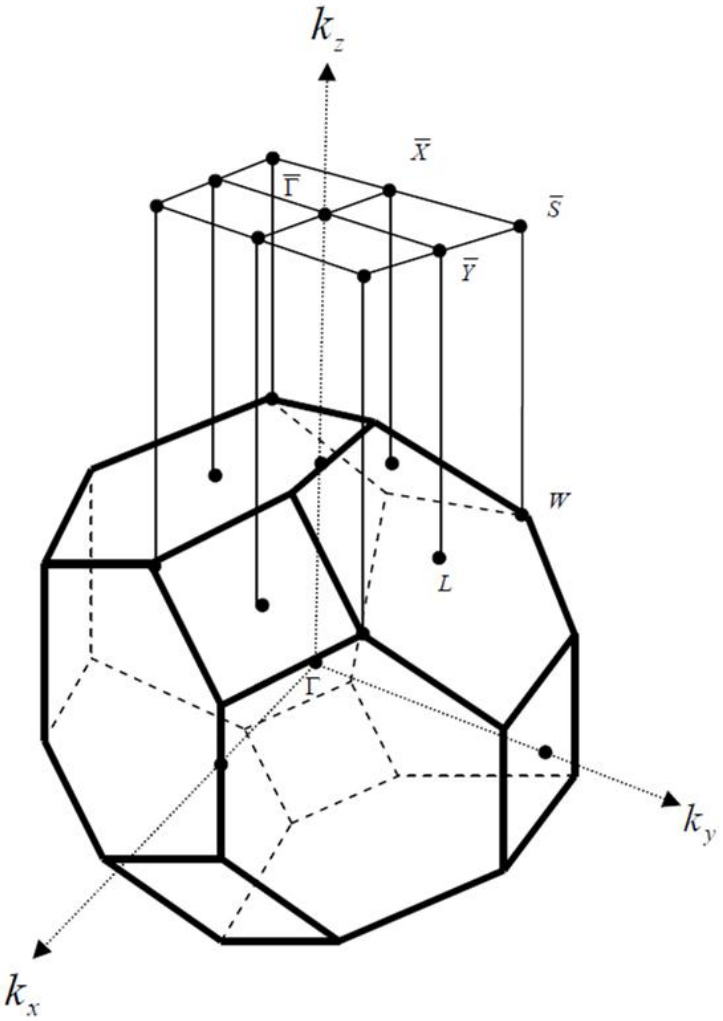

Figure 3.3 A schematic of the bulk Brillouin Zone for Cu with the surface Brillouin zone projected in the k_z direction [47].

the electrons that occupy the ground state are p-orbital, due to dipole selection rules, only light polarised in the [001] direction can excite these electrons. These states lie within forbidden regions in the bulk of the material but are created at the surface where the bulk of the crystal terminates. The atoms at the surface have a lower coordination number which produces surface electronic states that lie in the otherwise forbidden regions.

Stahrenberg *et al.* [49] followed this by producing a non-inverted spectrum of clean Cu(110), correcting the sign error made earlier by the same group, and

also assigned the 2.1eV peak to the $\bar{Y}$ transition described above. The transition made is between a partially filled band and an unoccupied band, as illustrated in Figure 3.4. The occupied band lies ≈0.4eV below the Fermi energy and the unoccupied state lies ≈1.8eV above, as shown by photoemission [50] and inverse photoemission [51] spectroscopy results.

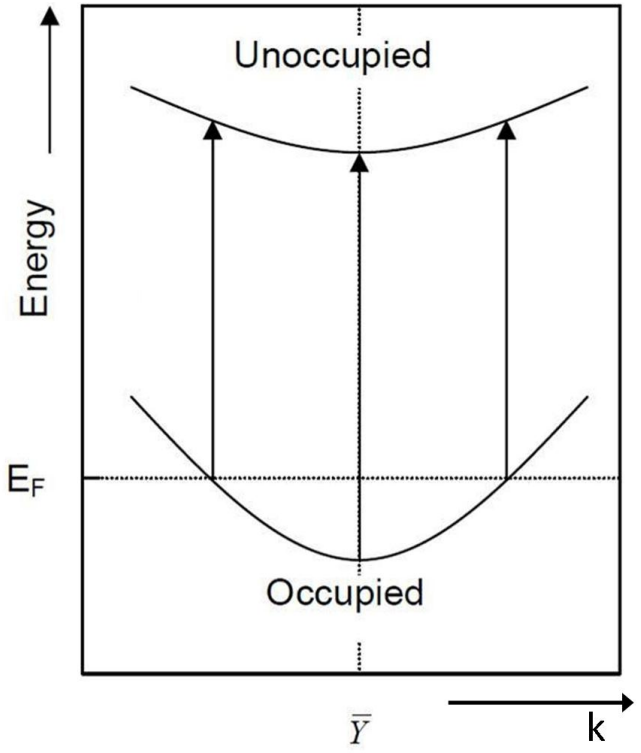

Figure 3.4 Diagram showing the occupied and unoccupied bands at the $\bar{Y}$ symmetry point in the surface Brillouin zone and the Fermi energy (E_F) [35].

RAS spectra are known to be sensitive to the temperature of the surface [22–25], this effect has been observed for the Cu(110) 2.1eV peak by Martin *et al.* [23]. The peak intensity was observed to decrease with increasing temperature which they attribute to a shift in the surface states. Using STM images they were also able to observe a roughening of the surface and a high proportion of generated monatomic steps with increasing temperature, both of which affect the peak. It was also found that the 4.2eV peak in the 4eV region of the RA spectrum was enhanced with surface roughening and increasing temperature.

Sun *et al.* [24] were the first to present a calculation of the surface state RA spectrum with varying temperature. They calculated the surface dielectric

anisotropy spectrum, $\Delta\epsilon$, by integrating the optical transitions in the vicinity of the $\bar{Y}$ symmetry point, illustrated in Figure 3.4, using the expression:

$$\Delta\epsilon_s(\omega, T) \propto \frac{1}{\omega^2} \int_0^\infty L[\omega - E_f(k) + E_i(k), \sigma]\, F[E_i(k), T]\, k\, dk\,, \qquad (3.2)$$

where E_i and E_f are the initial and final energies of the electronic transition, $L[\omega, \sigma]$ is a Gaussian with width σ (which is dependent on T to model vibrational broadening), and F is the Fermi-Dirac function. Using literature values for the band curvatures and for the T dependence of the band energy shifts Sun *et al.* computed $\Delta\epsilon$ and hence the RAS spectrum of Cu(110). Calculated results showed that the 2.1eV peak intensity decreases and shifts to a lower energy with increasing temperature, as seen in experiment.

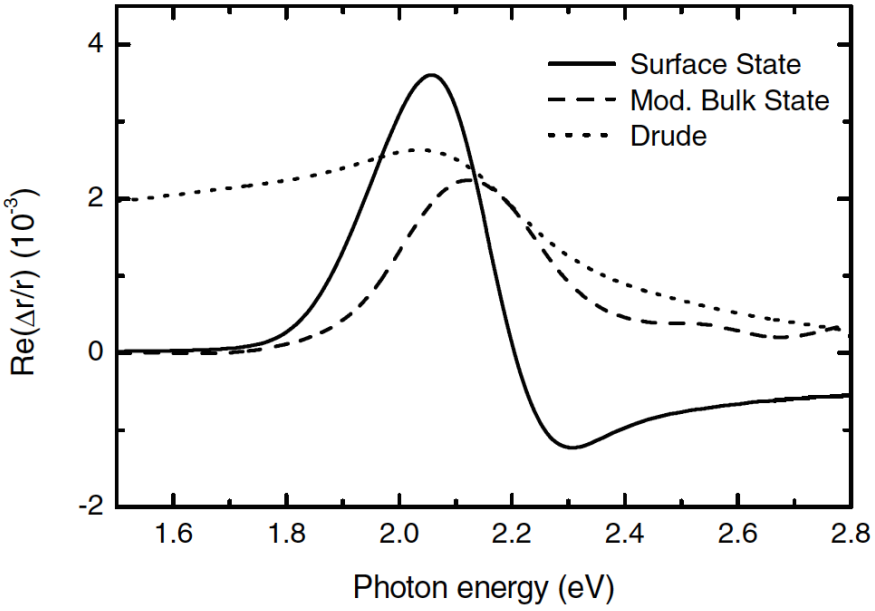

Figure 3.5 The contributions to the 2.1eV RAS peak [24].

Since only qualitative agreement was observed Sun *et al.* [24] offered a more complex interpretation of the RAS spectrum, attributing it to the combination of three contributions; surface state transitions, transitions between modified bulk states (with relationship described by Equation 3.1), and an anisotropic Drude effect (which assumes a free electron-like conduction band, but with differing parameters for transitions that can be accessed with [001] and $[1\bar{1}0]$ polarised light), the combination of which are shown in Figure 3.5. This improved on the agreement with experimental data but since each of the three contributions has structure around 2.1 eV, the resulting spectrum is not very sensitive to the relative weights of the different components.

Lane *et al.* [22] later pointed out that the temperature dependence of the band energies, and their curvatures, are not known precisely and fine-tuning of these parameters (within the error bars) allows the shape of the RAS spectrum to be fitted well by a surface state calculation alone. Results for 100K and 300K are shown in Figure 3.6. However the intensity of the 2.1 eV RAS peak of

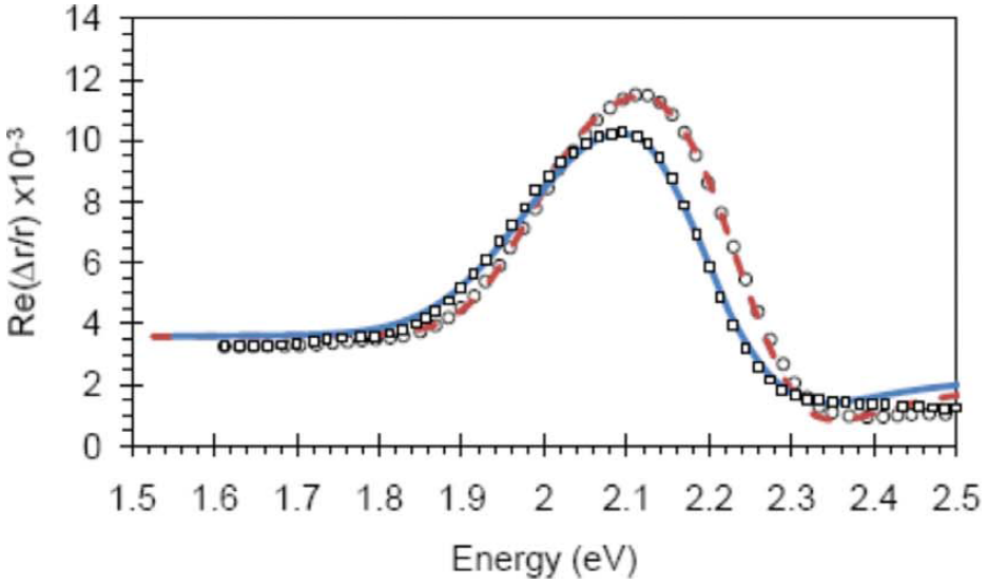

Figure 3.6 The computed RA spectra at 100K (red dashed line) and 300K (blue line) [22] and the experimental spectra at 100K (circles) and 300K (squares) [24].

Cu(110) is lower in experiment than predicted by a surface state calculation for temperatures above 300K. This is also the case for Ag(110) where there is no ambiguity concerning Drude effects or surface modified states. As T is increased the peak was lost more quickly than expected using the surface state model, indicating a missing element. Isted *et al.* [25] assigned this to thermally induced surface defects, whose effect was modelled using the Poelsema-Comsa method, described in Section 3.3, (which assumes the surface state electrons are scattered by defects) originally suggested by Sun *et al.* [27].

3.3 The Poelsema-Comsa Model

In an attempt to model the 2.1eV peak intensity Heskett *et al.* [52] used an algorithm which placed an $N \times N$ patch on each lattice site. If there is no defect present within the patch, then all the lattice sites within the patch

contribute towards the RA signal[2], and only those sites within the defect free patches contribute. They created a Monte Carlo simulation to model inverse photoemission spectroscopy (IPES) results of Cu(110) using this algorithm but did not consider adatoms or diffusion in their model. They reported that the IPES peak, which corresponds to the $\bar{Y}$ state, which generates the RAS signal seen at 2.1eV, decayed approximately exponentially with defect density while the decay in their simulated signal was approximately Gaussian.

Sun *et al.* [27] improved on this and were the first to use a model devised by Poelsema and Comsa [53] to simulate the 2.1eV RAS peak. The model was originally used to recreate helium surface scattering intensities, where a surface defect will scatter He atoms within a patch with an area centred around the defect which is larger that the area of the defect. Applying this analysis technique, the normalised 2.1eV Cu(110) RAS peak intensity during ion bombardment can be described by the following equation [22, 25, 27, 54];

$$I = (1 - \theta)^{\Sigma_I} \,, \tag{3.3}$$

where θ is the density of ion impacts (θ = ion flux $\times$ time), and Σ_I is the RAS cross section or patch size per impact in unit cells. Using this improves on the Heskett *et al.* [52] method giving the correct exponential decay of the peak.

This method assumes the electronic surface states, which contribute to the RAS peak intensity, are scattered within a patch centred on the ion impact site which has a total size of Σ_I. The impact sites form a lattice gas[3]. As the impact sites are made up of a distribution of individual defects Σ_I can be thought of as a function of the area of the RAS patches which are centred on each defect, Σ_d, such that

$$\Sigma_I = f(\Sigma_d) \,. \tag{3.4}$$

As a result the scattering area surrounding the impact site is larger than the physical area of the defects created by the impact. The 2.1eV peak signal then originates from the area of the surface which has not had its electronic states scattered by surface defects.

[2] *i.e.* the surface states within the patch are intact and not scattered.

[3] A lattice gas is a lattice where each site can either contain a molecule or not [55], such that molecules are only contained within the lattice sites. When discussing a lattice gas in this thesis it is also implied that the molecules are randomly distributed as an ideal gas would be.

The active surface fraction, f_a is proportional to the RAS peak intensity

$$I \propto f_a = \frac{CleanSites}{Clean + DamagedSites}\,, \tag{3.5}$$

where a lattice gas site is considered 'clean' if it is not within a patch (therefore the surface electron states are intact within that lattice site) and a site is considered 'damaged' if it is within a patch (as the surface electron states are damaged within that patch). When the coverage is low the impact sites are more likely to be further apart with their RAS patches not overlapping, therefore

$$I \propto 1 - \theta\Sigma_I \tag{3.6}$$

for $\theta << 1$.

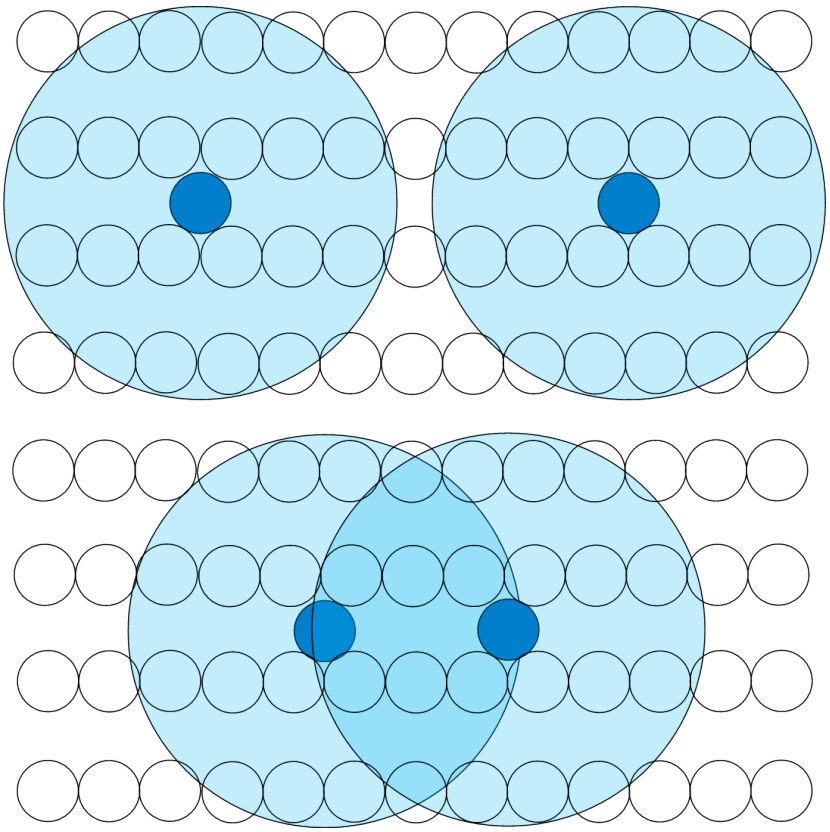

Figure 3.7 Schematic of two adatoms on the Cu(110) with 'RAS patches' that do not over lap, and two adatoms with overlapping patches.

When the defects are close enough to each other such that the RAS patches overlap the result is that the total area of the surface which is damaged is less than if they were further apart; illustrated in Figure 3.7.

Equation 3.3 assumes the total patch area per impact size , Σ_I, is constant over

time; the applicability of this assumption is something which is considered in Chapters 5, and 6.

3.4 Ion Bombarded Copper(110)

Bombardment by ions liberates some surface adatoms into the vacuum, which erodes the surface, but also changes the structure by creating vacancies in the top-most layer and depositing adatoms around the vacancies [56–58]. This is not too dissimilar to a crater where a stone has been dropped into sand.

There have been several studies aimed at gaining an understanding of the nanostructure of the ion bombarded copper surface [14, 22, 23, 33, 35, 54, 59–63]. Below are two which lead us to the conclusion that surface defect diffusion plays an active role in shaping the surface. It is as a consequence of this work that I have written a kinetic Monte Carlo (KMC) simulation, outlined in Section 4.2, to simulate diffusion of defects on the surface.

Also presented in this section is the effects of temperature on the RAS intensity, the data of which is used later in Chapter 6 for comparison against simulation data.

3.4.1 STM Imaging Used to Interpret the 2.1eV RAS Peak

As the atomic arrangement of the surface directly affects the surface electronic structure, combing RAS and STM imaging gives a unique and powerful insight into surface morphology [23]. By using STM in conjunction with RAS we are now able to interpret surfaces outside of cold and high vacuum environments. This new understanding can then be applied to surfaces which are not necessarily under these conditions.

In a recent study by Lane *et al.* [22] the ion gun, described in Section 2.2.4, was used to damage the Cu(110) surface in order to investigate the effects of defects on surface electronic states. The yield of each impact was assumed to be 3 defects (2 vacancies and 1 adatom) but this was later shown to be too small in a study which demonstrated, through STM images of Cu(110) after ion bombardment, that the yield is much higher with approximately 5 vacancies and 25 adatoms per impact [54]. Figure 3.8(a) is an STM image showing the arrangement of

the impact sites; it can been seen that the ion impact creates islands of adatom clusters around vacancy clusters, analogous to the debris seen around a crater formed by a mechanical impact.

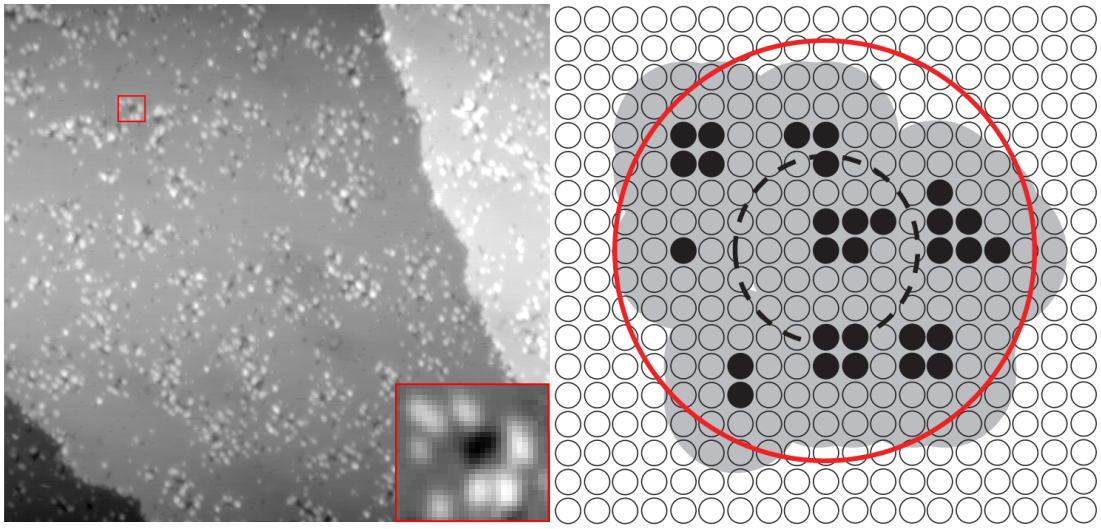

(a) An STM image of the Cu(110) surface after ion bombardment. The inset picture shows a magnification of a typical impact site (approximately $4\text{nm} \times 4\text{nm}$) with the vacancies (black) clustered in the centre and the adatom clusters (white) dotted around the vacancies [54].

(b) Schematic showing the cross section of an impact site as corresponding to the boxed area in Figure (a). The defects are illustrated as filled black circles and the lattice illustrated with open circles. The grey area shows the accumulated cross sections of each of the defects, Σ_d, and the area enclosed by the red line shows the total cross section for the impact site, Σ_I, (approximately 170 unit cells) [54].

Figure 3.8 STM image of the ion bombarded Cu(110) surface at 144K and a schematic showing an impact site with proposed RAS cross section.

The atomic defects did not form a lattice gas (as they have a non random distribution), but with knowledge of the surface geometry the Poelsema-Comsa model, explained in Section 3.3, was used by Isted *et al.* [54] to model the RAS intensity of the 2.1eV peak. This was achieved by assigning each atomic defect a patch, Σ_d, which would sum up to a total patch size per impact, Σ_I, as

$$\Sigma_I = f(\Sigma_d)\,; \tag{3.7}$$

this is illustrated in Figure 3.8(b). The RAS signal was shown to decay in proportion to a patch size per impact of $\Sigma_I \approx 170$ unit cells per impact, with the individual defects having a cross section of $\Sigma_d \approx 19$ unit cells shown in

Figure 3.8(b).

In the same study [54] STM images of the Cu(110) surface at 144K were used to calculate the RAS peak. The surface was bombarded at intervals of 2 seconds with a flux of 0.0014 impacts/unit cell/second and then imaged (such that a clean surface was prepared, bombarded for a specific time, and then RAS and STM measurements made). By using the images of the surface with the Poelsema-Comsa analysis they attempted to calculate the normalised RAS 2.1eV peak intensity for each bombardment time with different patch sizes, the results of this is shown in Figure 3.9.

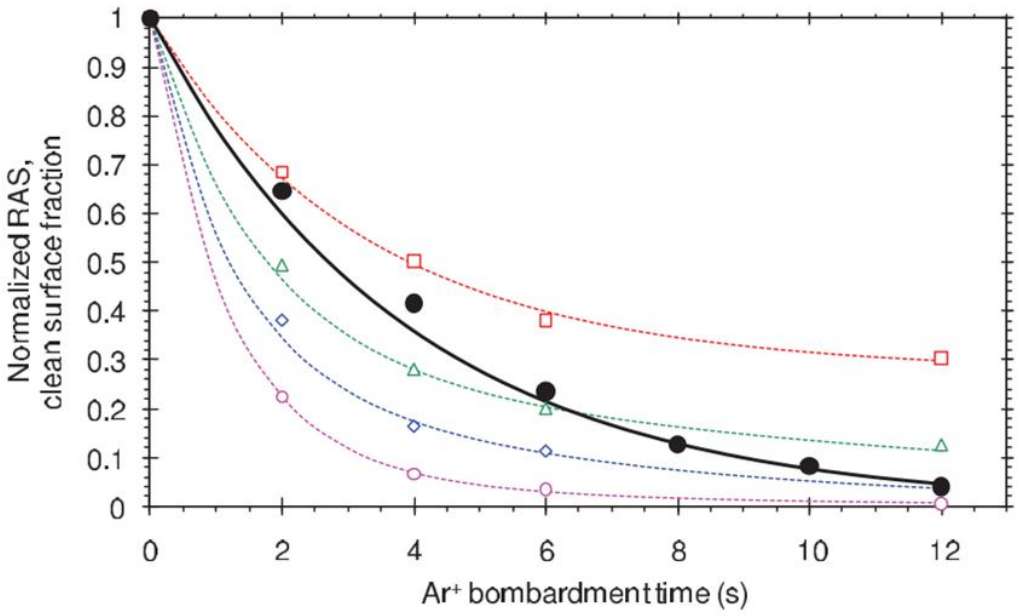

Figure 3.9 The normalised 2.1eV RAS peak (solid circles), and the calculated RAS peak using STM images for patch size radii of 0.5nm (squares), 0.75nm (triangles), 1nm (diamonds), and 1.5nm (open circles), as a function of ion bombardment time at 144K [54].

Using this analysis the calculated peak intensity does not fit the experimentally obtained peak intensity well. This could be due to the assumption that at this temperature the surface is inactive. The time between bombarding the surface and taking a RA spectra was approximately 2 minutes, while the time between bombarding and taking an STM image was approximately 30 minutes. The role of diffusion on the nanostructuring of the surface is further discussed in Chapters 6, 7, and 8.

3.4.2 STM and MD Cluster Results

In a recent study by Lane *et al.* [14] the ion bombardment process was modelled using a molecular dynamics (MD) simulation and compared to STM images of impact sites. It was found by analysing the STM images that an average 10±6 adatoms and 9±3 vacancies were created per ion impact. The MD simulation generated an average of 10.3±0.8 adatoms per impact which is consistent with STM analysis. The number of adatoms in each cluster size per impact was also analysed, results of which are shown in Figure 3.10.

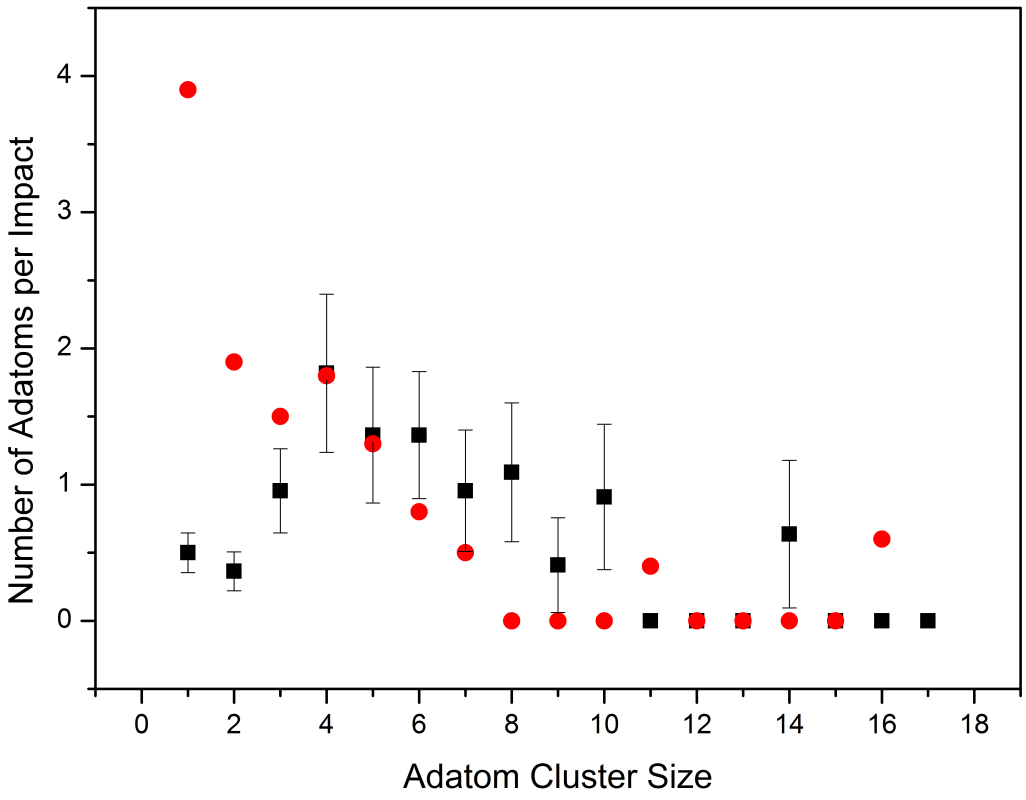

Figure 3.10 Cluster analysis of the number of adatoms created per ion impact for a given cluster size [14] for STM (black squares) and MD (red circles) analysis.

The results show a large disagreement for cluster sizes under 3 adatoms. Also, there is a broad peak in the experimental histogram at ≈ 5 adatoms which is shifted to a lower cluster size in MD, and is smaller.

In counting the clusters in STM images it may be that the resolution is not high enough to distinguish between an adatom which is one lattice site away from a cluster, which could account for some discrepancy. Figure 3.8(a) shows a

typical ion impact site which was used to gain statistics on the number and size of clusters per impact, and (b) shows the authors interpretation of the image. Though the interpretation of the positioning of the defects remains as accurate as the resolution allows, there is the possibility that some of the clusters differ in shape due to the lack of detail in the image. Also, the STM data was taken by choosing obvious impact sites and counting the number of adatom clusters in the immediate vicinity. This gives a bias to impacts that look like the classic crater (with a large vacancy cluster and adatom clusters around it), which will most likely give bias to the larger adatom clusters. Single adatoms may not always be counted using this method due to their mobility, having diffused a distance away from the initial impact site.

The discrepancy in the data could also be explained by looking at the time scales involved with each process. In the case of the MD simulations the time span is of the order of nanoseconds (this is explained in greater detail in Section 4.3.2) which allows for some diffusion on the surface, but nothing significant, while the STM data was recorded ≈30 minutes after the surface was bombarded.

3.4.3 Diffusion Effects on the Bombarded Surface

Once a surface has undergone ion bombardment at a finite temperature, the defects created will diffuse across the surface [35]. This can be indirectly seen in Figure 3.11 where at higher temperatures the 2.1eV peak is less affected by ion bombardment. This is due to the defects having enough energy to overcome energy barriers allowing them to 'hop' to adjacent lattice sites on the surface, such that adatoms are likely to recombine with vacancies or join step edges, repairing the surface and restoring the anisotropy. At lower temperatures the defects have less energy resulting in the surface becoming more disordered and isotropic with constant bombardment and hence the accelerated destruction of the 2.1eV peak seen in Figure 3.11.

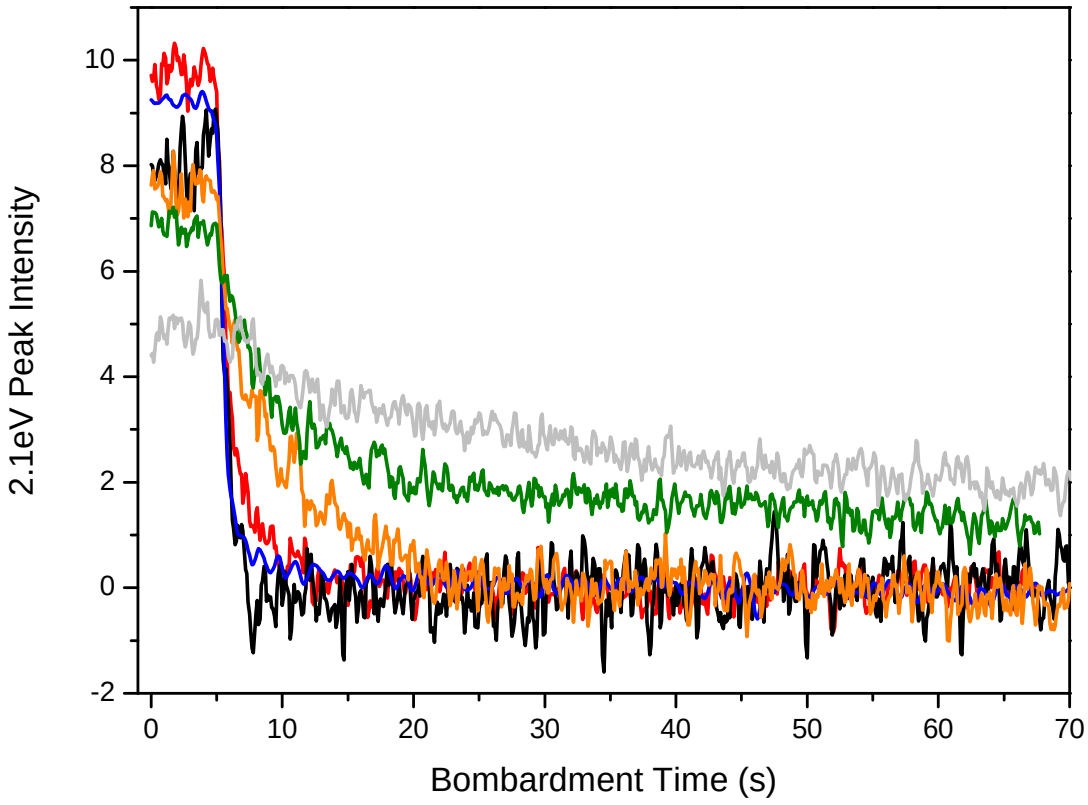

Figure 3.11 The un-normalised 2.1eV peak intensity of the ion bombarded Cu(110) surface at 183K (red), 203K (black), 223K (blue), 243K (orange), 263K (green), and 283K (grey) [35].

Chapter 4

Surface Simulations

4.1 Introduction

The conclusion was reached in Chapter 3 that to model the nanostructure of radiation damaged Cu(110) diffusion processes would need to be considered, and a simulation that can reach time spans of up to 30 minutes would also be required. A KMC simulation has been written to model diffusion processes on the surface for temperatures above ≈100K, and with time and length scales seen in experimental RAS and STM data (up to hours, and μm).

Density functional theory (DFT) is *ab initio* and solves the Schrödinger equation for electronic states based on the density of the electronic states and not the individual electron orbitals [64]. MD use these solutions as input parameters to calculate the forces on individual particles within a system, this is described in more detail in Section 4.3.2. Monte Carlo simulations then use the statistics gained using MD to simulate systems on larger length and time scales.

The schematic shown in Figure 4.1 illustrates the time and length scales different simulation methods can achieve. It is clear that a KMC simulation is appropriate as this type of simulation can reach the time and length scales needed.

This chapter contains explanations about the algorithms, input parameters, and analysis techniques used in the simulation which allow for comparison with experimental RAS and STM data. Preliminary results are also presented at the end of the chapter.

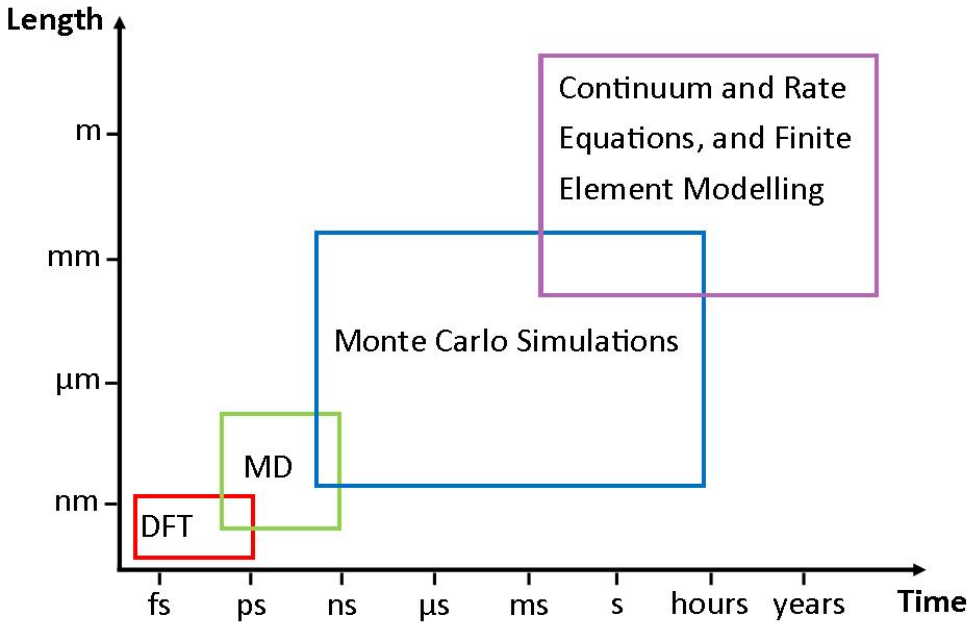

Figure 4.1 Schematic showing the approximate time and distance scales that can be accessed using different programming methods.

4.2 Kinetic Monte Carlo Methods

A KMC simulation utilising the Gillespie algorithm (explained later in this section) has been created using the Java programming language that simulates the Cu(110) surface during and after Ar^+ bombardment. Specifically, the diffusion processes and nanostructuring of resulting defects is studied in this thesis using the simulation created.

The program produces a 2D lattice with a finite depth and width where each lattice site represents a unit cell on the Cu(110) surface. There are two types of defects which are represented in the simulation, adatoms and vacancies, which are deposited on the lattice, with an initial arrangement described by MD simulation results; an example of this is shown in Figure 4.2. The ion impact sites form a lattice gas while the vacancies and adatom form a localised lattice gas within a specified ejection range centred on the impact site. By utilising the Gillespie algorithm these defects have the functionality to diffuse over the lattice.

Monte Carlo simulations rely on the generation of random numbers and the use of artificial dynamics [64]. The dynamics are said to be artificial as the true forces on the system are not analysed and calculated, only the probabilities for each process to occur is used. For example, if you take a fair coin and toss it,

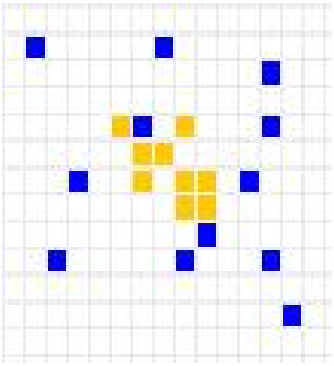

Figure 4.2 Simulated ion impact site with adatoms (blue), and vacancies (orange).

the outcome can be calculated by analysing the exact forces imposed on the coin. This method would be very slow but very exact (similar to an MD simulation explained in Section 4.3.2). By doing this a number of times it would become clear that there is a 50/50 probability whether the coin lands heads up or tails up. At this point, when we have the probability of each outcome, we can assign a random number, let's say between 0 and 1, to each flip. If the number assigned to the flip is greater than 0 but less than 0.5 then the coin lands heads up, and if the number is between 0.5 and 1 then it lands tails up. This new procedure is a description of a Monte Carlo process. This method is quicker, but relies on many samples to gain an accurate representation of the system due to natural statistical error.

MD experiments by Lane *et al.* [14] have been used to gain statistics of the Cu(110) system where in this case there are several processes to consider (which is perhaps more like throwing a loaded dice, than a coin). These are used in a KMC simulation that uses random numbers to model the kinetics of the system. By using this method much larger time scales can be reached than with MD alone.

The adatoms that diffuse on the surface undergo a random walk process [4] through independent hopping from one stable site on the surface to an adjacent site, this can be described as a stochastic Markov Chain as each hop is random and 'memoryless' (*i.e.* does not depend on the previous process). Each process (or hop) has an associated diffusion coefficient, D ($\mathrm{cm^2 s^{-1}}$), which is described by the following Arrhenius equation [65, 66];

$$D = D_0 \exp\left(-\frac{\Delta E}{k_B T}\right), \tag{4.1}$$

where ΔE is the energy barrier of the process, T is the temperature of the surface, k_B is the Boltzmann constant, and D_0 is the diffusivity of the surface. The 1D random walk equation can then be used to calculate the rate of the process occurring (the number of hops per second) [67],

$$c = \frac{2D}{d^2}\,, \tag{4.2}$$

where d is the distance to hop which is equal the lattice parameter (3.61Å) in the [001] direction, or the nearest neighbour distance (2.55Å) in the $[1\bar{1}0]$ direction.

Two complications beyond the simple coin toss analogy are apparent, firstly an adatom could potentially choose between several different processes, secondly there are many adatoms and it is unclear which one will hop next. The Gillespie algorithm, described in the next section, solves these two problems for us.

4.2.1 The Gillespie Algorithm

The Gillespie algorithm, devised by Daniel Gillespie in 1976 [68, 69], allows for one adatom to move at a time with a varying time step; this allows all processes to have to ability to occur on the surface, and tells us which adatom will move next, and where to. It is implemented by summing over all the available surface processes to find the 'activity' λ of the surface

$$\lambda = \sum_{i=0}^{n} c_i\,, \tag{4.3}$$

where c_i is the rate of a single reaction, i, (in this case the hops per second of each reaction which can be calculated using Equation 4.2). This can then be used to find the probability $P(i)$ of the i^{th} reaction to occur

$$P(i) = \frac{c_i}{\lambda}\,, \tag{4.4}$$

and also the probability $P(t)$ of a non-specific reaction happening after time interval t

$$P(t) = \lambda e^{-t\lambda}\,. \tag{4.5}$$

These two probabilities are independent of each other so each step requires the generation of at least two random numbers; one to calculate the time step and another to choose the reaction that will occur.

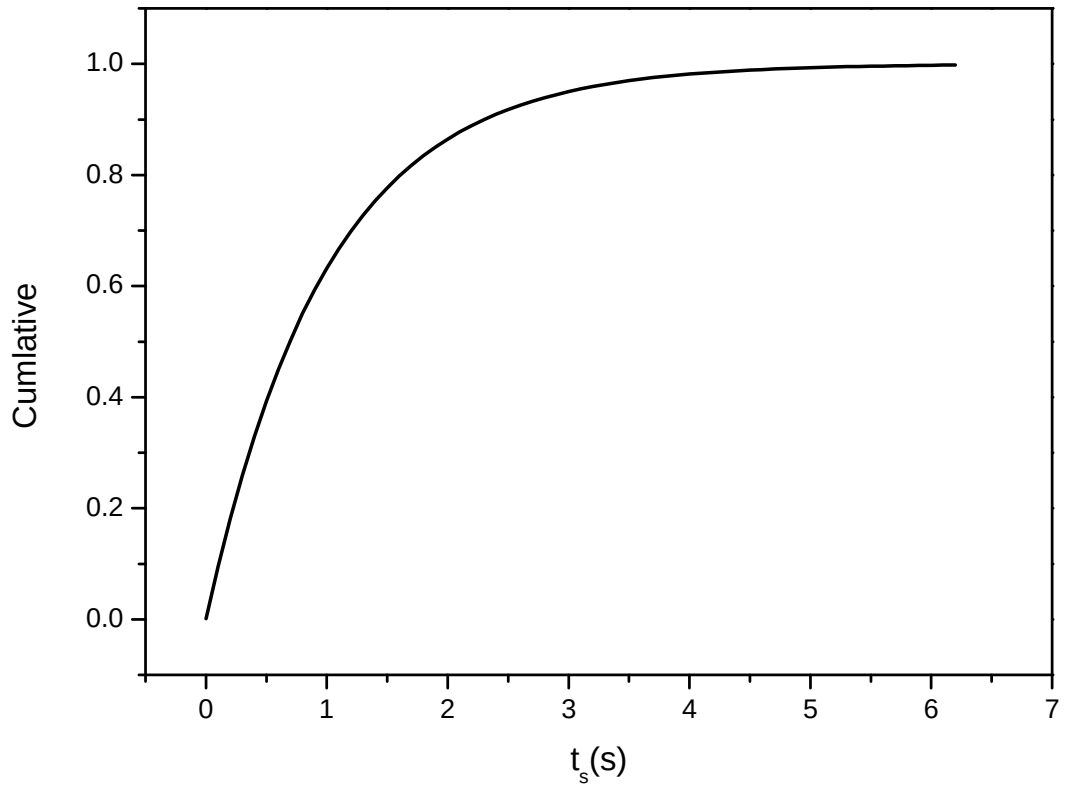

Figure 4.3 Schematic showing the relationship between the time step and the cumulative of the function $P(t)$, shown in Equation 4.6, for $\lambda = 1$.

To calculate the time step from Equation 4.5 first the cumulative, $C(t)$, needs to be calculated by integrating the probability from $t = 0$ to $t = t_s$;

$$C(t) = \int_0^{t_s} P(t)dt \ = 1 - e^{-\lambda t_s} \, . \tag{4.6}$$

The relationship between this function and the time step is shown in Figure 4.3.

By rearranging Equation 4.6 and choosing a random number, R, between 0 and 1 we can extract a time step, t_s, which is the time taken for the next reaction to occur,

$$t_s = -\frac{1}{\lambda} \ln R \, . \tag{4.7}$$

To choose the reaction that will occur, the total number of each available reaction on the surface is counted. The probability of a reaction being chosen is then weighted by the total reactions available on the surface and the probability of the reaction happening. Once a type of reaction has been chosen, the specific reaction is picked at random from all available reactions of that type.

The benefit to using this algorithm is that if the surface is inactive then the time step increases so that the program progresses quickly with no unnecessary steps, unlike a fixed time step where computational time is wasted in awaiting the next reaction.

4.2.2 Program Progression

The Mersenne-Twister algorithm was used to generate random numbers used in the simulation. Mersenne-Twister is a pseudo-random number generator which is both robust and fast.

The program progresses in the following way (also shown in Figure 4.4):

- the activity of the surface is calculated using Equation 4.3,
- a process is chosen using Equation 4.4,
- the time step is calculated using Equation 4.7,
- the adatom is moved to it's new location on the lattice, the time is updated.

This is repeated until the desired time, t, is reached.

Averaging Multiple Runs

As there is a natural amount of statistical fluctuation in the simulations due to the use of random numbers and the finite size of the simulation, it is important to carry out repeat runs to obtain an average; here we are assuming the 'ergodic hypothesis' holds true[1]. In the case of analysing the surface using the Poelsema-Comsa method, the implementation of which is described in Section 4.4.1, after each step the active surface fraction, f_a, described in Equation 3.5, is calculated. In order to average over a number of runs a uniform time step is needed, as such each f_a is binned into time steps of 0.1s (this value was chosen as many of the experiments have a data point recorded for every 0.1s). Within the bins the average f_a is calculated so that there is a value for every 0.1s increment. This then allows for the averaging over multiple runs of the program where an error on

[1] where a large system can be represented with the same smaller system sampled many times.

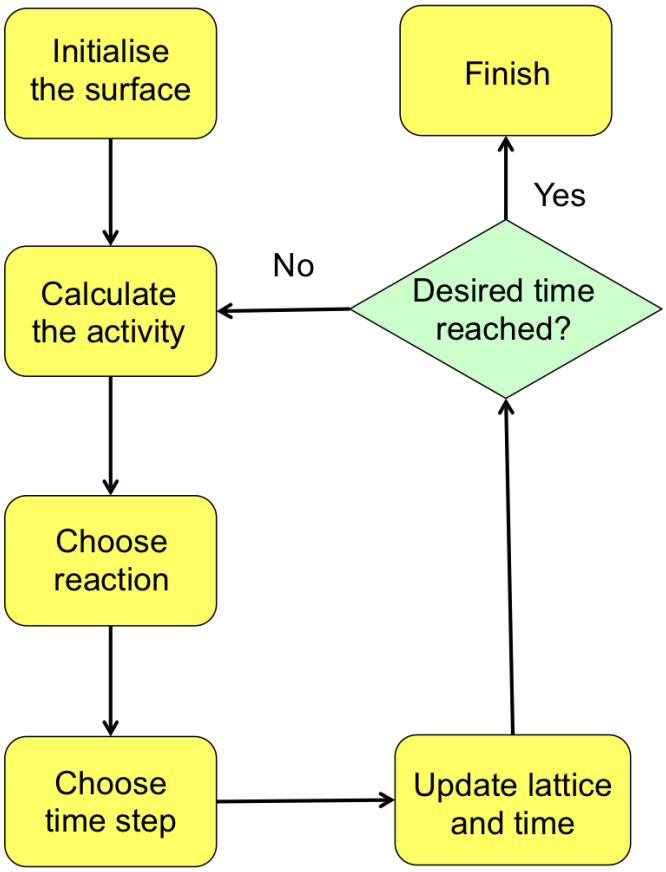

Figure 4.4 Diagram showing the steps involved with progressing the KMC simulation.

the mean can also be calculated. To minimise the error on the mean simulations are run at least 15 times.

Is is also of interest to illustrate surface properties, such as RAS intensity and adatom histograms, as a function of ion dose. As the number of ions impacting the surface is not uniform (due to the ions creating a lattice gas and impacting the surface at random intervals), the active surface fraction is binned into a constant ion dose. In each bin the average f_a is calculated so that there is a value for every increment. This then allows for the averaging over multiple runs of the program where an error on the mean can also be calculated.

4.3 Processes Included in the Model

Figure 4.5 is a schematic showing the processes that are included in the model. These processes were chosen as they have the lowest energy barriers and therefore

have the highest probability to occur at the temperatures studied. The processes labelled indicate the adatom moving in the direction of the arrow one lattice site along. Process 9 shows an adatom recombining with a vacancy. These processes are also used for large clusters as the energy barriers do not change significantly; an example of this is a trimer of adatoms in the $[1\bar{1}0]$ direction, where the energy barrier for the middle adatom to hop in the [001] direction is the same as process 4.

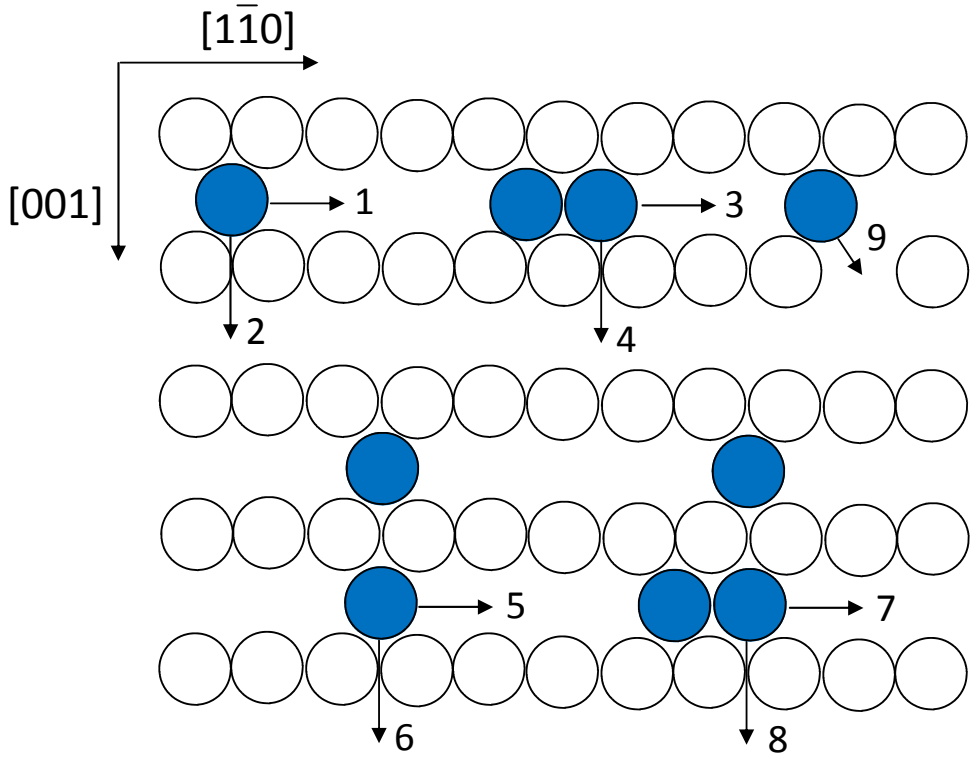

Figure 4.5 Schematic showing the processes on the surface which are included in the simulation. Adatoms are shown in blue, and surface atoms in white. Arrows indicate the adatom that will move as well as the direction.

4.3.1 Surface Energy Barriers and Hopping Rates

Table 4.1 contains information on the energy barriers associated with the processes shown in Figure 4.5. These were calculated by Lane *et al.* [14] using MD simulations, and are similar to energy barriers calculated by other groups [70–72] (which are within 10% of the values calculated by Lane *et al.* [14]). The effect of varying the energy barriers by a fixed percentage is explored further in Section 5.3.3.

Process, i	Energy Barrier (eV)
1	0.33
2	1.17
3	0.64
4	1.29
5	0.36
6	1.18
7	0.69
8	1.28
9	0.37

Table 4.1 The energy barriers for the associated process shown in Figure 4.5 calculated using MD simulations [14]

To give an idea of the hopping rates involved, using $D_0 = 6.29 \times 10^{-4}$ cm^2 s^{-1} [72] and a temperature of 150K, the hopping rate of a single adatom in the $[0\bar{1}1]$ direction (process 1) is ≈ 8 hops per second, and the hopping rate of a single adatom in the [001] direction (process 2) is $\approx 6 \times 10^{-4}$ hops per second.

Figure 4.6 shows how the hopping rate of different processes varies with temperature. As can be seen from the graph processes 1, 5, and 9 are the dominant processes as these govern along channel diffusion which have the lowest energy barriers. This means at low temperatures the processes with the smallest energy barriers dominate the diffusion process.

We can calculate the hopping ratio of two different processes with temperature, T, by combining Equations 4.1 and 4.2 to give

$$\frac{c_a}{c_b} = \left(\frac{d_a}{d_b}\right)^2 \exp\left(\frac{E_b - E_a}{k_B T}\right), \tag{4.8}$$

where c_a and c_b are the hopping rates for two arbitrary processes, a and b, as described by Equation 4.2 d_a and d_b are the respective hopping distances. Graph 4.7 shows how this ratio varies with temperature for $\frac{c_1}{c_2}$, which is the along channel diffusion divided by the across channel diffusion. The ratio is a very large number in this temperature range, and decreases exponentially. This shows that for very high temperatures the hopping ratio of the different processes decreases, such that at higher temperatures an increasing number of processes become dominant.

Figure 4.8 shows this hopping ratio for $\frac{c_1}{c_3}$, which is the along channel diffusion rate divided by the along channel boiling rate. The ratios are smaller, but still

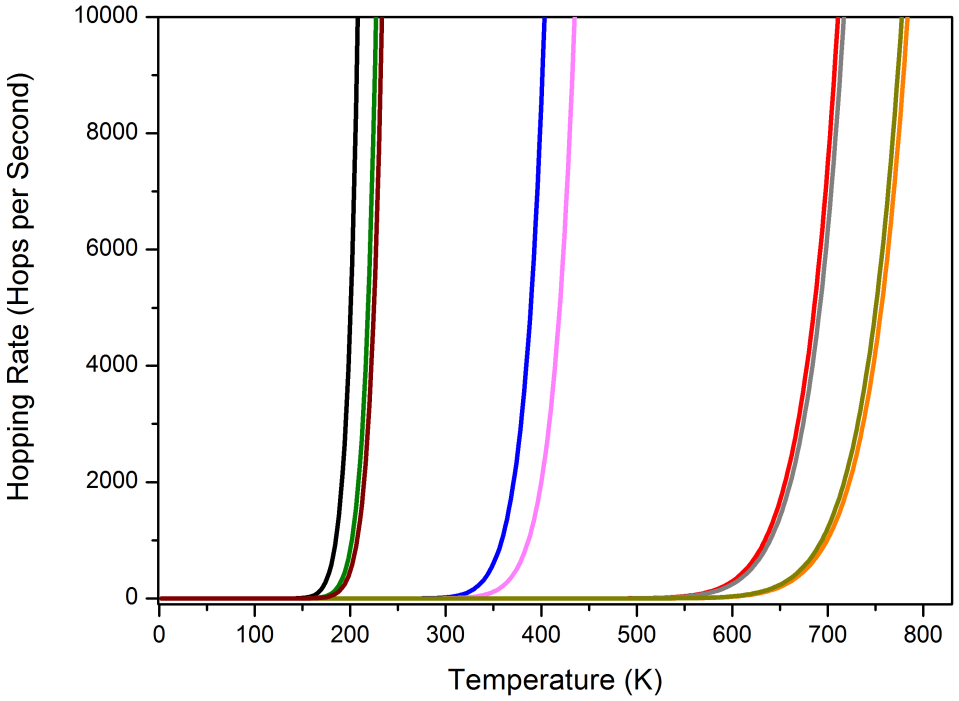

Figure 4.6 Adatom hopping rate as a function of temperature for process 1 (black), 2 (red), 3 (blue), 4 (orange), 5 (green), 6 (dark grey), 7 (pink), 8 (dark yellow), and 9 (dark red) corresponding to Table 4.1.

very high in this temperature range, which is to be expected as the energy barriers for these processes are more similar.

This leads us to conclude that by varying the surface temperature between 0K and ≈1000K the balance between in-channel diffusion and recombinations could change significantly, without the importance of dimer dissociation or cross-channel diffusion changing as these are only significant at very high temperatures.

4.3.2 Molecular Dynamics Calculations

MD has previously been used to predict nanostructuring in Ni and Cu crystals [11, 12, 73] and crater annihilation [13] (which is the recombination of surface vacancies and adatoms).

MD simulations utilise empirical fits to the equations of motion to simulate a many body system. This is done by evaluating the forces present on each particle at any one time to determine the position, $r(t + \Delta t)$, and velocity , $v(t + \Delta t)$, of a particle, where $r = \sqrt{x^2 + y^2 + z^2}$ and Δt is the integrated time step. The

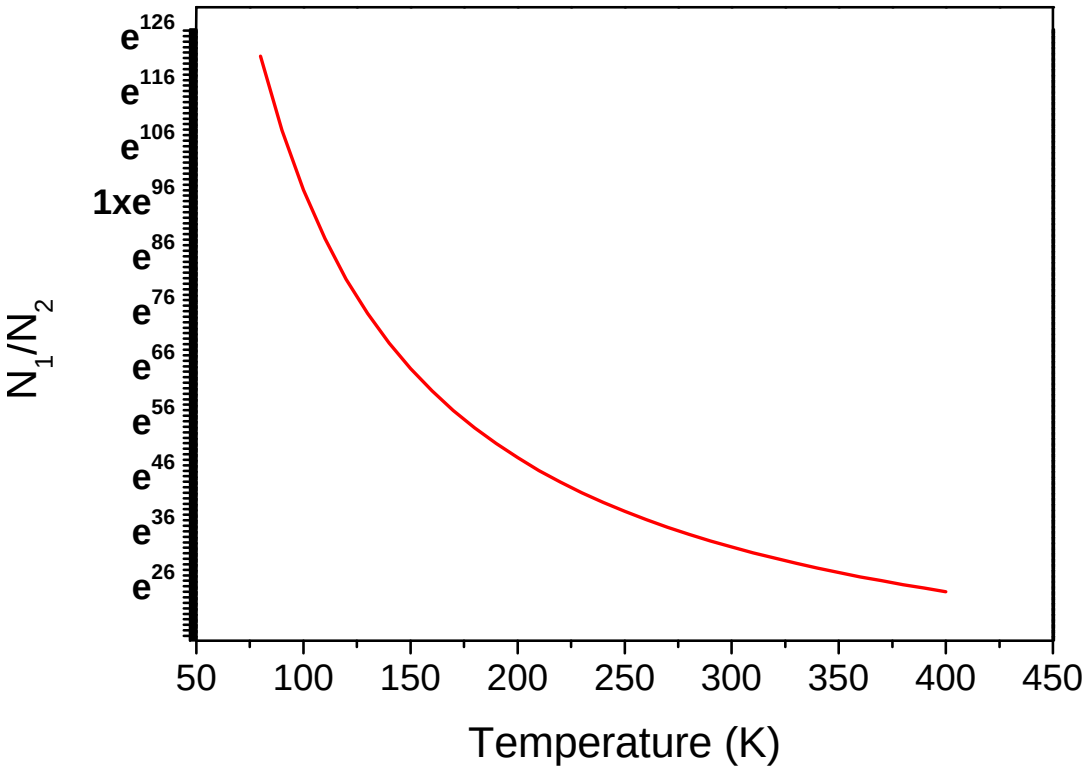

Figure 4.7 The relationship between the adatom hopping ratio of $\frac{c_1}{c_2}$ (the along channel diffusion over the across channel diffusion) and temperature.

force on each particle is then

$$F_{i\alpha} = m\frac{d^2 r_{i\alpha}}{dt^2} = -\frac{\partial E}{\partial r_{i\alpha}}\,, \tag{4.9}$$

where i is the atom being considered, F_i is the force on i, E is the potential energy, and α represents the coordinates in x, y, and z. MD simulations solve these equations numerically for a large system of particles.

The simulation results by Lane *et al.* [14] used in this thesis as the input parameters to the KMC simulation utilised the MOLDY code [74] with 250,000 atoms. The Finnis-Sinclair potential well [75, 76], which has been used previously to model surfaces and cascades [77–79], was used. This model splits the potential energy of each atom into a screened Coulomb repulsion term and a second moment tight binding term. They simulated the experimental conditions at 144K by using the Cu(110) surface, with periodic boundary conditions in the [001] and [1$\bar{1}$0] directions, and started with a 500eV Ar ion at 5° off surface normal and 3.5 Å above the surface. The simulation was run for 10ps before the ion was introduced and then simulated until all damage had settled which took around 2-3ps. The

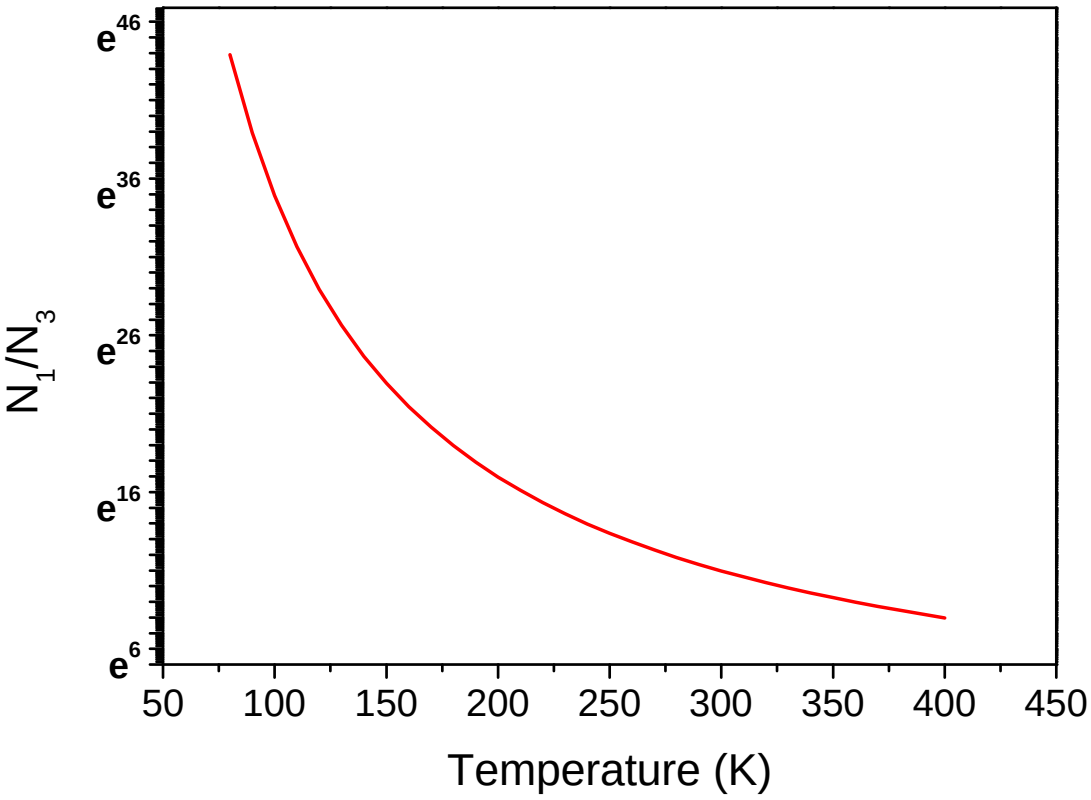

Figure 4.8 The relationship between the adatom hopping ratio of $\frac{c_1}{c_3}$ (the along channel diffusion over the along channel boiling) and temperature.

simulation was run 90 times so that statistics could be gathered.

Input Parameters from MD Results

As well as surface energy barriers MD simulations can give other parameters as an input to the KMC simulation; these are [14]:

- Adatom ejection range = 8 unit cells.
- Vacancy ejection range = 4 unit cells.
- Adatom sputter yield = 10 adatoms.
- Vacancy sputter yield = 9 vacancies.

These values are used in the simulation to recreate the experimental conditions, with the sensitivity of each parameter on the outcome of the simulation further explored in Chapter 5.

4.4 Analysis Techniques

In order to simulate the RAS intensity the Poelsema-Comsa model has been incorporated into the program. Also, to allow for comparison with experimental STM and MD simulation data a cluster counting algorithm has been implemented. Both of these analysis techniques are described below.

4.4.1 Implementing the Poelsema-Comsa Model

To compare simulation to experimental RAS data the Poelsema-Comsa model has been implemented. This is achieved by placing a 2D lattice patch over each defect on the surface, where the area within each patch does not contribute towards the RAS intensity as described in Section 3.3. The active surface fraction is then calculated using Equation 3.5 by counting the 'undamaged' lattice sites (*i.e.* the sites which are not within a patch) and dividing by the total number of lattice sites. This number is directly proportional to the normalised RAS intensity.

Ideally we would model an infinite sized lattice but, as this is not possible due to computing restrictions, finite lattices are modelled. In doing so boundary issues arise where a defect is close to the edge of the simulated lattice so that the RAS patch associated with that defect is outside the boundaries of the simulation, and so will not contribute to the destruction of the RAS signal. A way to avoid this is to use periodic boundary conditions where the patch wraps around and appears on the opposite side of the lattice; this has therefore been implemented into the program.

4.4.2 Cluster Analysis of Defects on the Surface

In order to compare STM and MD simulation results to KMC results a cluster counting algorithm has been incorporated into the simulation. This algorithm records the number of adatom clusters and also how many adatoms are in each cluster. An adatom is counted as being part of the same cluster of another adatom if they are either one site above or below, or one site left or right of each other.

This algorithm gives a true value of the size and number of different clusters. However, this may not give comparable results to STM data because the

resolution of the images may make it hard to distinguish between adatoms next to each other and adatoms which are near each other. This is described in more detail in Section 3.4.2.

4.5 Preliminary Results

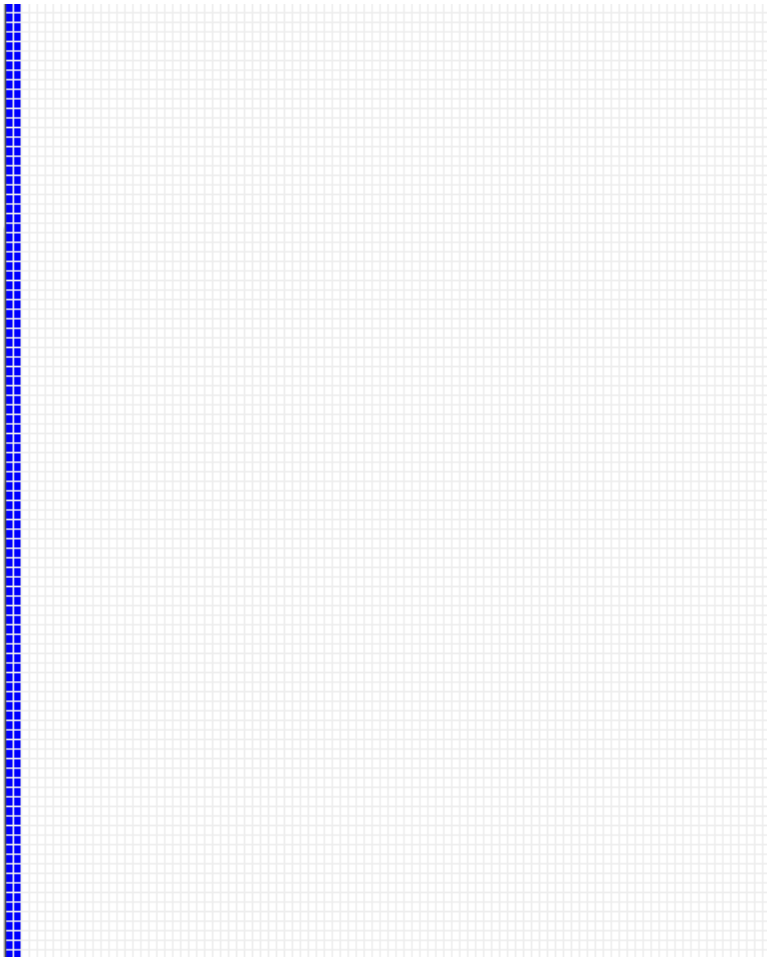

Figure 4.9 The initial surface at time $t = 0$.

The initial surface consists of a 100×100 unit cell lattice with a step edge to the left made up of 2 adjacent adatoms as shown in Figure 4.9. Adatoms placed on the surface interact with the step as though the adatoms at the step were double dimers, such that they can 'stick' to the step creating a 'sink' for the adatoms, but can also diffuse away. Adatoms, however, cannot diffuse over the step edge up to the higher terrace. The right side of the lattice is a step down where adatoms can not 'hop' over the step as at the temperatures studied the probability of this process occurring is very low.

Figure 4.10 shows preliminary results of the simulation at 183K as well as experimental data taken at the same temperature. The surface was ion bombarded for 12 seconds and the normalised RAS intensity calculated using the Poelsema-Comsa model described in Sections 3.3 and 4.4.1. The graph shows a decay in the peak, which is very similar to experimental results, indicating the simulation is producing sensible results.

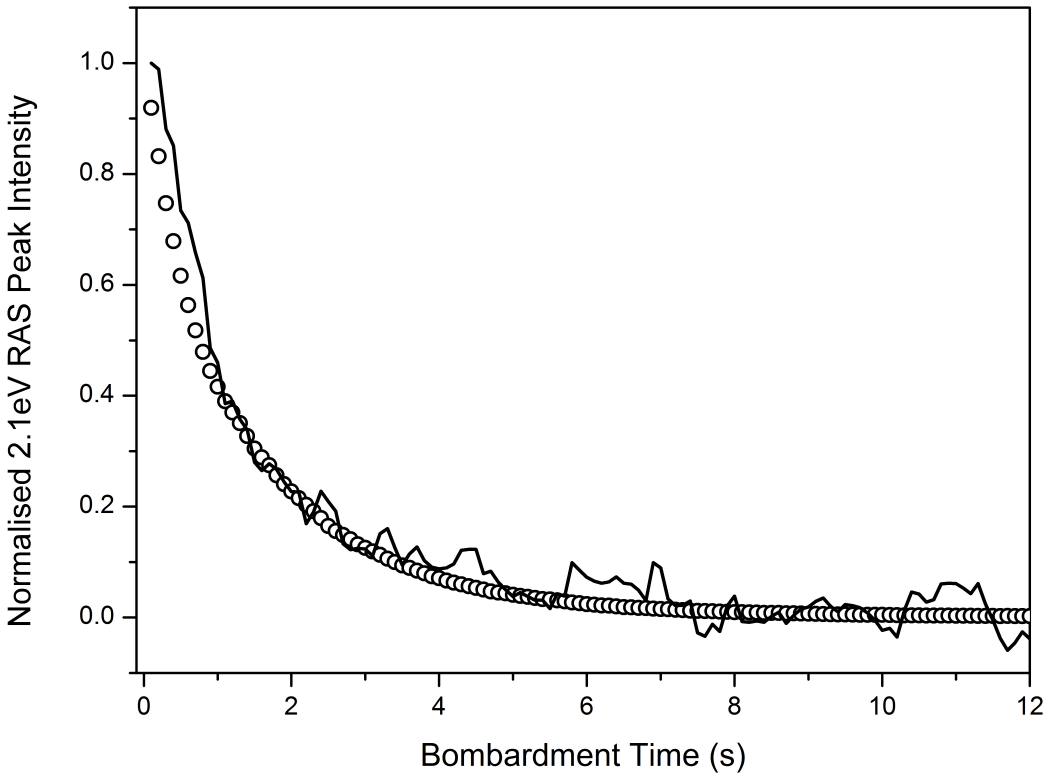

Figure 4.10 Preliminary results of the simulation showing the RAS intensity vs ion bombardment time. Experimental results (solid line) were taken at 183K. The simulation (open circles) was run at 183K, on a 100x100 lattice with a step edge, and a patch per defect size of 49 unit cells. Error bars are not included as they are too small.

Figure 4.11 shows the simulated surface after 2 seconds of ion bombardment and the same bombarded surface after 30 minutes of diffusion. The surface looks distinctively different after 30 minutes, such that the defects have created large clusters, adatoms have joined the step edge, and some adatoms and vacancies have recombined.

Further testing results are presented in Chapter 5, with surface simulation results presented in Chapters 6, 7, and 8.

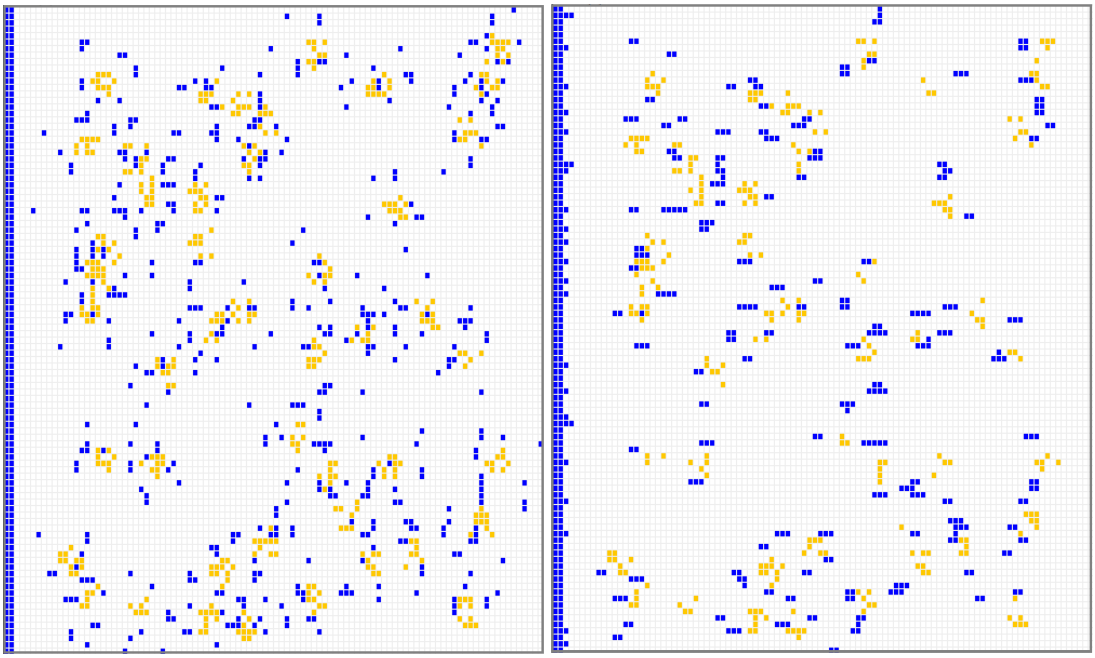

(a) The simulated surface after 2 seconds of ion bombardment.

(b) The simulated ion bombarded surface after 30 minutes of diffusion.

Figure 4.11 Preliminary results of the program showing the simulated lattice 2 seconds after ion bombardment and the same lattice after 30 minutes of diffusion with adatoms shown as blue and vacancies as orange. A step edge is created using 2 rows of adatoms.

Chapter 5

Simulation Testing

5.1 Introduction

Having shown in the previous chapter that the simulation produces sensible results, it is now important to test the program to understand its sensitivity to input parameters and also to further understand its limitations. This will confirm that the program behaves sensibly and also confirm its robustness and sensitivity to these parameters.

5.2 Functionality Testing

To confirm the simulation behaves sensibly and consistently the effect of varying the simulation size (the number of unit cells within the simulation), ion flux, and patch per defect shape has been tested. The lattice size should not affect results beyond the size needed for good statistics. Ion flux should have a fairly predictable effect on the RAS signal as, repeated here from Equation 3.3, $I = (1 - \theta(t))^{\Sigma_I}$ where θ is the impacts per unit cell which is a function of time, t. Taking the basic tests as 'passed' and trusting the programming algorithms, as well as its limitations, we can move forward.

5.2.1 Ion flux

The simulation was tested to verify the effect of varying ion flux on the RAS intensity. Figure 5.1 shows the results of this at 0K plotted on a time axis. As flux increases, the peak decays more rapidly. The behaviour, as expected, is described by Equation 3.3.

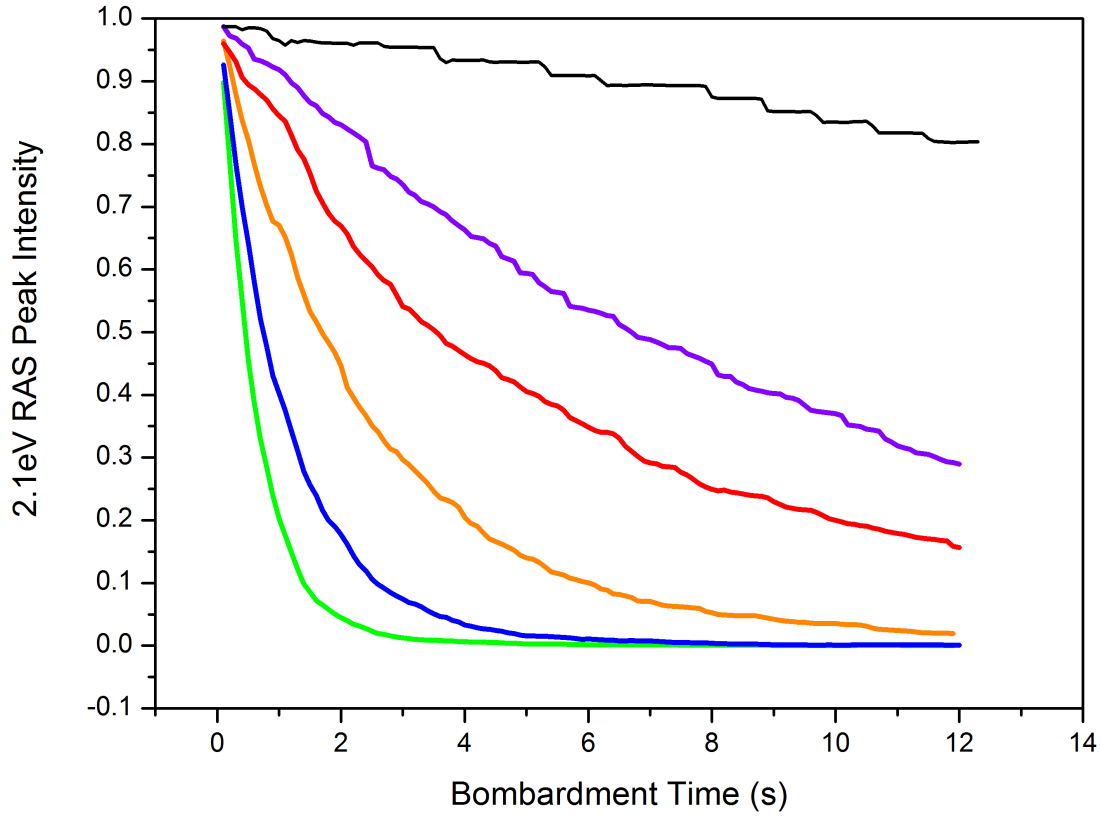

Figure 5.1 The decay of the RAS intensity with varying with flux at 0K. 0.0001 (black) 0.00055 (purple) 0.001 (red), 0.0025 (orange), 0.005 (blue), and 0.01 (green) ions/unit cell/s .

As the data is taken at 0K, so that there is no diffusion occurring on the surface, upon converting the x axis to impact density the data should coincide. This is this is confirmed with data shown in Figure 5.2, telling us that when bombarding the lattice with different fluxes the simulation responds as expected.

5.2.2 Lattice Size

The lattice was tested for robustness against changing the lattice size. Potentially boundary conditions could affect the resultant RAS intensity of the surface at any

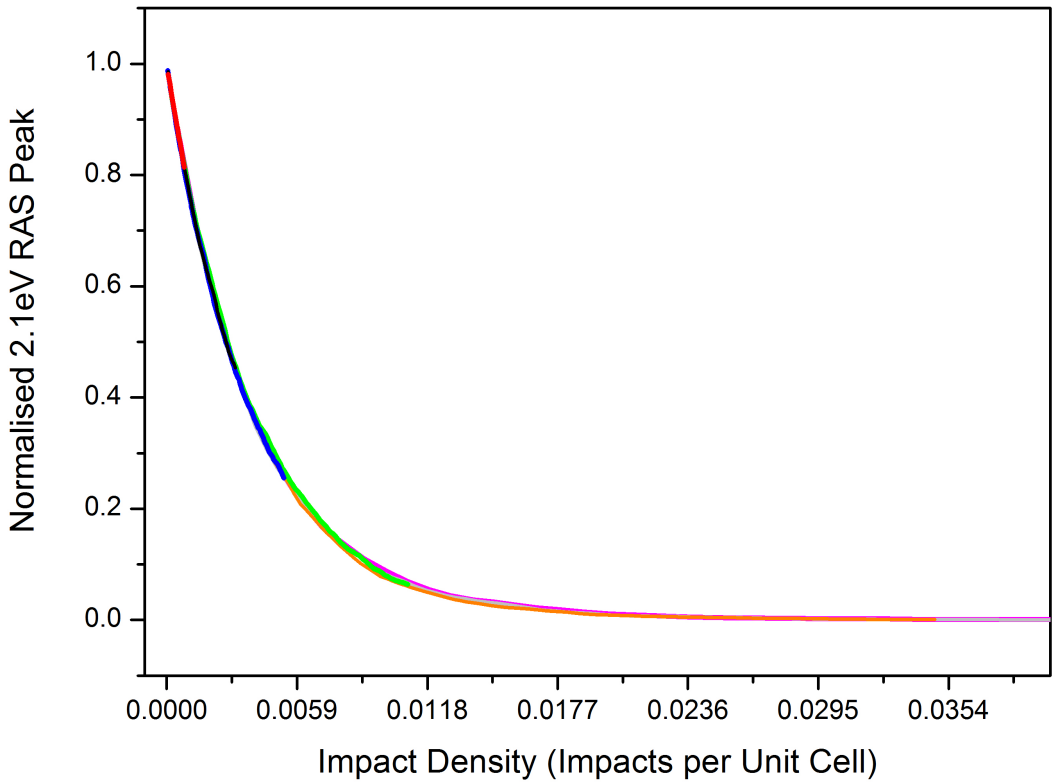

Figure 5.2 The decay of the RAS intensity vs impact density with varying flux at 0K for fluxes of 0.0001 (red), 0.0003 (black), 0.0005 (blue), 0.001 (green), 0.003 (orange), 0.005 (grey), and 0.01 (purple) ions/unit cell/s.

one time, and this may be the case for a small lattice. Results of this test are shown in Figure 5.3. No identifiable difference between the simulation results for each lattice size can be seen.

5.2.3 Dependence on Defect Patch Shape

The sensitivity of the program on the patch per defect shape has been tested, using a patch of 49 unit cells. The patch shape was varied by using a rectangle with sides of 7×7 unit cells, and a 'star' shaped patch with the same area shown in Figure 5.4.

The results of simulations with different patch sizes are shown in Figure 5.5. These results show that the program behaves the same regardless of patch shape, as is expected.

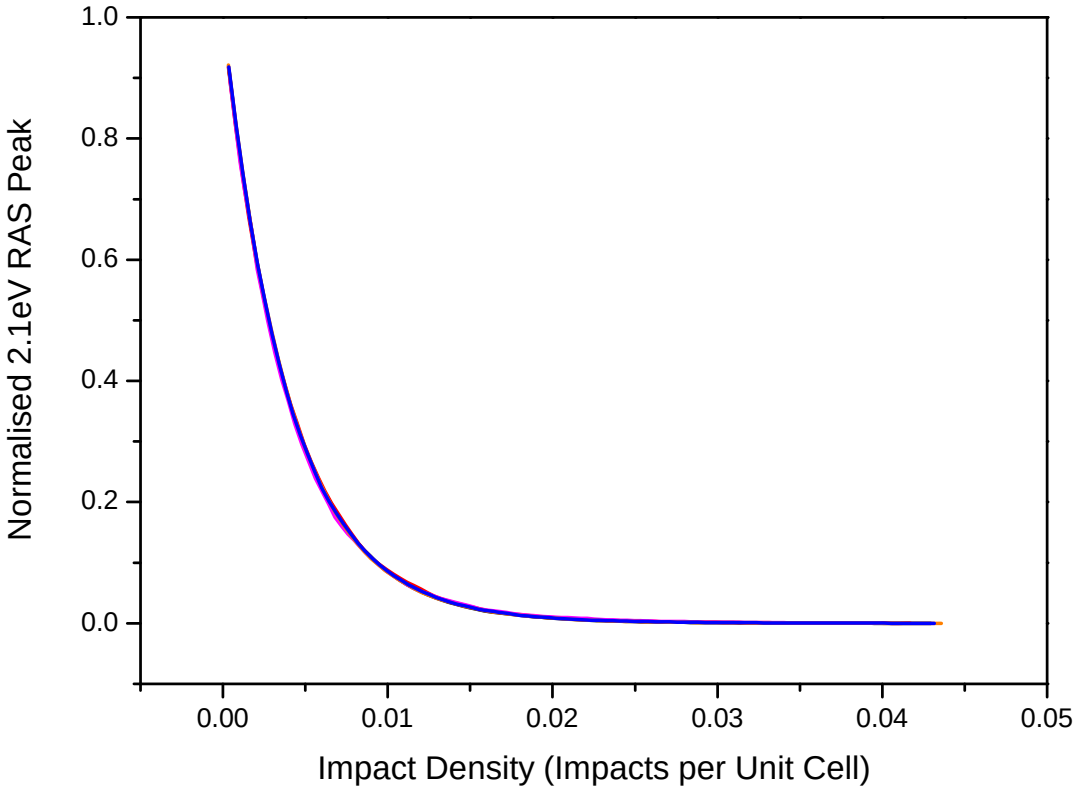

Figure 5.3 The simulated normalised RAS intensity during ion bombardment for lattice sizes of 150×150, 200×200, 300×300, 350×350, and 400×400.

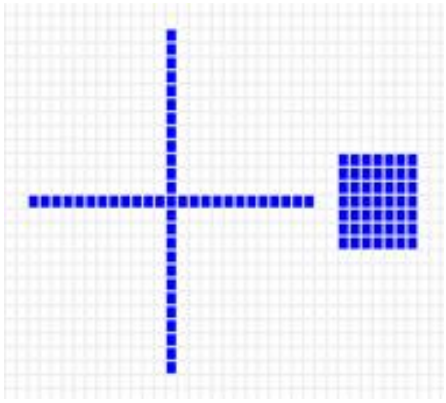

Figure 5.4 A star and square patch used in the Poelsema-Comsa model.

5.3 Sensitivity to Input Parameters

To test robustness and sensitivity of the program to input parameters from MD simulations the effect of energy barriers, defect ejection range, patch size, and adatom-vacancy recombinations have been tested. It is useful to know the sensitivity to these parameters and important to understand how robust the

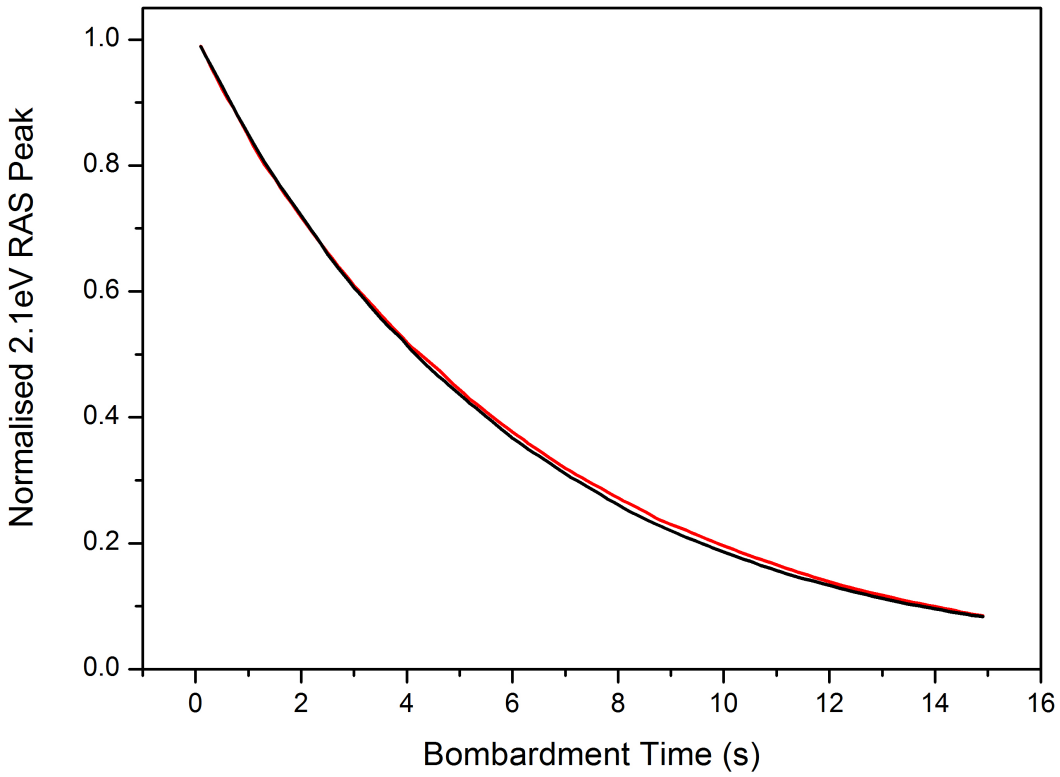

Figure 5.5 The RAS intensity vs bombardment time with a square (black line) and star (red line) RAS patch.

simulation is against them. This will allow us to understand how uncertainties in values affect the results, as well as telling us which parameters play key roles in the destruction of the RAS intensity and the nanostructuring of the surface.

5.3.1 Patch Per Defect Size

Figure 5.6 shows results which tell us how the peak decay changes with varying the patch per defect size, Σ_d. This has the effect of changing the total patch per impact size where $\Sigma_I = f(\Sigma_d)$. As expected, by inspecting Equation 3.3, with increasing defect patch size the 2.1eV peak decays more rapidly.

The peak decay is affected quite drastically with varying patch sizes. This implies the extent of RAS decay is highly dependent on the electron scattering effect of a defect.

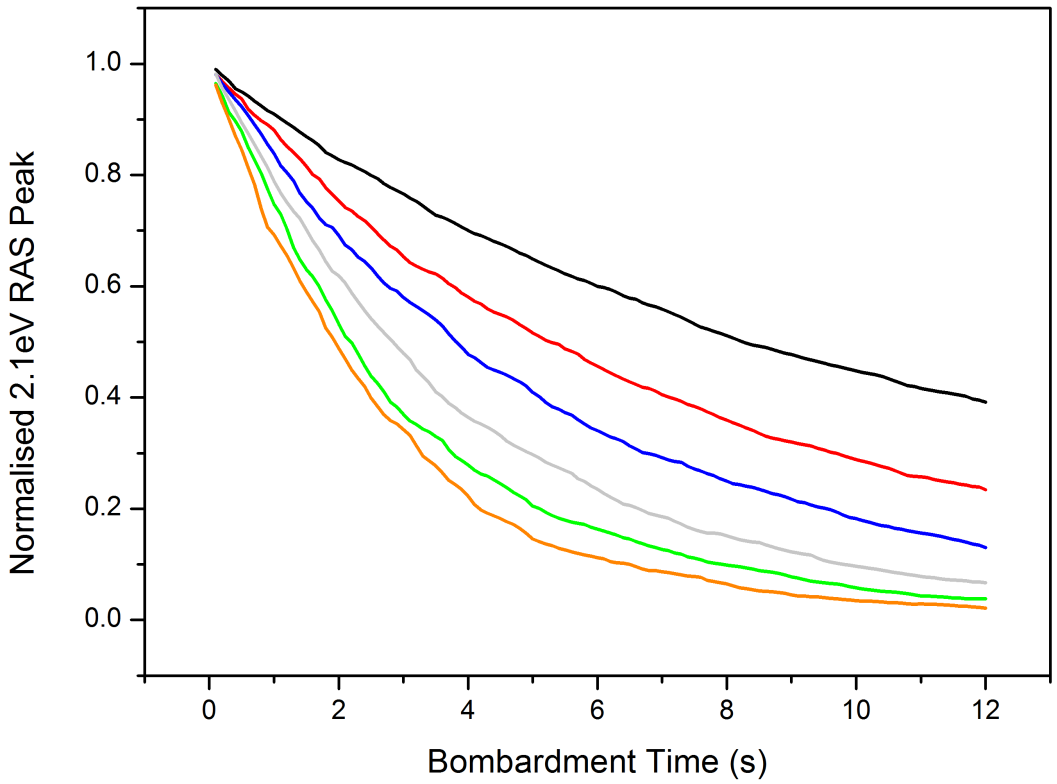

Figure 5.6 The RAS intensity vs bombardment with varying patch per defect size. Simulated at 144K with ion flux of 0.0014 ions/unit cell/second, with patch per defect sizes of 2x2 (black), 3x3 (red), 4x4 (blue), 5x5 (grey), 6x6 (green), and 7x7 (orange) unit cells.

How Impact Patch Size Varies with Defect Patch Size

As each impact site consists of a distribution of defects and each defect has a corresponding patch size, Σ_d, associated with it, it is of interest to know the effect increasing the defect patch size has on the total patch size of the impact, Σ_I, the results of this are shown in Figure 5.7. The data was created by simulating the surface at a temperature of 0K and using a least squares fit to fit the Poelsema-Comsa equation to the RAS intensity vs bombardment time data in order to calculate the patch per impact Σ_I .

It is expected that for a large patch per defect size that the patch per impact would increase linearly. This is because there is complete overlap in the centre of the impact site with the increasing size only contributing to the damage outside the adatom ejection range. This is what is found in Figure 5.7 where for patch per defect sizes of over 20 unit cells the patch per impact increases approximately linearly.

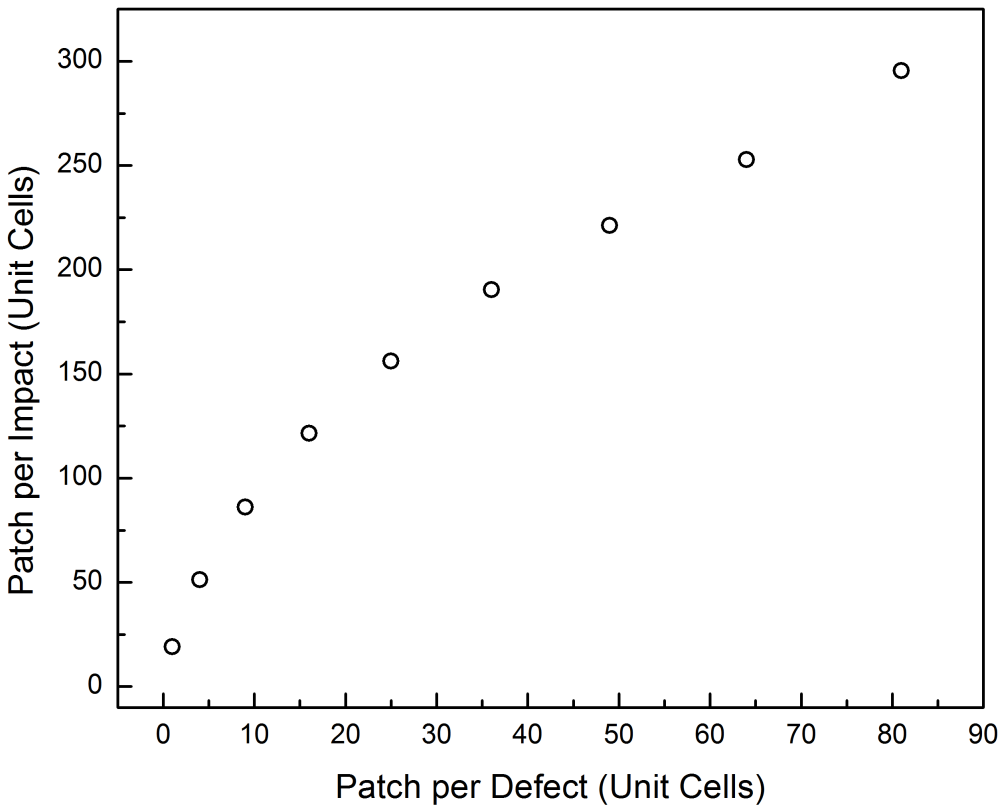

Figure 5.7 The patch per impact area vs patch per defect area. Error bars too small to include.

5.3.2 Ejection Range

The ejection range of the adatoms and vacancies are taken from MD results as explained in Section 4.3.2. Figure 5.8 shows the results of varying the ejection range of the adatoms while all other parameters are kept constant.

The results suggest that the 2.1eV peak decay is not sensitive to changes in the ejection range for values over 8 unit cells. The literature suggests a value of 8 unit cells [14] for the adatom ejection range so the associated error on this value should not affect the simulation outcome.

5.3.3 Surface Energy Barriers

The energy barriers used in the KMC simulations input parameters are taken directly from MD results as described in Section 4.3.1. It is again important to know the sensitivity of the program to a change in these barriers.

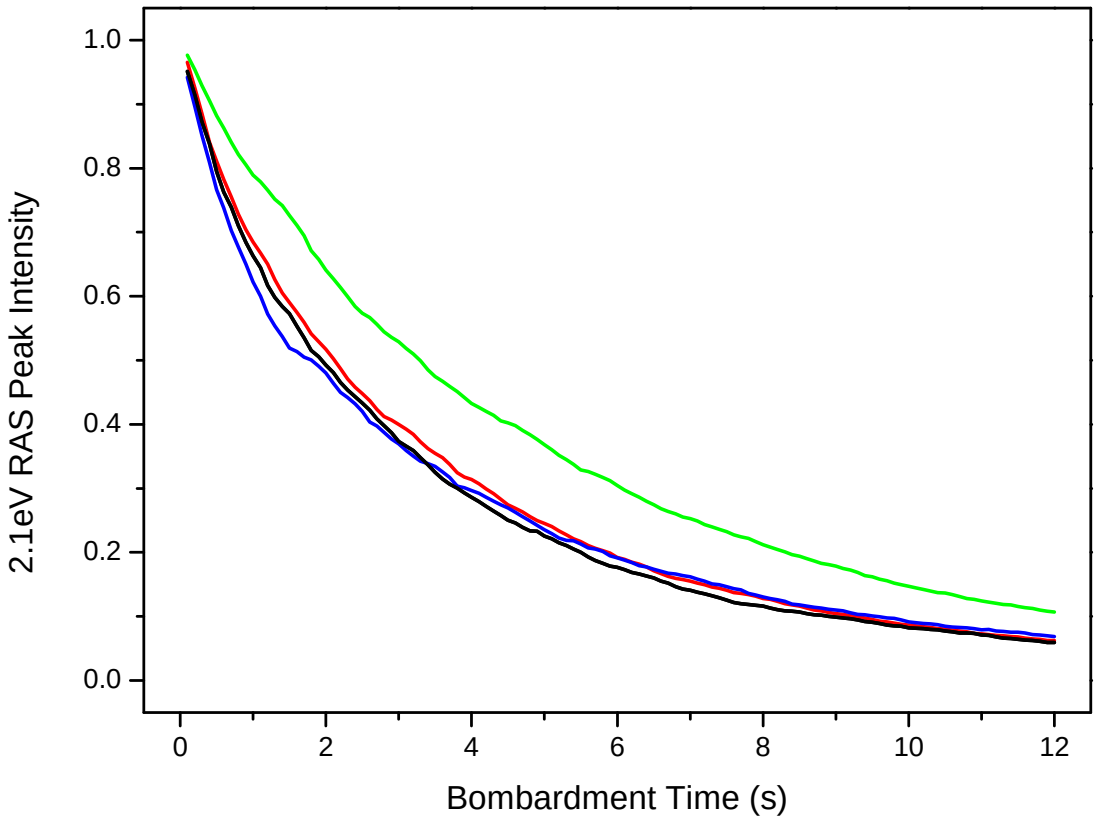

Figure 5.8 Simulation results of the RAS intensity vs bombardment time for adatom ejection ranges of 5 (green), 8 (red), 10 (black), and 15 (blue) unit cells.

Changing Energy Barriers by a Fixed Percentage

Changing the surface energy barriers by a fixed percentage should have an inverse effect to changing the temperature of the lattice as, repeated here from Equation 4.1 ,

$$D = D_0 \exp\left(-\frac{\Delta E}{k_B T}\right), \tag{5.1}$$

such that lowering the energy barriers would have the same effect as increasing the temperature.

Figure 5.9 shows the results for this, where lowering the energy barriers equally does indeed affect the peak such that it decays less quickly.

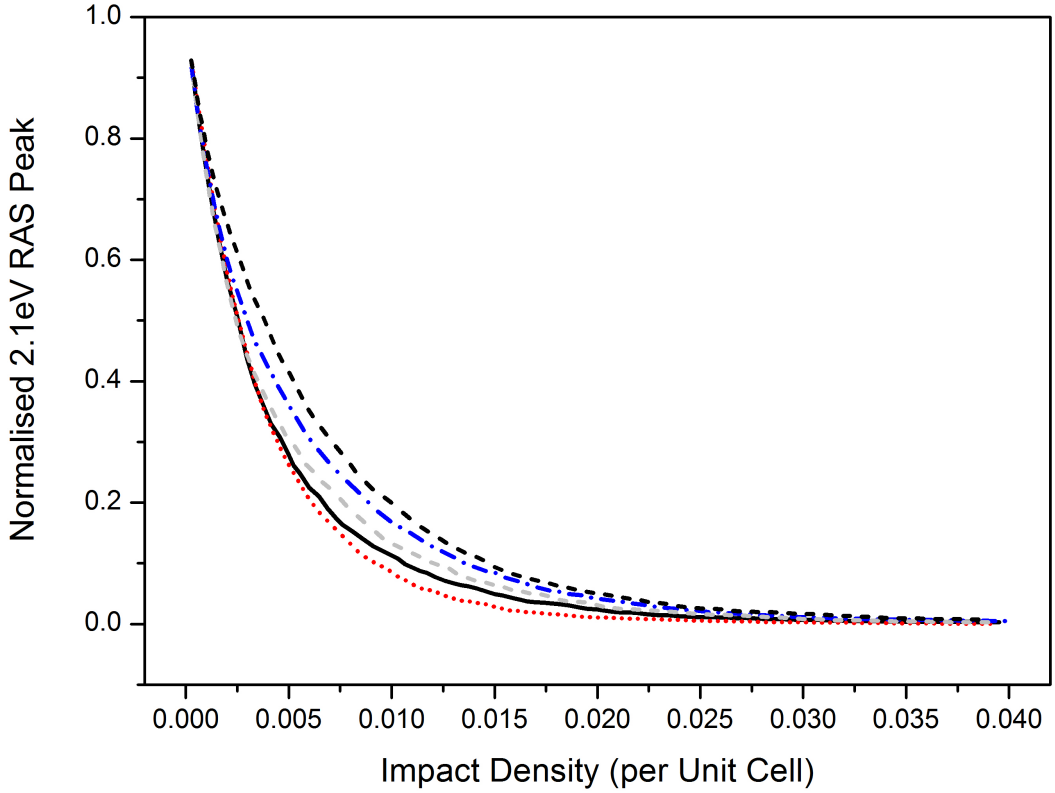

Figure 5.9 Sensitivity of the 2.1eV peak intensity vs bombardment time to energy barriers at 183K. Cu(110) energy barriers (blue dot dash), 10% lower (black dash), 5% higher (grey dash), 10% higher (black solid line), 25% higher (red dots).

Creating a 1-Dimensional Lattice

Diffusion in the [100] direction (across the channels) was 'frozen out' so that adatoms could only move in the $[1\bar{1}0]$ direction (along the channels) and also any 'boiling off' $[1\bar{1}0]$ energy barriers were set to non 'boiling off' energies (*i.e.* in Figure 4.5 the energy barriers of processes 2, 4, 6, and 8 are set to infinity such that these processes will not occur, and process 5 = 1 and 7 = 3). This was to test whether at low temperatures the surface behaves in as a 1 dimensional lattice, with results shown in Figure 5.10.

The difference between the the 1D and 2D lattice seem to be negligible at 183K. This shows the movement of the adatoms and key processes at this temperature only occurs in the $[1\bar{1}0]$ direction, which may not be the case though at higher temperatures. This makes sense as, as discussed in Section 4.3.1, at low temperatures the along channel processes dominate.

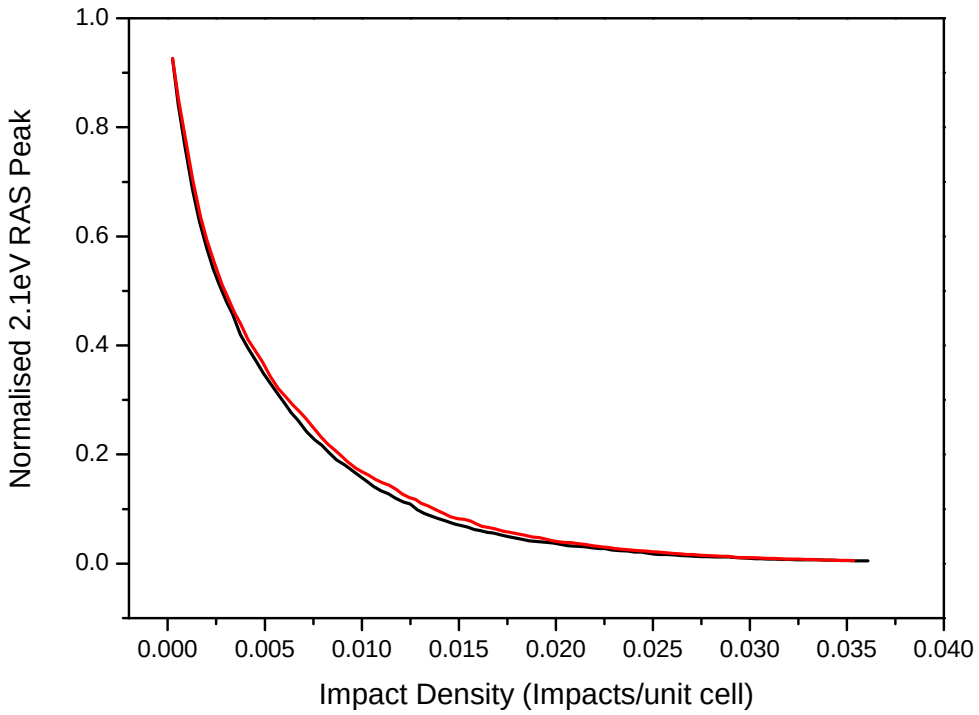

Figure 5.10 The RAS intensity vs impact density at 183K for a 1D (black) and 2D (red) lattice.

5.3.4 Effects of including Adatom-Vacancy Recombinations

A process which has been included in the simulation due to its role in surface repair is adatom-vacancy recombination (process 9 seen in Figure 4.5). The effects of this have been tested by removing the process from the model, with results shown in Figure 5.11.

The results show that at 183K adatom-vacancy recombinations play an important role in the nanostructuring of the surface. As expected the decrease in the 2.1eV peak is faster with no recombinations. This is because recombinations help to repair surface anisotropy and therefore restore the 2.1eV peak intensity.

Figure 5.12 shows the simulated surface with the same flux with (a) and without (b) adatom-vacancy recombinations. It is obvious upon inspection of the two images that the recombinations affect the surface nanostructure considerably.

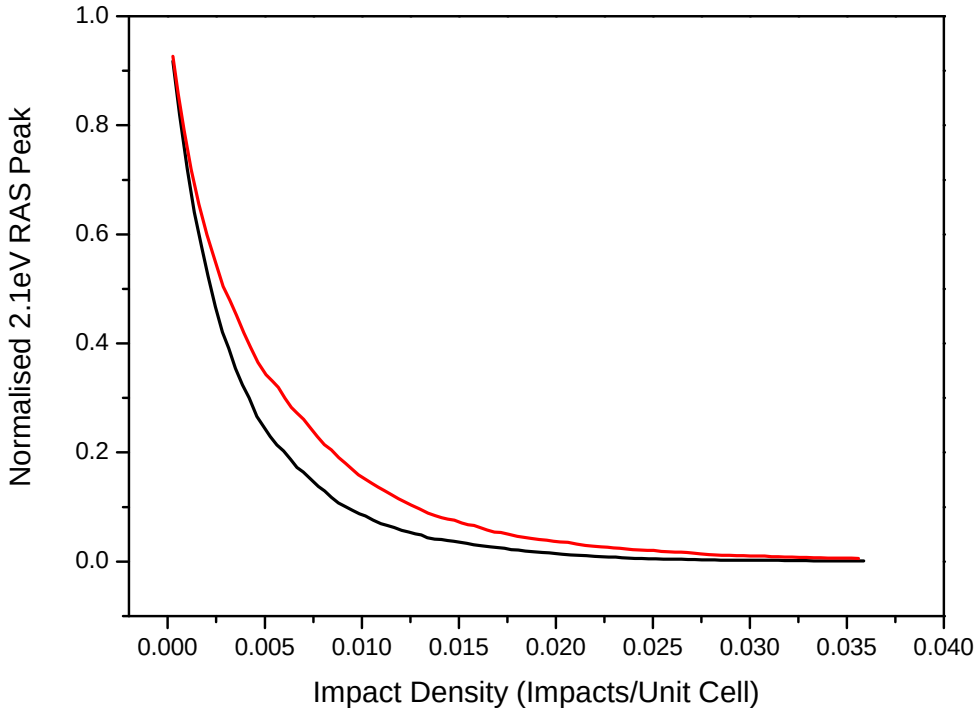

Figure 5.11 The RAS intensity vs impact density at 183K with (red) and without (black) adatom-vacancy recombinations.

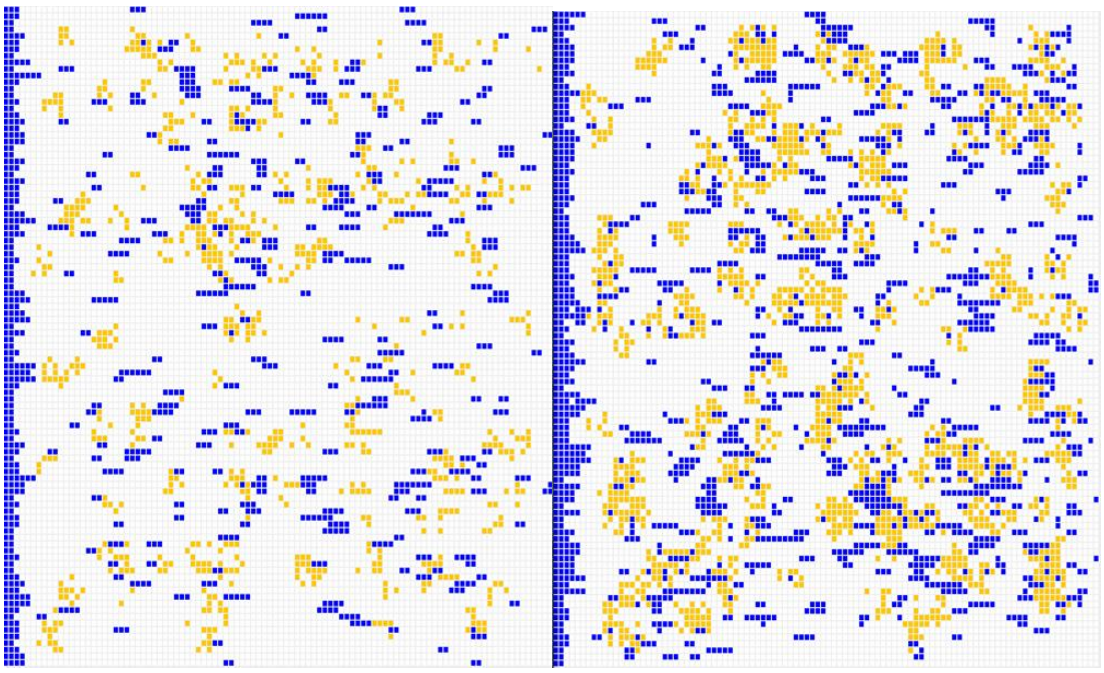

(a) The simulated surface after 12 seconds of ion bombardment with adatom-vacancy recombinations.

(b) The simulated surface after 12 seconds of ion bombardment without adatom-vacancy recombinations.

Figure 5.12 Simulation results of the surface bombarded with an ion flux of 0.0014 ions/unit cell/second with adatoms shown as blue and vacancies as orange. A step edge is created using 2 rows of adatoms.

Chapter 6

Modelling the RAS signal of the Ion Bombarded Cu(110) Surface

6.1 Introduction

The ion bombarded Cu(110) surface has been simulated using the KMC simulation described in Chapter 4. Simulations were carried out in order to replicate experimental conditions used in published results [54], in doing this the aim is to understand defect kinetics of the Cu(110) further. Ideally we would like to demonstrate that RAS can reveal the defect distribution, this would mean 'inverting' experimental data, which is not possible. Similarly, simulations cannot completely reproduce experiment since some parameters are not known precisely. But experiment can guide simulations, and simulations can interpret experiments.

A new type of analysis is also presented in this chapter where the patch per ion impact, Σ_I, is monitored over bombardment time for experimental and simulation data. This method presents a new complex analysis which may give further insight to the diffusion mechanisms on the surface, and a direct way of measuring diffusion using RAS data, though analysis of this seems non-trivial.

6.2 Optimising Ion Flux and Patch per Defect Size

There are some remaining input parameters that need to be optimised using the experimental data. The ion flux for each experimental data set is required as the flux is probably not stable, as discussed in Section 2.2.4, and in order to accurately recreate experimental data we need to know the ion flux. Also required is the patch per defect, Σ_d, size. This is calculated by manual refinement where the patch per defect size is changed until the best fit to experimental data is found. Both of these methods and results are presented below.

6.2.1 Calculating the Ion Flux

As discussed in Section 2.2.4 the ion gun may not be stable when first switched on. This leads to large uncertainties when measuring the ion flux. The flux can be better calculated by using the experimental RAS intensity data.

In the initial stage of ion bombardment of the clean surface it is likely that the ion impacts will land far apart from each other. This means the 'RAS patch' from each impact, Σ_I, will not overlap, and at low temperatures we can assume the patch size is constant over time. This leads to a linear decrease in the RAS intensity for a low bombardment time. This can be shown by considering the differential of Equation 3.3 for small time, t,

$$\frac{dI}{dt} = -\frac{d\theta}{dt}\Sigma_I \,, \tag{6.1}$$

where $\frac{dI}{dt}$ is the slope, Σ_I is the patch per impact size in unit cells, and $\frac{d\theta}{dt}$ is the rate of change of the ions impacting the surface (the ion flux), where θ is the number of ions that have impacted the surface at time, t.

A linear fit to the experimental data at 183K with bombardment time of 0 to 1 second is shown in Figure 6.1. The linear fit gives a slope of $\frac{dI}{dt} = -0.644 \pm 0.027$ s^{-1}, using Equation 6.1 and for a value of $\Sigma_I = 170$ unit cells [54] the flux is calculated to be

$$\frac{d\theta}{dt} = (3.79 \pm 0.16) \times 10^{-3} \text{ ions unit cell}^{-1}\text{s}^{-1} \,. \tag{6.2}$$

Using this method the flux can be calculated for the experimental data at different

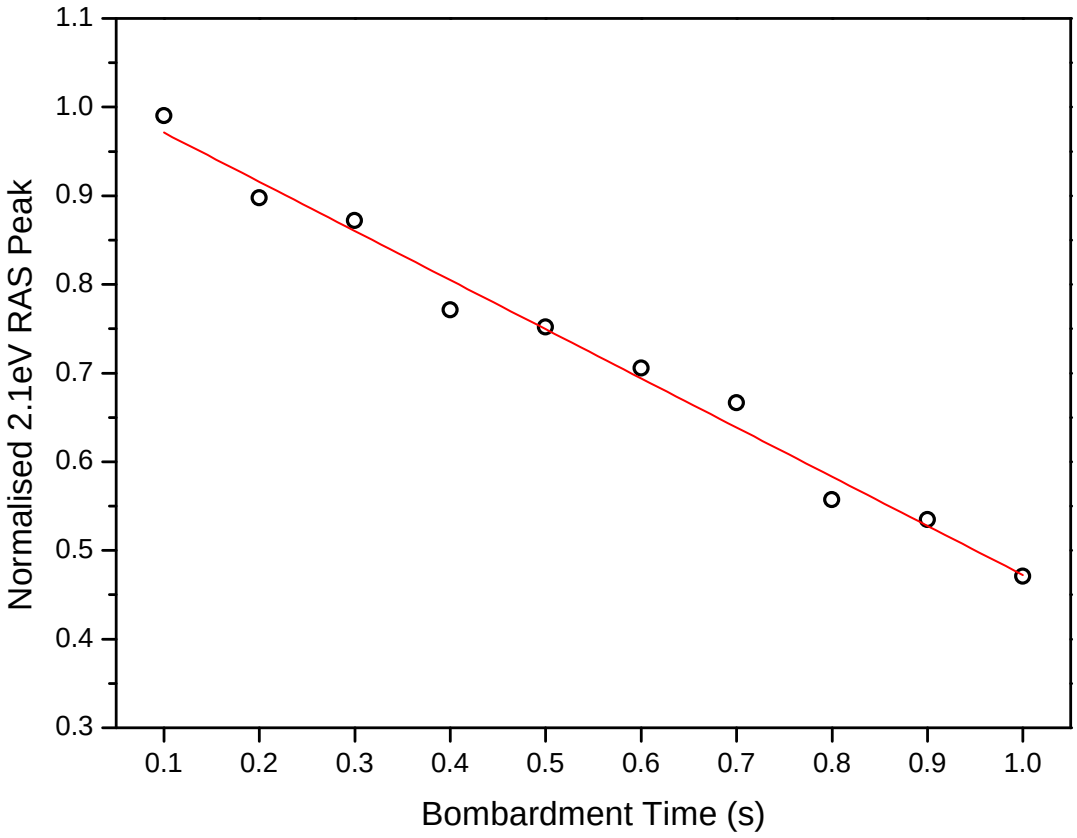

Figure 6.1 The RAS intensity for low bombardment time (open circles) with a linear fit (red line) to the data.

temperatures, the results of this are shown in Table 6.1. This method assumes a constant patch per impact size which is appropriate for low temperature results. At higher temperatures, in this case over 243K, the slope is not linear for low t and therefore measuring the flux this way is not appropriate.

Temperature (K)	Flux (ions/unit cell/s)
183	$(3.8 \pm 0.2) \times 10^{-3}$
203	$(6.4 \pm 0.6) \times 10^{-3}$
223	$(4.5 \pm 0.2) \times 10^{-3}$
243	$(1.6 \pm 0.1) \times 10^{-3}$

Table 6.1 The calculated flux for each experimental data set varying with temperature.

6.2.2 Patch Per Impact Optimisation

Surface ion bombardment was first simulated at 183K as this is the lowest temperature experimental data available for comparison. As the diffusion coefficient for each process

$$D \propto \exp\left(-\frac{1}{T}\right), \tag{6.3}$$

lower temperatures, T, lead to a lower surface activity, λ, as is apparent by combining Equation 4.2 and 4.3. This leads to simulations that run faster due to there being less hops per second on the surface as

$$t_s \propto \left(\frac{1}{\lambda}\right), \tag{6.4}$$

where t_s is the time step of a reaction occurring. For this reason the 183K data was used for patch per defect optimisation.

The simulation can be used to estimate the patch per defect size, Σ_d, by optimising to match experimental data at 183K. This is achieved by using the flux calculated in the last section, $\frac{d\theta}{dt} = (3.79 \pm 0.16) \times 10^{-3}$ ions unit cell^{-1}s^{-1}, and using the input parameters from MD simulations described in Section 4.3.2 as well as surface energy barriers outlined in Section 4.3.1.

Figure 6.2 shows the simulation results of changing the patch per defect size with the experimental result at 183K. It is clear that a patch per defect Σ_d between 6×7 and 7×7 unit cells fit the data more closely. A patch per defect area of 7×7 unit cells has therefore been used in subsequent simulations.

This is in much better agreement with experiment than previous results [54], shown in Figure 3.9 which shows it is important to consider diffusion when simulating the RAS intensity data. The size of the patch per defect calculated using the simulation is also consistent with other studies [22, 54] which indicates a correct distribution of adatoms.

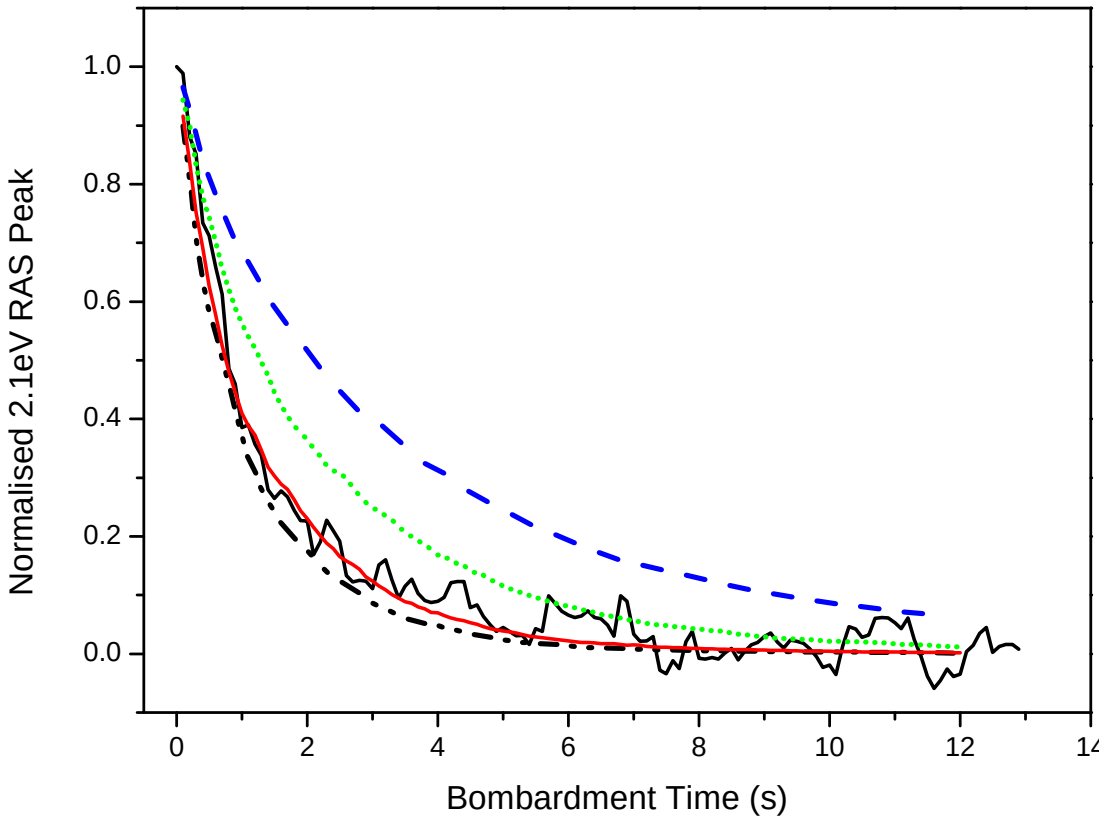

Figure 6.2 The normalised RAS intensity with bombardment time for experimental data (black line), and simulated data with patch per defect sizes of 4×4 (blue dashed), 6×6 (green dots), 7×7 (black dash dot dot), and 6×7 unit cells (red line) at 183K.

6.3 Modelling the RAS Intensity for Various Temperatures

Having optimised the patch per defect using the low temperature experimental data in Section 6.2.2, and having calculated the flux for experimental data at various temperatures in Section 6.2, it is now possible to model the experimental data. Presented here are results of modelling the data with the Poelsema-Comsa fit using Equation 3.4 and using the Poelsema-Comsa method in the KMC simulation to recreate the surface and model the RAS intensity.

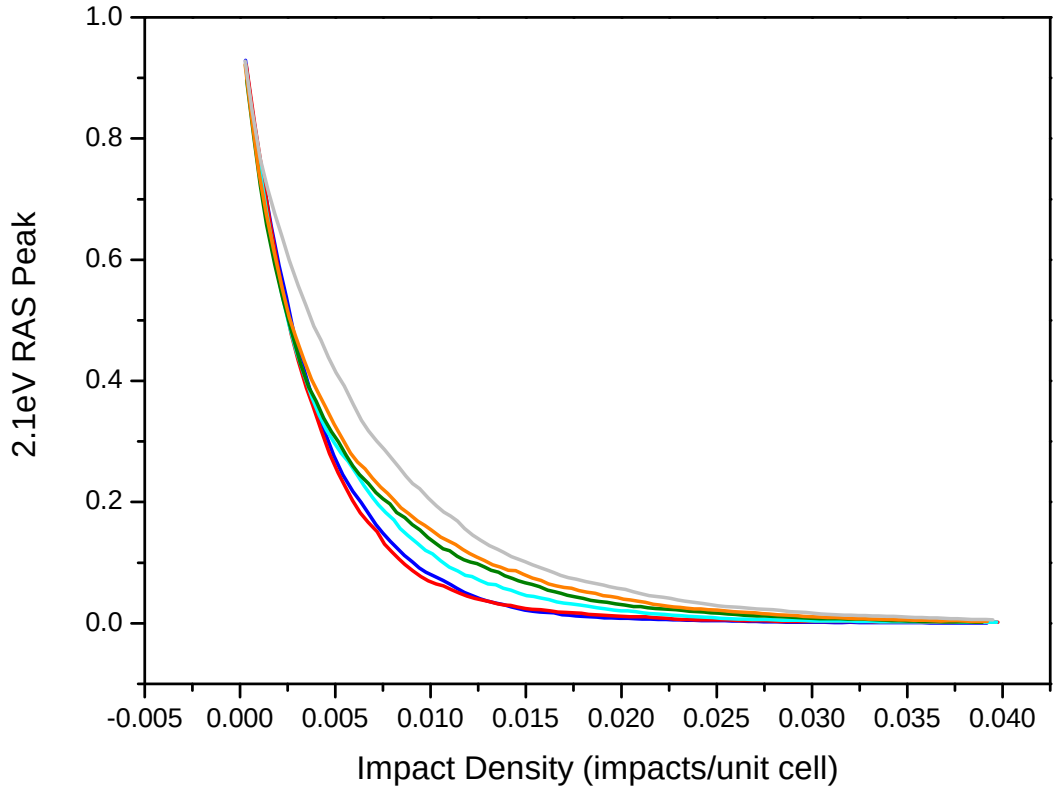

Figure 6.3 The RAS intensity vs impact density,θ, for 140K (dark blue), 150K (red), 165K (light blue), 174K (green), 180K (orange), and 200K (grey).

6.3.1 Temperature Effects on the Peak

Figure 6.3 shows the results on the RAS intensity with impact density (number of ion impacts per unit cell) for varying temperature. For higher temperatures the 2.1eV peak decreases more slowly than for low temperatures, this mimics the behaviour of experimental data seen in Figure 3.11.

Effects of temperature on the patch per impact size, Σ_I, are shown in Figure 6.4. In order to calculate Σ_I Equation 3.3, repeated here for clarity

$$I = (1 - \theta)^{\Sigma_I}, \tag{6.5}$$

where θ is the impact density and I the RAS intensity, was fitted using the least squares method for each temperature.

The result is not a linear decrease in patch per impact size as maybe expected. This shows a 'switch on' temperature of some processes around 160K, where Σ_I

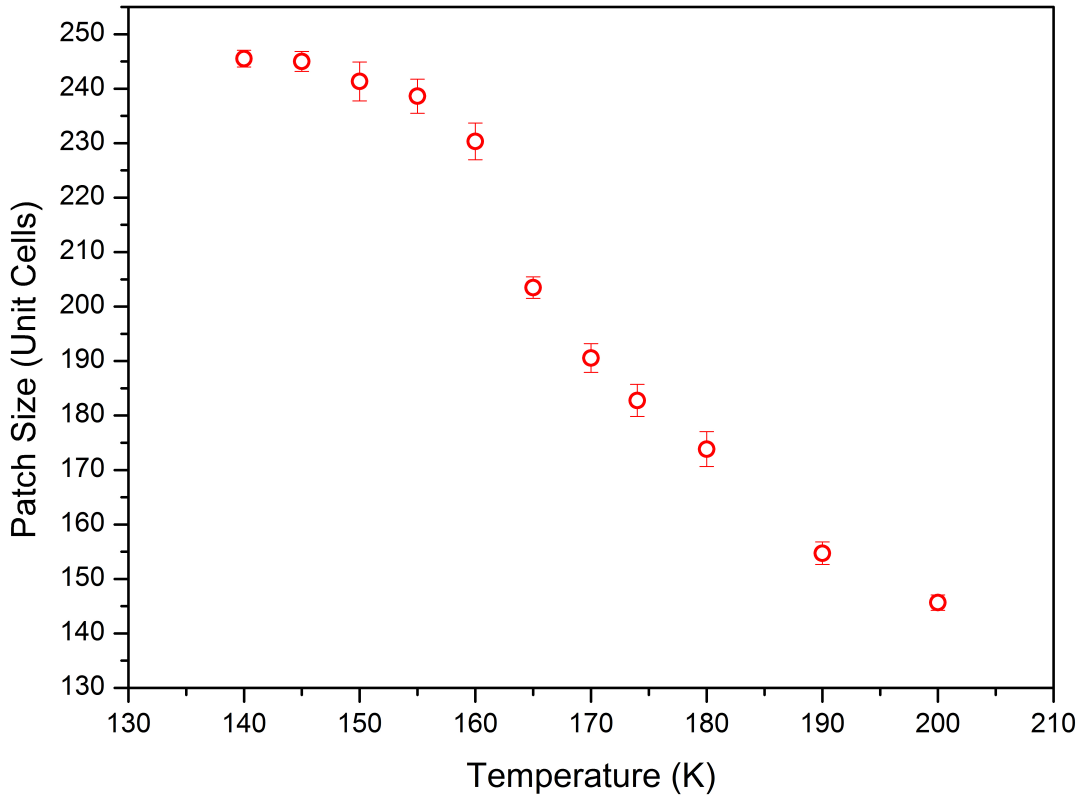

Figure 6.4 The patch per impact as a function of temperature. Errors originate from statistical variation.

decreases quickly. By inspecting Figure 4.6 the processes being access could be 5 and 9 corresponding to processes illustrated in Figure 4.5.

6.3.2 Modelling Experimental Data with the Poelsema-Comsa Fit

The Poelsema-Comsa model has been used here to fit the experimental data at various temperatures in the same way it was used above in Section 6.3.1. Figures 6.5(a), 6.5(b), 6.6(a), and 6.6(b) show the experimental data at 183K, 203K, 223K, and 243K respectively with the Poelsema-Comsa fit.

The fit was used to calculate the patch per impact, Σ_I, for each temperature using Equation 3.3 and the calculated flux in Table 6.1. Table 6.2 shows the results of this fit. There is a trend of decreasing patch size, with the exception of the 223K data.

The results are interesting as they show that the patch per impact, Σ_I, is

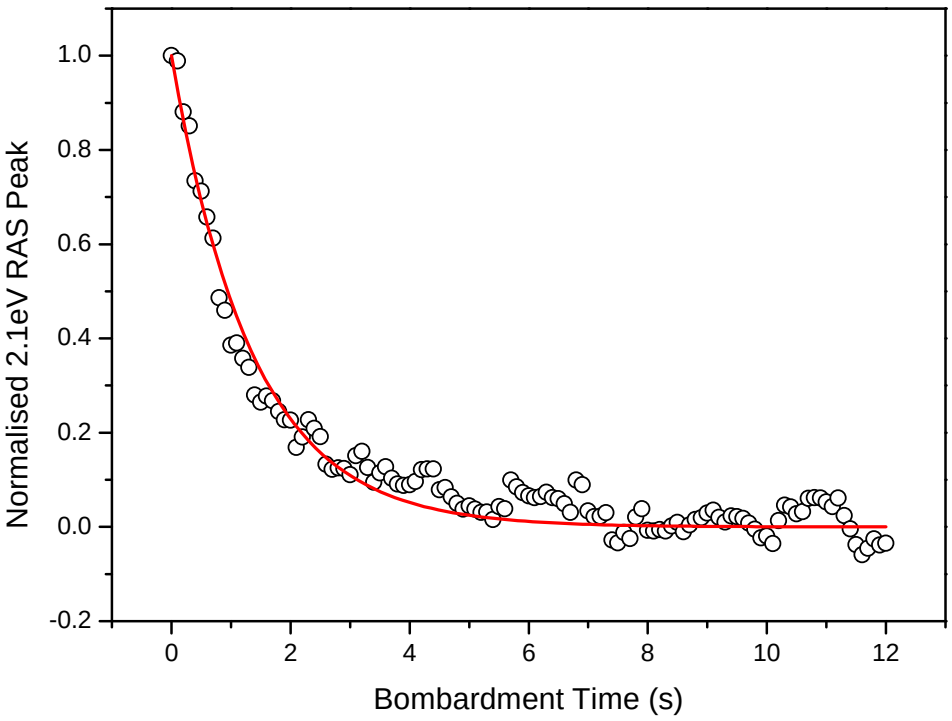

(a) 183K

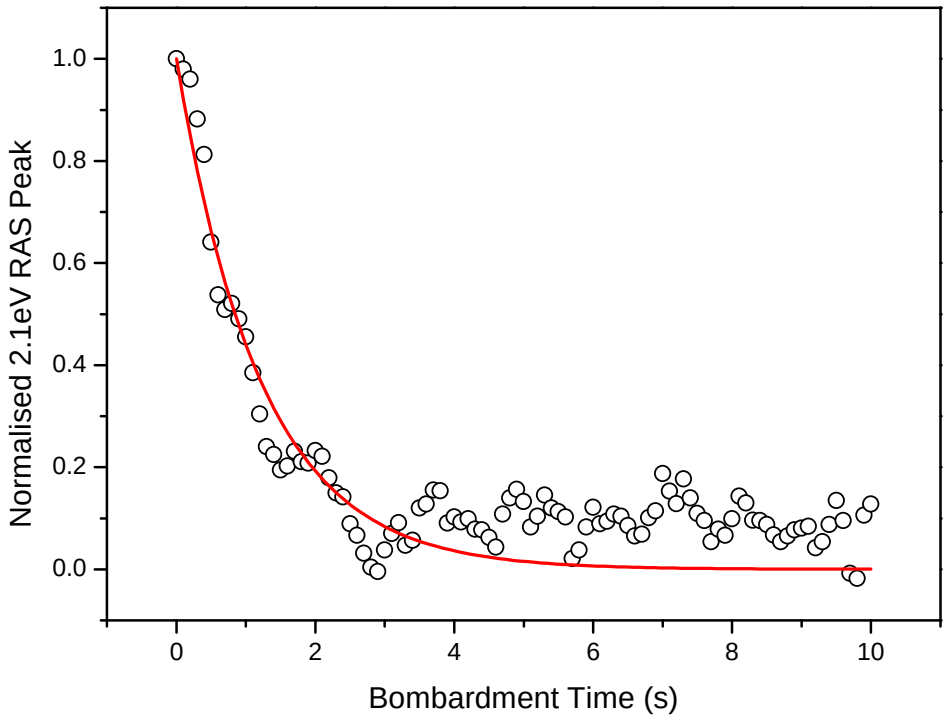

(b) 203K

Figure 6.5 The experimental data with a Poelsema-Comsa fit for 183K and 203K.

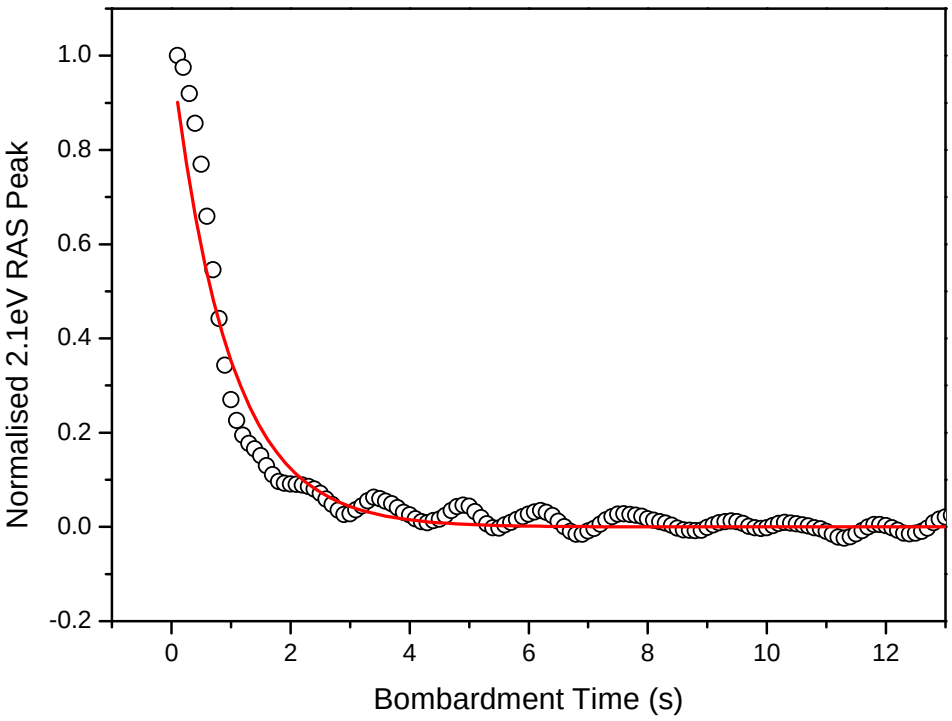

(a) 223K

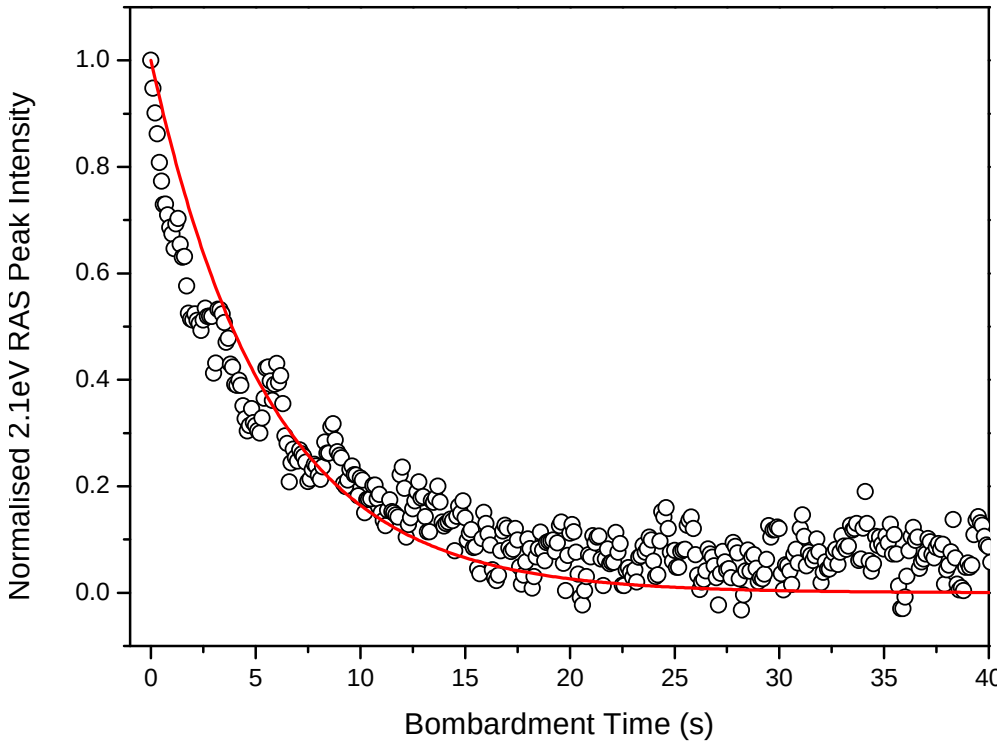

(b) 243K

Figure 6.6 The experimental data with a Poelsema-Comsa fit for 223K and 243K.

Temperature (K)	Σ_I (Unit Cells)
183	194 ± 4
203	128 ± 6
223	231 ± 6
243	112 ± 2

Table 6.2 The patch per impact calculated for experimental data at each temperature.

dependent on temperature. As the energy of the impacting ions remains constant with each data set the amount of damage initially created is solely dependent on the flux (as explained in Section 6.2.1), and therefore the initial Σ_I should be constant for all temperatures. This implies that the patch per defect is affected by the surface diffusion.

6.3.3 Modelling Experimental Data with the Kinetic Monte Carlo Simulation

The simulations were carried out on a 100×100 unit cell lattice with a step edge, using the flux calculated in Table 6.1 and a patch per defect of $\Sigma_d = 7 \times 7$ unit cells as this was the optimal size found in Section 6.2.2. The results for 183K, 203K, and 223K are shown in Figures 6.7(a), 6.7(b), and 6.8 respectively.

Above this temperature range the simulation can not reach bombardment times of order of seconds as the time step decreases with increasing temperature, as described in Section 4.2.1. As the time step decreases the computational time needed to reach longer time scales increases, as such temperatures of above 223K are currently beyond the limit of the program.

The simulation seems to fit the 183K and the 203K data well. The flux, Σ_d, and diffusion rates seem to have been estimated correctly. This also indicates there are no key diffusion processes missing from the model, where the processes chosen are shown in Figure 4.5.

The 223K data has a y-axis change as the experimental 2.1eV RAS data did not fall to zero. This is due the RAS spectra changing due to temperature effects, described in Section 3.2.2, where the surface states shift with temperature. As such, the RAS intensity for the 223K data was normalised to the 183K data (so that the RAS intensity falls to the same value as the 183K data), and in doing so

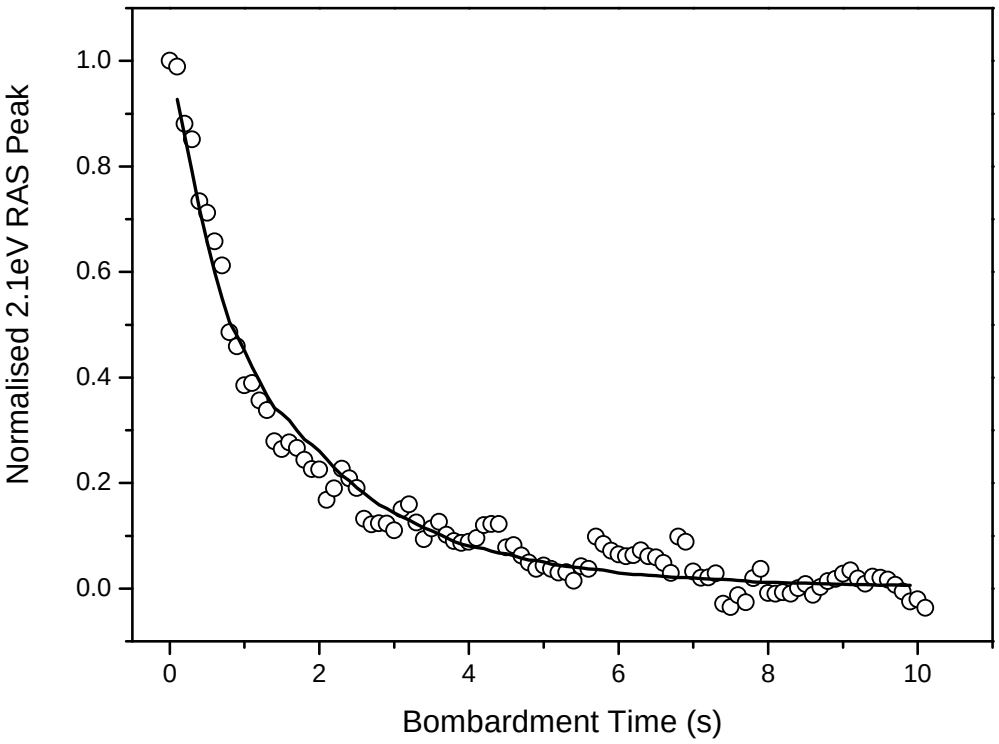

(a) 183K

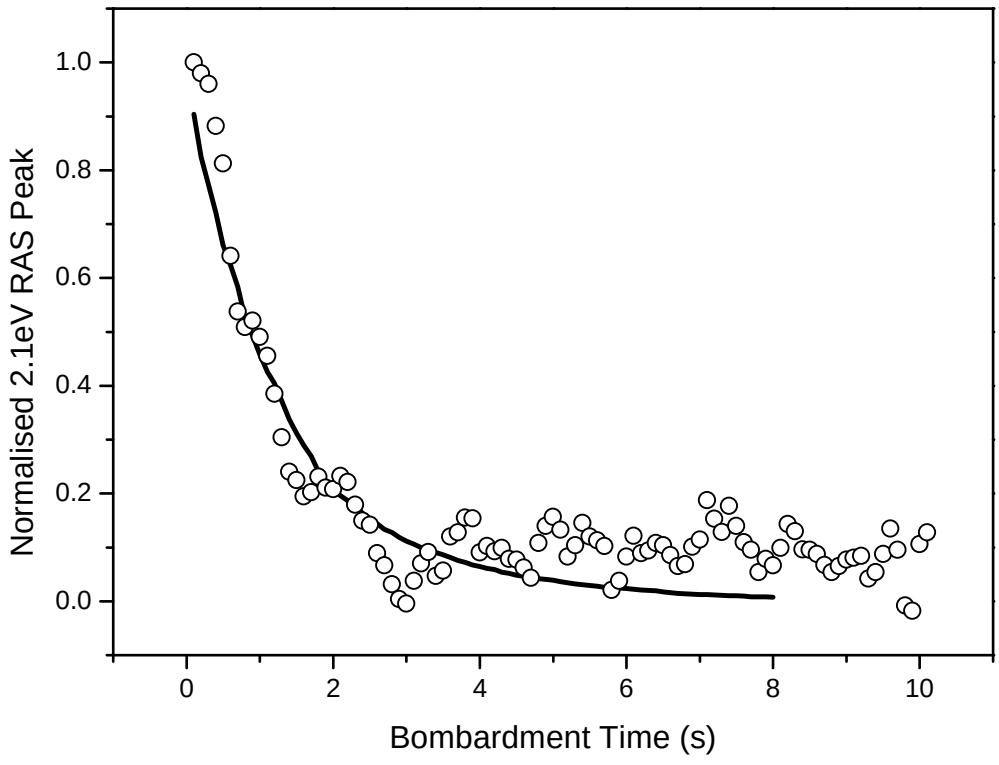

(b) 203K

Figure 6.7 The simulation and experimental data for the ion bombarded surface at 183K and 203K.

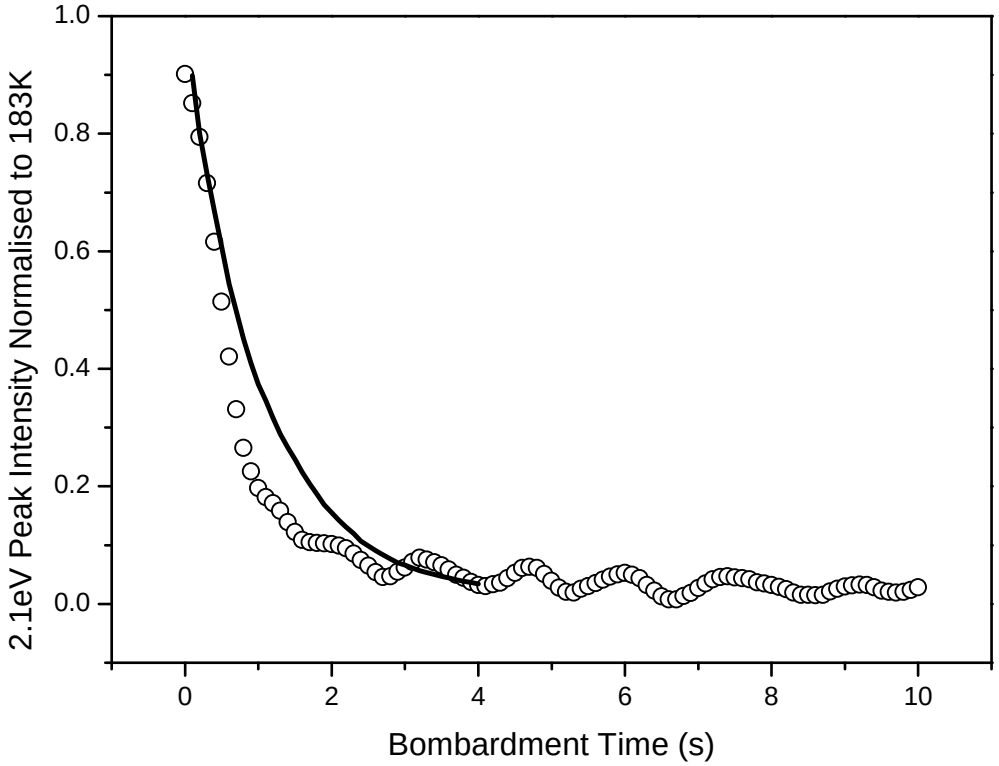

Figure 6.8 The simulation and experimental data for the ion bombarded surface at 223K.

the simulation data is now able to more accurately model the higher temperature data.

After re-normalisation of the experimental data the simulation does not predict the 223K data with the same accuracy as the lower temperature experimental data. The residuals at 223K are shown in Figure 6.10 and are the largest for simulated data. This could be due to a miscalculation of the flux, an inaccuracy in the model which is only observed at higher temperatures, or an experimental anomaly. An inaccuracy in the model could arise from an overestimation of the amount of diffusion on the surface at this temperature.

6.3.4 Analysing Residuals

Here the residuals of the Polesema-Comsa fit to the simulation and experimental data have been analysed. Doing this allows us to evaluate whether the model and the simulation are accurately predicting experimental data.

Figures 6.9(a), 6.9(b), and 6.10 show residuals of the experimental data and the

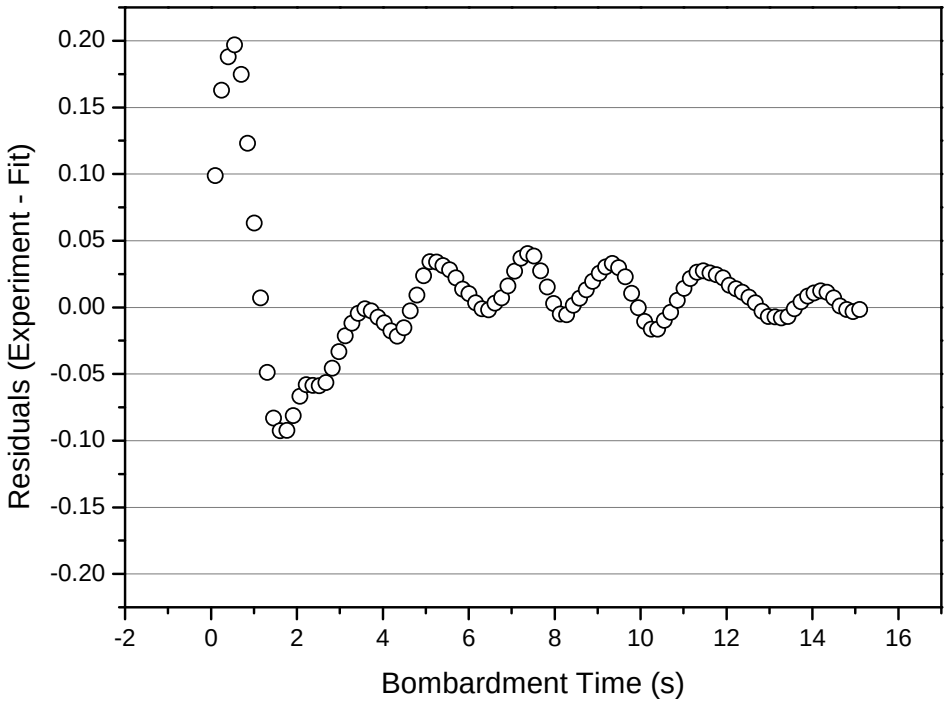

(a) Residuals of the experiment−the Poelsema-Comsa fit at 223K.

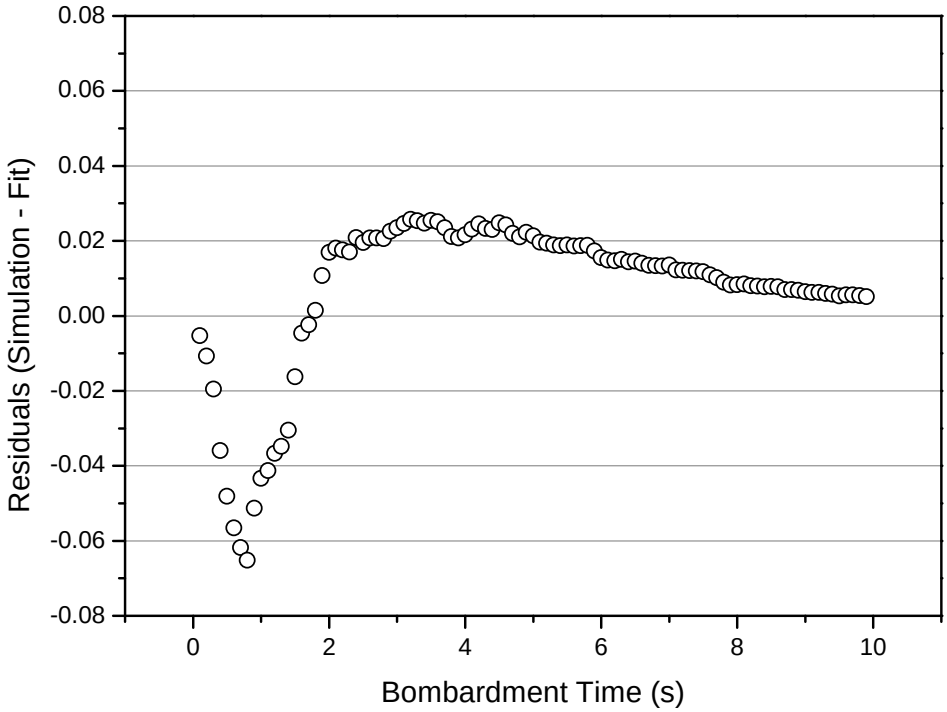

(b) Residuals of the the simulation−the Poelsema-Comsa fit at 183K.

Figure 6.9 Graphs showing the residuals of the experiment and the simulation−the Poelsema-Comsa fit.

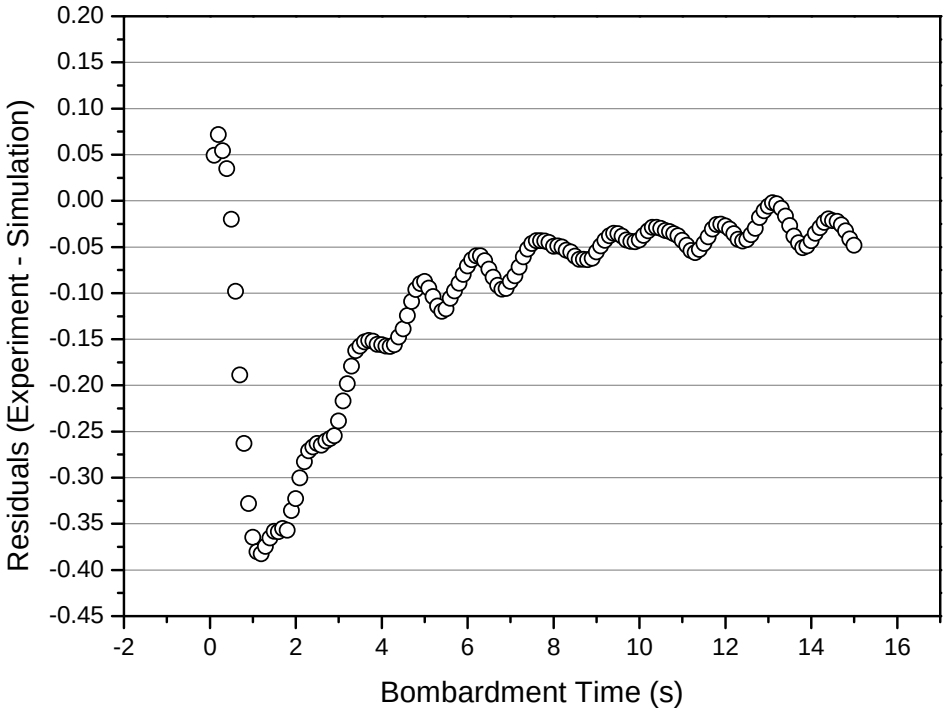

Figure 6.10 Residuals of the the simulation−experiment at 223K.

fit, the simulation data and the fit, and the experimental data and the simulation data respectively. These residuals were chosen as they show the largest trend; residuals for all the data analysed are contained within Appendix A. The periodic feature contained in some of the residuals come from experimental data rather than simulation.

As can be seen from the residuals there is a trend present, where each one is qualitatively similar. This hints at a missing parameter in the Poelsema-Comsa model.

6.4 Analysing the Patch per Impact as a function of Bombardment Time

In Section 6.3.4 the residuals of the Poelsema-Comsa model were analysed with respect to the simulation and the experimental data. The data shows a clear trend leading to, as discussed, the conclusion that the Poelsema-Comsa model is missing a parameter. This is possibly temperature dependent, and leads us to consider diffusion to be the possible missing parameter.

The Poelsema-Comsa model (described in Section 3.3) uses Equation 3.3, repeated here for clarity

$$I = (1 - \theta)^{\Sigma_I}\,, \tag{6.6}$$

where I is the RAS 2.1eV peak intensity, θ is the impact density, and Σ_I is the patch per ion impact in unit cells to model the RAS data. In this model the patch per impact is constant as each impact creates a 'RAS patch' which does not change. This assumption should hold true for the 0K case where no diffusion occurs on the surface such that all defects are immobile. However, at non zero temperatures the total patch per impact may change over time as the defects recombine and create clusters which reduces damage, as explained in Section 3.3.

To analyse the patch per impact over bombardment time Equation 6.6 can be rearranged to give

$$\Sigma_I = \frac{\ln I}{\ln (1 - \theta)}\,, \tag{6.7}$$

such that the patch per impact can be plotted as a function of bombardment time, t, as $\theta = ft$, where f is the flux (ions/unit cell/second).

6.4.1 Experimental Results

As discussed above, the Poelsema-Comsa equation assumes there is no surface diffusion, and in this case the patch per impact is constant. Using Equation 6.7 the patch per impact can be plotted against bombardment time for experimental data, the results of which are shown in Figure 6.11 for various temperatures.

The results show a decreasing trend in the patch per impact for all temperature ranges in the experimental data. Unexplained though, is a rise in the patch per impact in the first few seconds of bombardment before the decrease. This could be due to variations in the flux due to the ion gun having not stabilised as described in Section 2.2.4.

Temperatures of 183K-223K qualitatively behave similarly, each taking a few seconds to reach their maximum patch per impact and then decreasing at approximately the same rate. The higher temperature data (243K-283K) also behave similarly but quite differently to the lower temperature data. In this regime the patch per impact increases to a maximum within the first seconds of bombardment, and then decreases more rapidly than the lower temperature data. This indicates a change in the surface kinetics between temperatures of 223K and

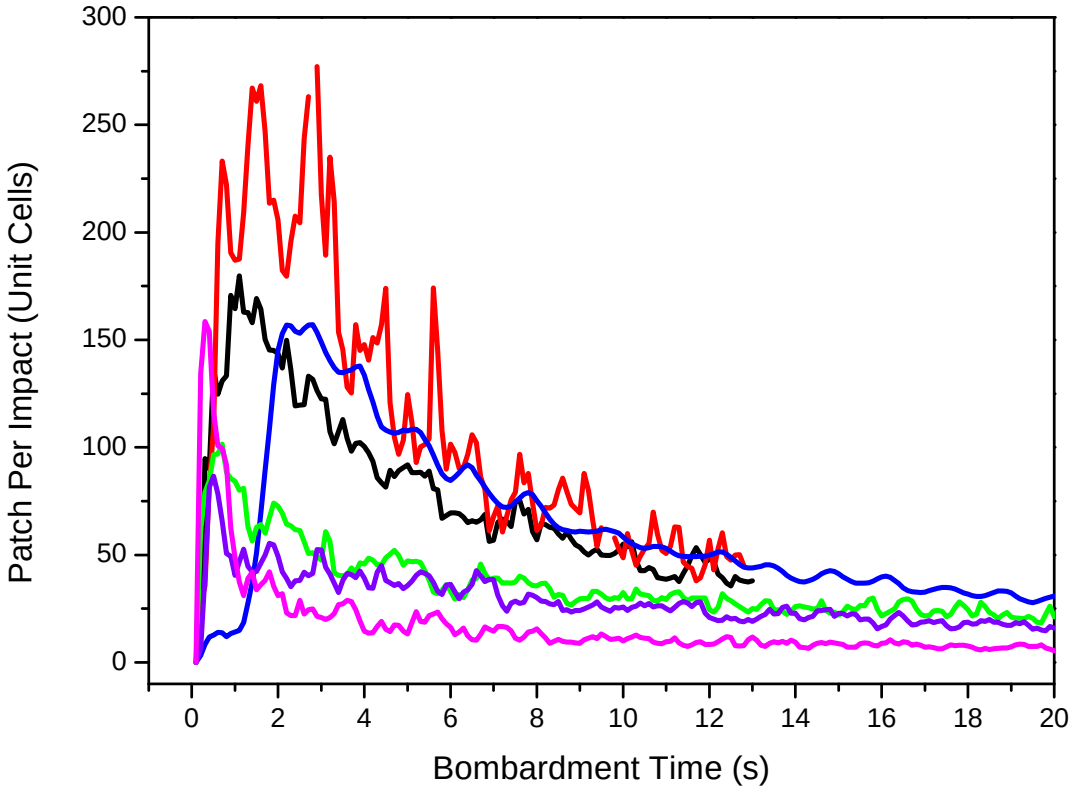

Figure 6.11 The patch per impact as a function of bombardment time for experimental data at 183K (black), 203K (red), 223K (blue), 243K (green), 263K (purple), and 283K (pink).

243K. This change could be attributed to the 'switching on' of a process in this temperature region. Analysing the data this way shows us that Σ_I is dependent on temperature, T, and time, t, *i.e.*

$$\Sigma_I = f(\Sigma_d, T, t)\,. \tag{6.8}$$

6.4.2 Simulation Results

The patch per impact was also analysed for the simulation data, with results shown in Figure 6.12. The simulation results show a similar decline in the patch per impact to experimental results. The first seconds of bombardment also replicate the behaviour seen in experimental data.

Also shown in Figure 6.12 are results for bombarding the surface at 0K. As can be seen from the graph the patch per impact is relatively stable which implies a constant patch per impact. This is expected as there is no diffusion occurring on

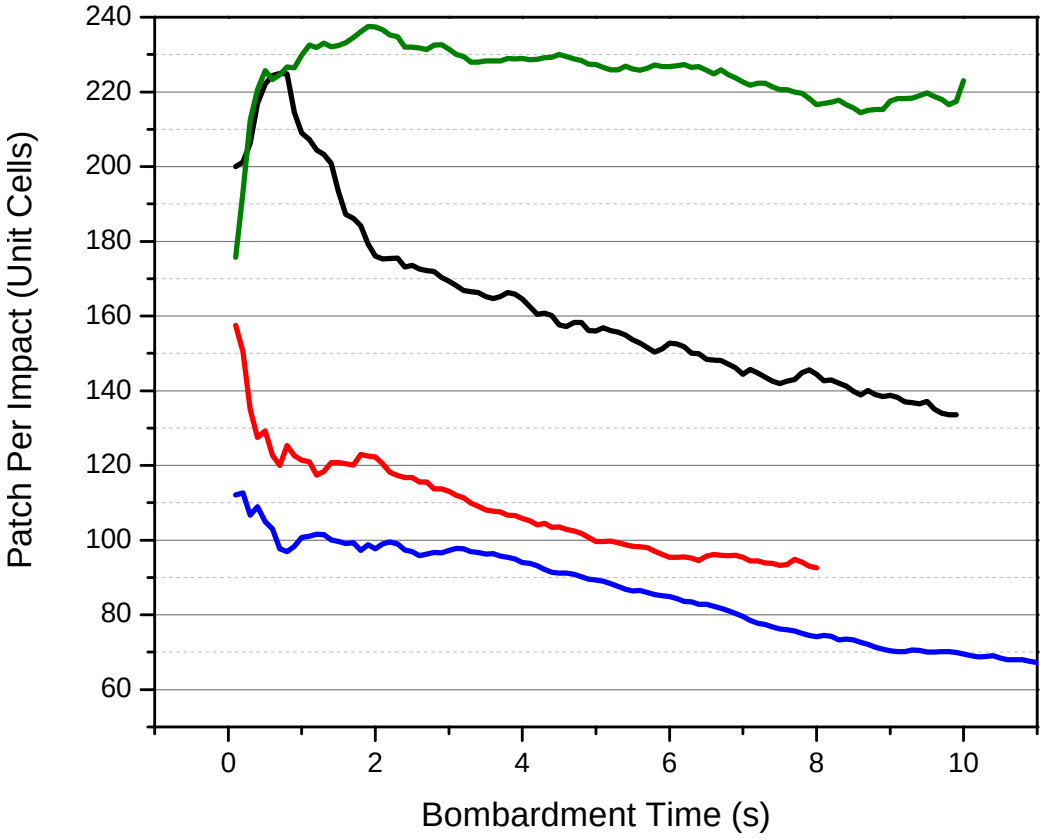

Figure 6.12 The patch per impact as a function of bombardment time for simulation data at 0K (green), 183K (black), 203K (red), and 223K (blue).

the surface. The noise is due to the random nature of the ion flux, where at any time there is a probability that an ion impact will occur, but the actual number will vary over time. The 0K data also shows a large increase in the first seconds of bombardment, which means this is not an effect of diffusion. It could be due to a sensitivity of the ion flux, where at the start of bombardment not many ions have impacted the surface such that the average flux is unstable.

6.5 Discussion

The Cu(110) surface has been successfully simulated at temperatures of 183K and 203K. This indicates that the flux, and patch per defect size of $\Sigma_d = 7 \times 7$ unit cells have been correctly calculated using the experimental data. It also indicates that the key diffusion processes have been successfully identified and their corresponding energy barriers are correct, and that in order to model the

RAS intensity at finite temperatures diffusion of defects need to be considered which improves on previous studies [54].

It seems that at the higher temperature of 223K the simulation does not predict the normalised peak quite as well as the lower temperature data. This could be due to an inaccuracy in the simulation, possibly too much diffusion such that the diffusivity constant, D_0, is too high.

After analysis of residuals it was concluded that the Poelsema-Comsa model is missing a parameter which is assumed to be diffusion. Diffusion plays a role in decreasing the patch per impact size over time. This has been shown to be the case using experimental data of the 2.1eV peak such that $\Sigma_I = f(\Sigma_d, T, t)$. This method for analysing the patch per impact over time seems non-trivial with features in the data still unexplained, but with more investigation may provide a novel way of monitoring surface diffusion using experimental RAS data alone.

Chapter 7

Investigating the Surface Nanostructure after Ion Damage

7.1 Introduction

In this chapter the nanostructure of the Cu(110) ion bombarded surface is analysed and modelled. As explained in Section 3.4.2 current studies do not replicate the nanostructure of the surface well, this chapter explores whether including diffusion on the minute scale in the model improves on the current MD results [14].

STM images of the surface have first been re-analysed and a new result for the surface structure calculated. This is then compared to KMC simulation results of the surface, which are shown to improve on MD simulation results. The evolution of adatom clusters are also analysed giving a unique insight to the formation of these clusters.

7.2 STM Cluster Analysis

As discussed in Section 3.4.2, in the analysis of STM images in a study by Lane *et al.* [14] only defects which were part of craters which were obvious impact sites upon inspection were counted, this may have biased larger impact sites and not included single adatoms. It can be reasoned that, with higher surface mobility,

single adatoms may have diffused away from these crater sites and therefore may not have been included in the results.

7.2.1 Image Analysis

A new way of assessing the surface nanostructure has been devised using the image editing software ImageJ [80]. Figure 7.1 shows an image of the Cu(110) surface after ion bombardment of 2 seconds at a rate of 0.0014 ions/unit cell/second.

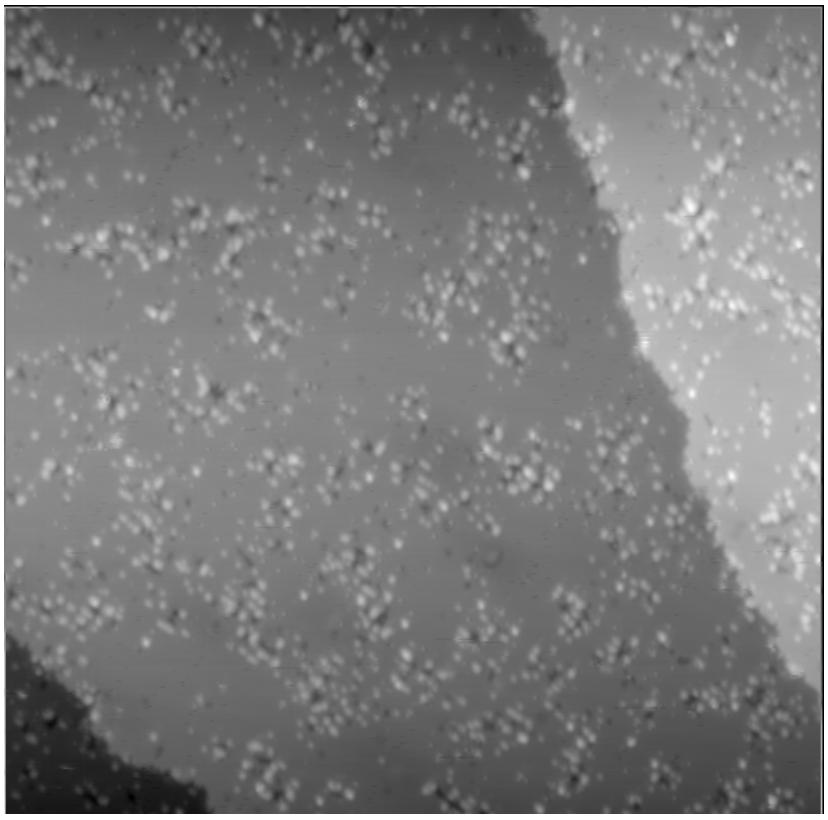

Figure 7.1 STM image of the 80×80 nm^2 Cu(110) surface after 2 seconds of ion bombardment [54].

Using the software the background was subtracted and the contrast and brightness enhanced such that only the adatoms are visible on the surface as seen in Figure 7.2(a).

Thresholding[1] was then used to create a binary image. The result of this is shown in Figure 7.2(b). The software then allows for particle analysis of this

[1]Where pixels above a certain number on the grey scale are converted into a white pixel, and below are converted into black.

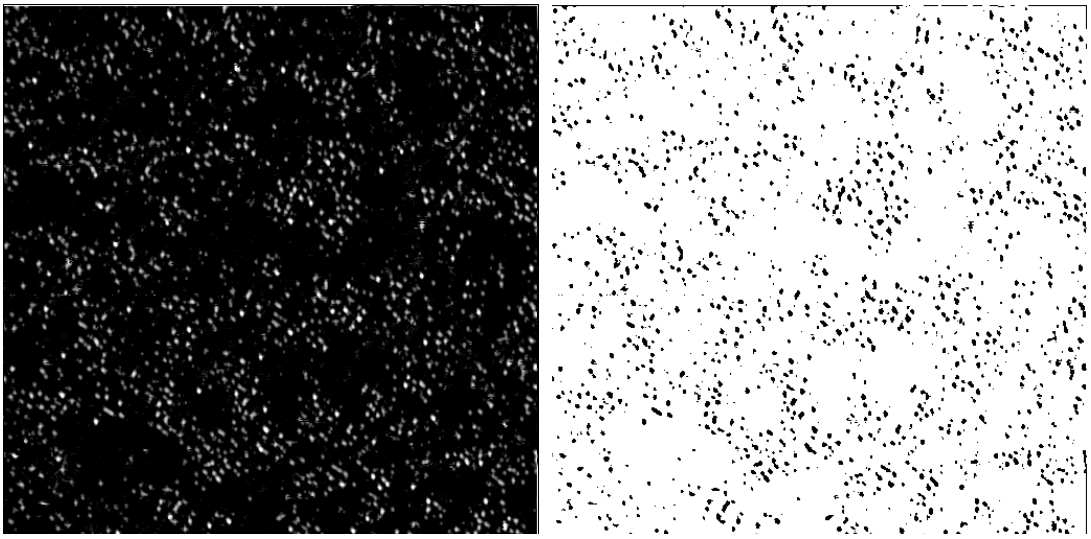

(a) STM image of the Cu(110) surface after 2 seconds of ion bombardment with the background subtracted.

(b) STM image of the Cu(110) surface after 2 seconds of ion bombardment with the background subtracted and thresholded.

Figure 7.2 STM images of the Cu(110) after image analysis using ImageJ.

image where each cluster is allocated a number, and the associated area of the cluster in pixels.

Knowing that the size of the image corresponds to an area of 80nm×80nm, each cluster area can be converted into nm^2 using the size in pixels. STM tip convolution (a result of the STM tip having a non zero thickness) is accounted for by subtracting 1Å from the radius of each cluster. The number of adatoms which make up a cluster size can be calculated using this information where an adatom was assumed to be the size of one unit cell.

The number of impacts on the surface can be calculated using the flux (0.0014±0.0003 ions/unit cell/second), the bombardment time (2 seconds), and the area being analysed (6400nm^2), which equates to 195±40 impacts over the whole area. The cluster sizes are then rounded to whole numbers and binned according to their size, this gives the total number of each cluster size on the whole surface being analysed. This is then divided by the total number of ion impacts on the surface to give the average number of each cluster size per impact.

Figure 7.3 shows the results for the different levels of thresholding on the surface. The thresholded values correspond to the grey scale values which are are the cut off values for the binary image. As can be seen the lower thresholded value

of 46 produces a noisy profile with many larger clusters being counted and less single adatoms being counted on the surface. This is due to the grey scale value being too small such that small clusters are being counted as larger clusters due to surface blurring (due to STM tip convolution), and clusters which are close together are being counted as one large cluster as they merge together.

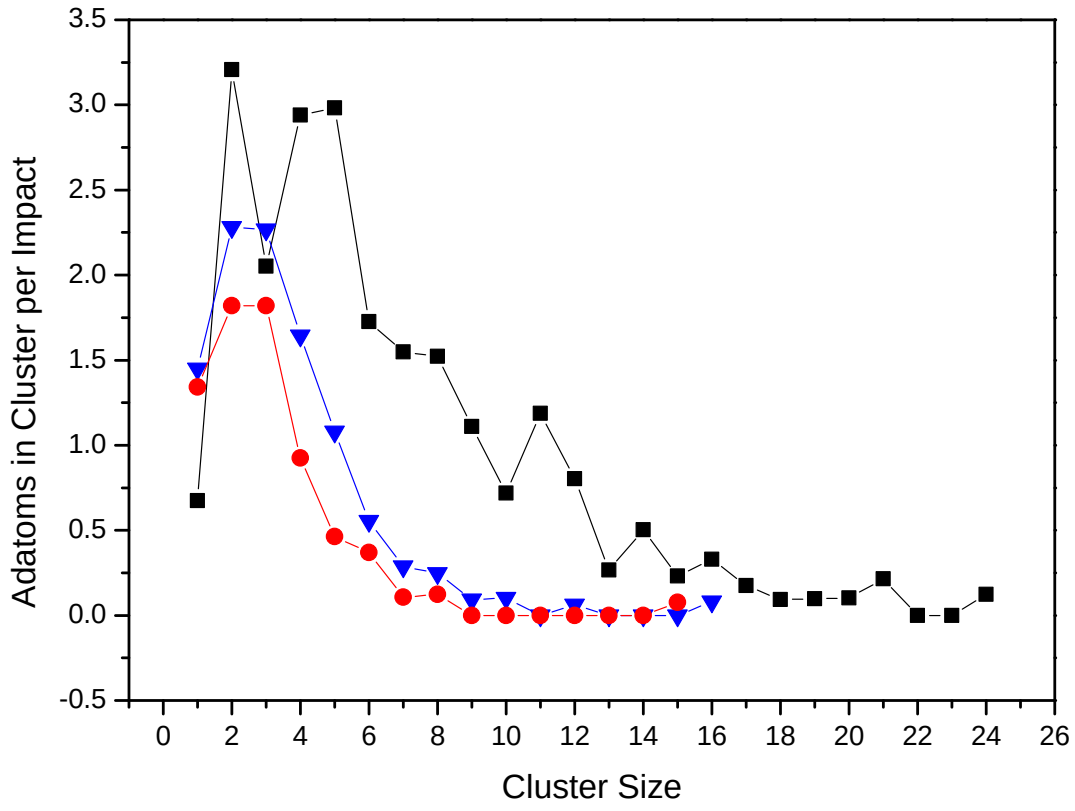

Figure 7.3 Cluster profile for threshold values of 46 (black squares), 80 (blue triangles), and 96 (red circles).

The higher thresholds suffer the opposite problem where smaller adatoms may not be included as their grey scale values are under the threshold value, and clusters maybe underestimated in size. However, larger clusters are being differentiated from clusters close by. The thresholded value of 80 was chosen as single adatoms are still being observed on the surface and the larger clusters are not merging into one and are being counted, with their size estimated as being approximately correct.

7.2.2 New Cluster Analysis Results

The result of the new STM analysis is shown in Figure 7.4 along with STM analysis by Lane *et al.* [14]. Applied to the analysis was a cut off point for single adatoms of over size 0.7, where only clusters with over 0.7 adatoms were counted. This is because the image contains some noise and any cluster of size under 0.7 adatoms is more likely noise than a surface defect. The error bars on the new analysis are due to uncertainties in flux.

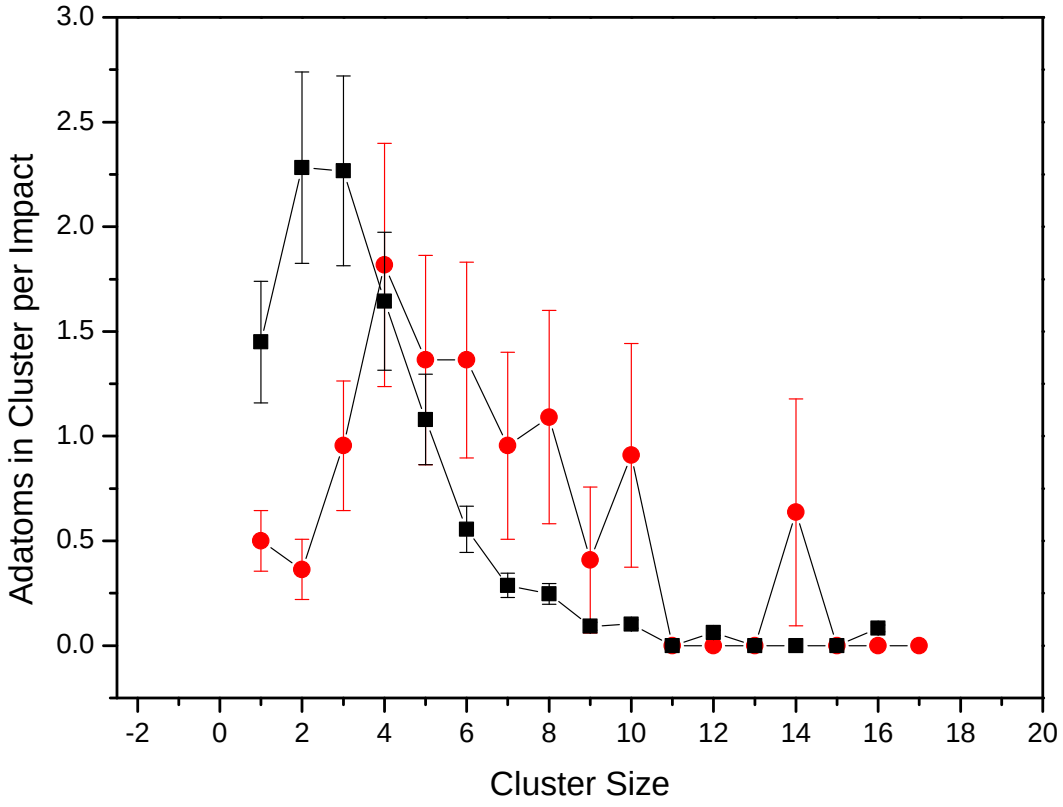

Figure 7.4 Cluster analysis of the STM image with the original data (red circles) [14] and data from the new analysis (black squares).

As can be seen from the graph the cluster profiles are qualitatively different. The new analysis suggests more single adatoms on the surface, with a peak in clusters of 3 to 4 adatoms. There is then a fast decline in the number of larger adatom clusters. This is more consistent with what is seen on the surface in Figure 7.1 where on close inspection small adatom clusters can be seen which are not in close proximity to an obvious impact site. The new analysis also predicts fewer large adatom clusters than the original analysis.

This new analysis of the STM images will be used as experimental results in the following sections. This is because it takes account of the whole surface, without bias to large impact sites caused by identifying impact sites by eye.

7.3 Simulation Results

As explained in Section 3.4.2 previous surface simulations do not replicate the atomic structure of the surface after ion bombardment and 30 minutes of diffusion well. By considering surface diffusion on the scale of minutes this has been improved.

Figure 7.5 shows the KMC simulated surface after (a) 2 seconds of ion bombardment at 0.0014 ions/unit cell/second and (b) the same surface after 30 minutes of diffusion at 144K. There is a clear difference in the surface nanostructure upon inspection of the two images, which implies diffusion plays a large role in the shaping of the surface under these conditions. This section further explores the nanostructure of the surface after long diffusion periods using quantitative measurements of the surface clustering.

7.3.1 A Comparison with STM and MD Results

To improve on previous results [14] the KMC simulation (described in Chapter 4) has been used to incorporate diffusion into the model of the ion bombarded surface deduced from MD simulations (which we believe give an accurate representation of the bombardment process on the picosecond time scale). The KMC simulation bombarded a 100×100 unit cell lattice (with a step edge) for 2 seconds at a flux of 0.0014 ions/unit cell/second in order to recreate the experimental conditions. The surface was then diffused at 144K for 30 minutes, after which the number of clusters and the size of each was calculated using the algorithm described in Section 4.4.2.

Results of the cluster analysis from the KMC simulation are shown in Figure 7.6 along with MD [14] and the new STM surface analysis. The results show that the KMC model can qualitatively reproduce the surface better than MD alone.

Although an improvement on MD results as the biggest discrepancy is removed (the excess of single adatoms in the MD results), the KMC model underestimates

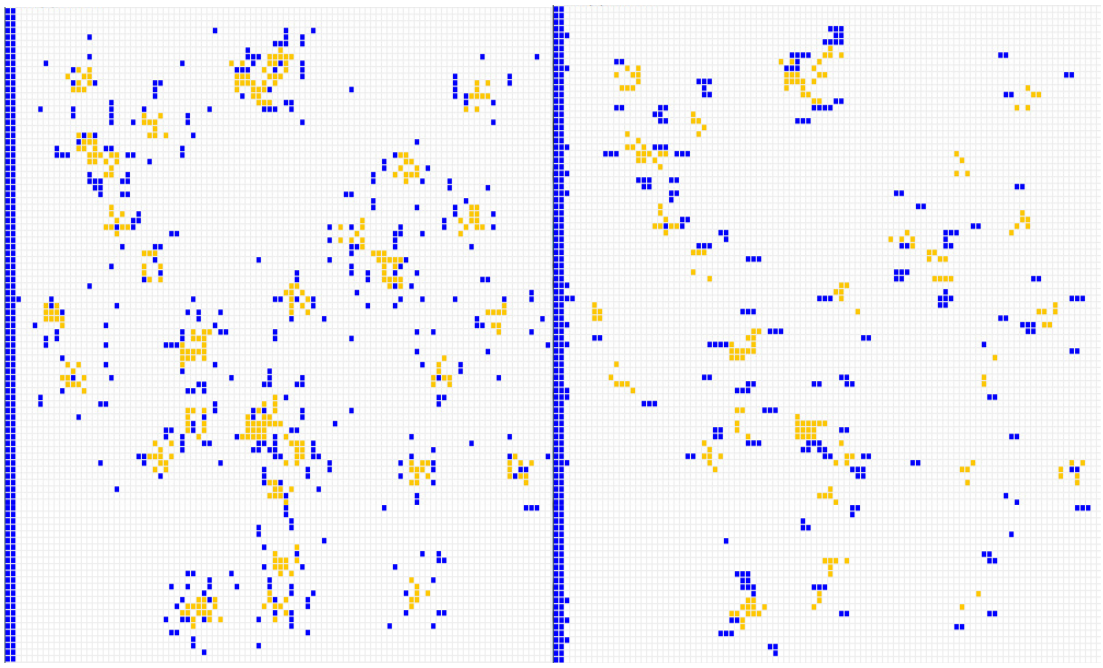

(a) The simulated surface after 2 seconds of ion bombardment.

(b) The simulated ion bombarded surface after 30 minutes of diffusion.

Figure 7.5 Results of the program showing the simulated lattice 2 seconds after ion bombardment and the same lattice after half an hour of diffusion with adatoms shown as blue and vacancies as orange. A step edge is created with a 2 layerd line of adatoms.

the number of smaller adatom clusters and larger clusters remaining on the surface after the total diffusion time. This could be due to a diffusion parameter being too high such that all the single adatoms have either recombined with a vacancy or step, or have created a cluster with other adatoms.

Figure 7.7 shows the residuals of the STM data compared to KMC and MD simulations. As can be seen from the graph the KMC predicts the surface structure more accurately for lower sized cluster than MD alone, but is underestimating single adatom clusters.

7.3.2 Cluster Evolution

Using the cluster counting algorithm described in Section 4.4.2 the number of adatom clusters on the surface has been monitored after the surface has been ion damaged as a function of diffusion time. The surface was bombarded for 2 seconds at 0.0014 ions/unit cell/second at 144K. The total number of adatoms

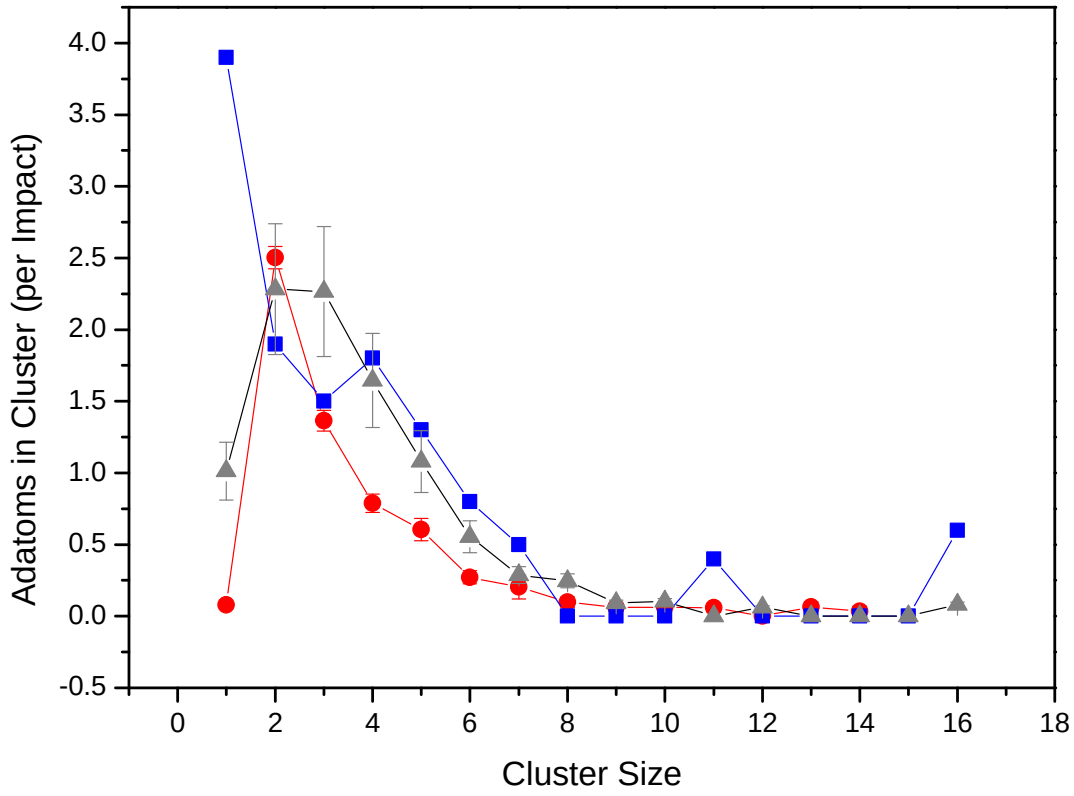

Figure 7.6 Frequency of adatoms which make up different cluster sizes per defect for MD calculations (blue squares) [14], STM imaging results using the new imaging technique (grey triangles), and KMC results (red circles).

that make clusters of a given size was recorded at intervals such that the surface was left to diffuse for 1 second after ion bombardment, up to half an hour. Results of these simulations are shown in Figure 7.8.

The simulation results show the single number of adatom clusters decrease logarithmically (note the logarithmic scale of the graph) which is previously predicted by Lane *et al.* [22]. This shows that the number of single adatoms on the surface decrease quickly in the first few seconds once the diffusion process has begun.

The number of adatoms which make it to a step edge increases logarithmically with diffusion time, which is expected as the single adatoms migrate over the surface to join the step edge. The number of of dimers on the surface seems to decrease with increasing diffusion time. This is probably due to single adatoms joining the dimers to make trimers such that the number of smaller clusters decrease as the larger clusters increase. This is seen in the increase with time of the number of clusters of size ≥ 5 adatoms.

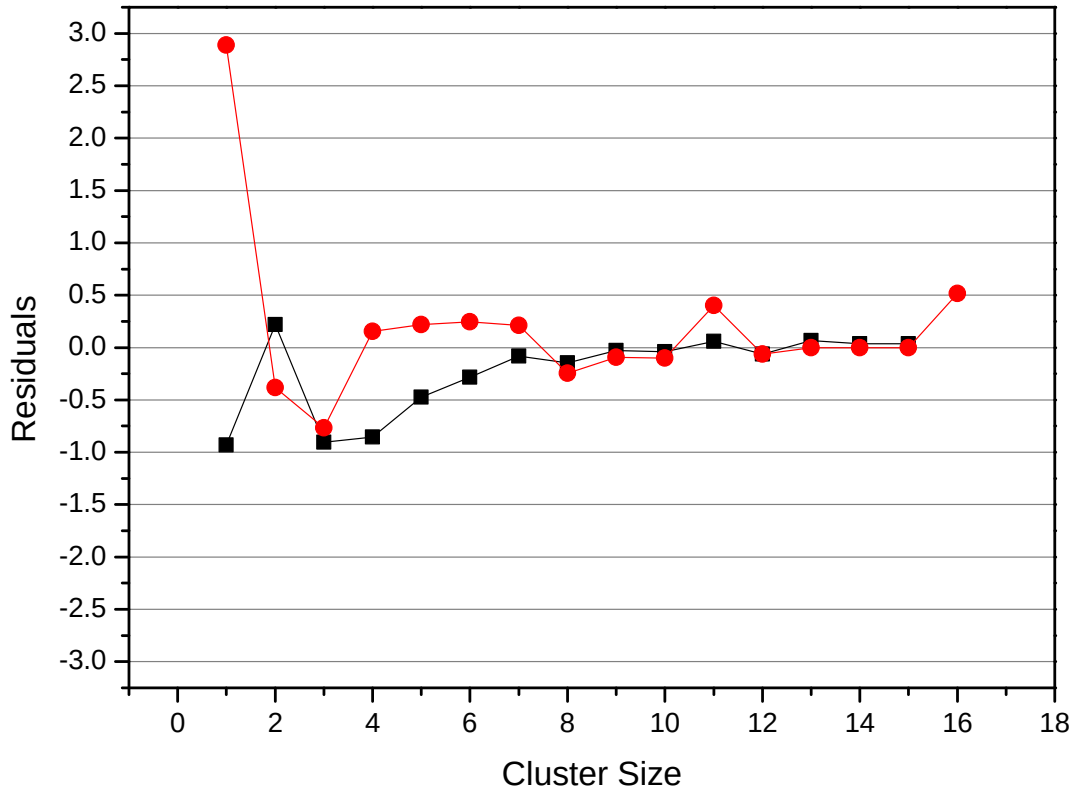

Figure 7.7 Residuals of the MD simulation and the new STM cluster analysis (red circles), the KMC simulation and the new STM cluster analysis (black squares).

Clusters of 3 and 4 adatoms seem to increase in the first $\approx$ 10 seconds before decreasing. This is possibly due to single adatoms joining to make larger clusters, where this reaches a maximum at $\approx$ 10 seconds after which many turn into larger clusters which is seen in the increase in the 5 adatoms and above clusters.

This time scale of cluster evolution is interesting as the surface structure seems to change quickly in approximately the first 10 seconds, and then on a slower time scale after this initial diffusion. This has implications when taking experimental measurements of the surface structure, such as RAS data, after damaging the surface as it seems measurements need to be taken quickly in order to obtain a true picture of the surface immediately after ion bombardment.

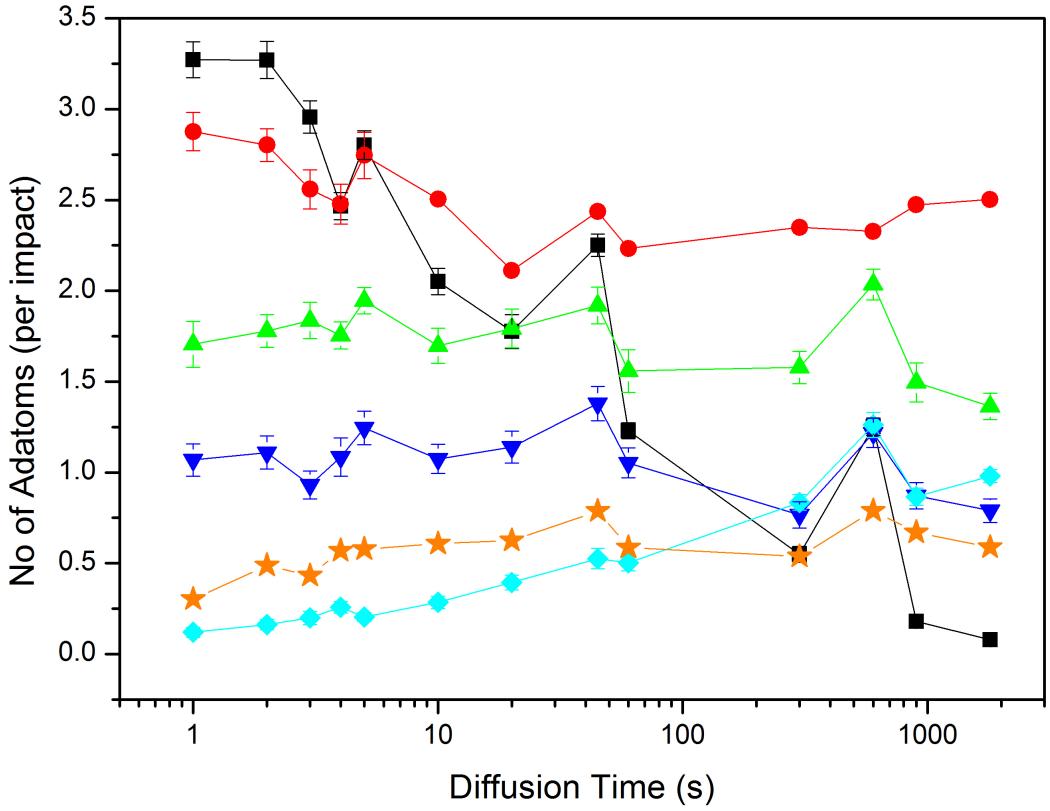

Figure 7.8 Frequency of adatoms which make up different cluster sizes per defect as a function of time on a log scale, for cluster sizes of 1 (black square), 2 (red circle), 3 (green triangle), 4 (blue upside down triangle), above 5 adatoms (orange star), and adatoms which have joined the step edge (light blue diamond) are shown.

7.4 Discussion

The nanostructuring of the ion bombarded Cu(110) surface has been analysed using STM images and simulations. A new technique for image analysis has been described along with cluster analysis results. This new technique was deemed more suitable as it considered the whole imaged surface, without bias to obvious impact sites.

The surface was simulated in order to reproduce STM experimental results with the new analysis. By analysing residuals the KMC simulation was shown to be more effective in modelling the surface than MD alone. This is because MD results simulate up to nanoseconds, but diffusion mechanisms that shape the structure of the surface take place on the seconds scale.

It was concluded that a surface diffusion parameter was too high at this

temperature as after 30 minutes of diffusion the simulated surface underestimated the amount of single adatoms and small clusters than the experimental results show. This could be due to the diffusivity constant, D_0, being too high.

The number of adatoms which make up different cluster sizes was recorded for different diffusion times. The surface was seen to change quickly in the first ≈ 10 seconds and then more gradually for the remainder of the 30 minutes of diffusion. This implies the nanostructure of the surface changes quickly, with other processes occurring more gradually after the first ≈ 10 seconds.

Chapter 8

Modelling Surface State Recovery

8.1 Introduction

Once the surface has undergone ion bombardment at temperatures above 0K the annealing process begins. This chapter analyses this process by using experimental and simulation data of the Cu(110) RAS intensity after the surface has undergone ion bombardment.

In experimental results, collected by Lane [81], the Cu(110) surface was ion bombarded for a few seconds at a number of temperatures, the ion gun was then switched off and the surface monitored for $\approx$ 30 minutes using RAS. The RAS intensity was measured and seen to recover over time.

KMC simulations have been performed to mimic this experimental data, with the surface bombarded for 2 seconds and then left to diffuse for 30 minutes while the Poelsema-Comsa method was used to calculate the RAS intensity.

Presented here is an analysis of the the peak recovery after ion bombardment and a calculation for the diffusion constant, D_0, calculated by comparing simulation and experimental results.

8.2 Experimental Data

Experimental RAS data of the annealing process, obtained from Lane [81], has been analysed. In these experiments the Cu(110) surface was bombarded for 10 seconds at 0.0014 ions/unit cell/second for a range of temperatures at which time the ion gun was switched off. The surface was then maintained at the temperature at which it was bombarded while the RAS intensity was monitored. An example is illustrated in Figure 8.1 which shows the experimental data at 243K. The peak recovery is clearly visible in the data with the signal to noise ratio is relatively low. The recovery of the peak was calculated for different experimental temperatures,

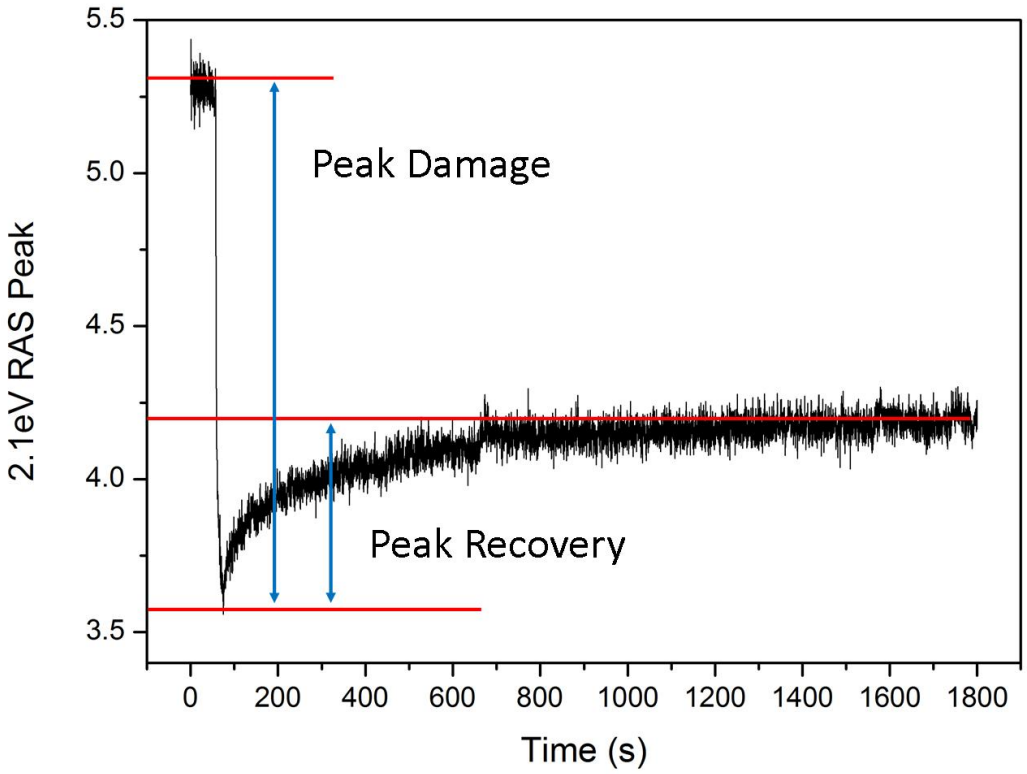

Figure 8.1 Peak recovery for experimental RAS data at 243K [81] showing the total peak damage by ion bombardment, and the peak recovery after ion bombardment.

results are presented in Figure 8.2 as a percentage of the original signal. The peak recovery was recorded as a percentage of the total peak damage indicated in Figure 8.1.

The errors on the values originate from the noise in the signal which can be seen in Figure 8.3, where the normalised experimental RAS intensity is plotted with

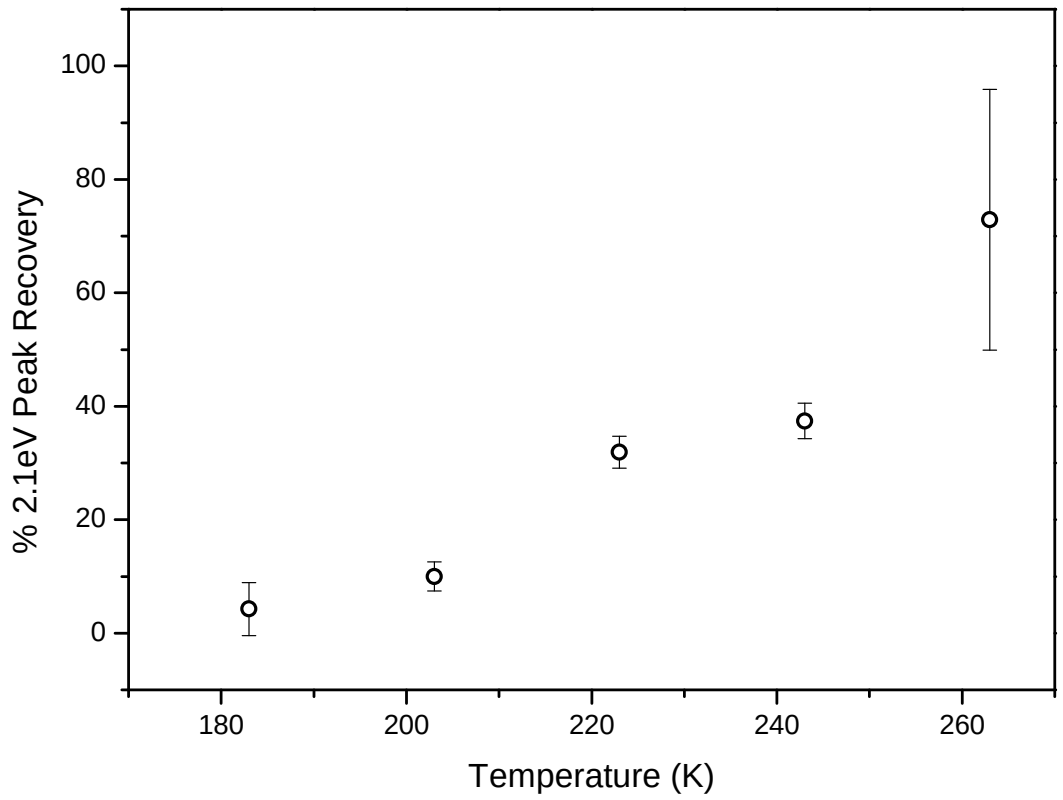

Figure 8.2 Experimental results of % 2.1eV peak recovery with temperature.

time for various temperatures. Figure 8.2 shows that the percentage of the peak which is recovered increases with temperature.

As loss of the intensity of the 2.1eV peak can be thought of as representing damage due to defects on the surface it can be seen in the results that over time the surface repairs itself after undergoing ion bombardment at finite temperatures. The recovery of the peak increases within the temperature range studied; as the repairing process is temperature dependent it can be deduced that the diffusion process is playing a significant role in this. This is because with higher temperatures the adatoms have higher mobility resulting in a greater probability that they will join step edges, recombine with vacancies, or join large clusters, all of which contribute to the recovery of the signal.

Figure 8.3 also illustrates the uncertainty in the ion flux as each surface was bombarded for ≈10 seconds but the initial decrease in signal varies considerably. This is partly due to errors in timing a 2 second burst of ions, and partly due to the fluctuating flux. This may affect the recovery of the peak as it is not known how dependent the recovery is on the initial amount if damage.

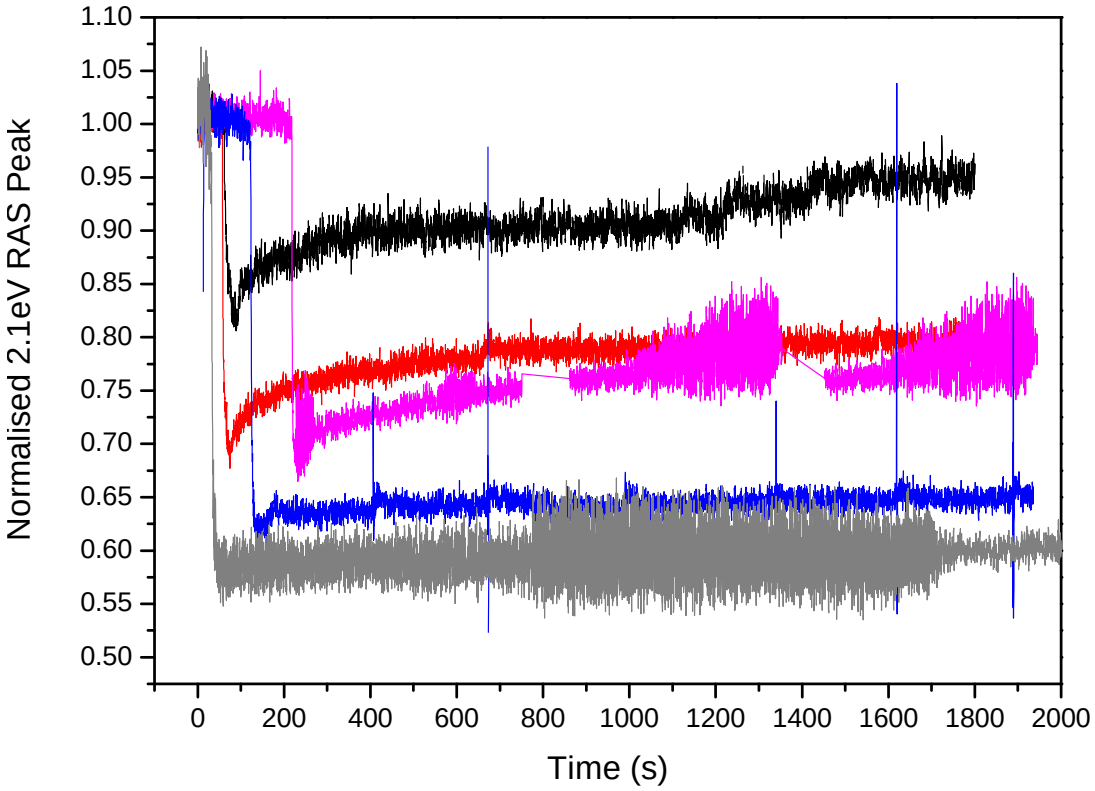

Figure 8.3 Experimental results of peak recovery with temperature at 183K (dark grey), 203K (blue), 223K (pink), 243K (red), and 263K (black) [81].

8.3 Modelling the Recovery

The surface was simulated in order to further explore the diffusion mechanisms which play the key role in the recovery of the RAS intensity.

To simulate peak recovery a 100×100 unit cell lattice (with a step edge) was bombarded at 0.0014 ions/unit cell/second for 2 seconds with a patch per defect size of $\Sigma_d = 7 \times 7$ unit cells. The program then simulated surface diffusion for a further 1800 seconds with the average 2.1eV peak recorded every 0.1 seconds using the Poelsema-Comsa model outlined in Sections 3.3 and 4.4.1 for a range of temperatures. The results at 144K are shown in Figure 8.4 where the peak recovery is clearly visible. The simulation was run for a number of temperatures, the results of which are shown in Figure 8.5.

The percentage recovery for each temperature was calculated and is presented in Figure 8.6. The recovery increases with temperature as is the case with experimental data discussed in Section 8.2. The amount of recovery seems to

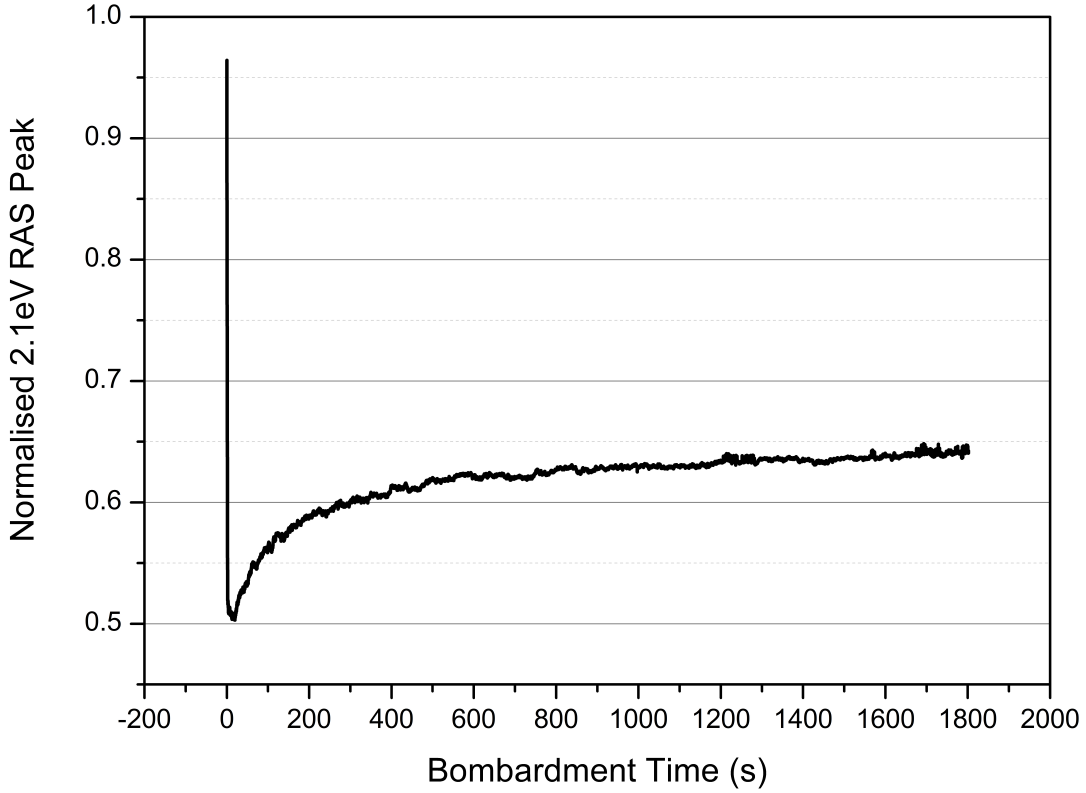

Figure 8.4 The recovery of 2.1eV peak at 144K. The simulated surface was bombarded for 2 seconds and then left to recover for half an hour.

be approximately constant between 155K and 180K.

By comparing Figures 8.2 and 8.6 the amount of peak recovery seems to be overestimated by the simulation, with 183K recovery at $\approx 25\%$ for simulation data and $\approx 5\%$ for experimental data. This suggests diffusion parameters are set too high in the simulation, which is further explored in Section 8.5.

A zoomed in plot of the simulation data for peak recovery after 8 seconds can be seen in Figure 8.7. For temperatures of 130K, 135K, and 144K the recovery rates look similar, but above these temperatures the recovery rate increases. This suggests a 'switch on' temperature where a process is activated in the 144K-155K region. This agrees with overall recovery results shown in Figure 8.6 where it was discussed earlier that above 144K the recovery plateaus, such that the processes with the next largest energy barriers are not being activated. By inspecting Figure 4.6, at these temperatures the simulation could be accessing processes 5 and 9 (illustrated in Figure 4.5) which were perhaps not active below 155K.

It can also be seen in Figure 8.7 that the 2.1eV peaks do not decrease to

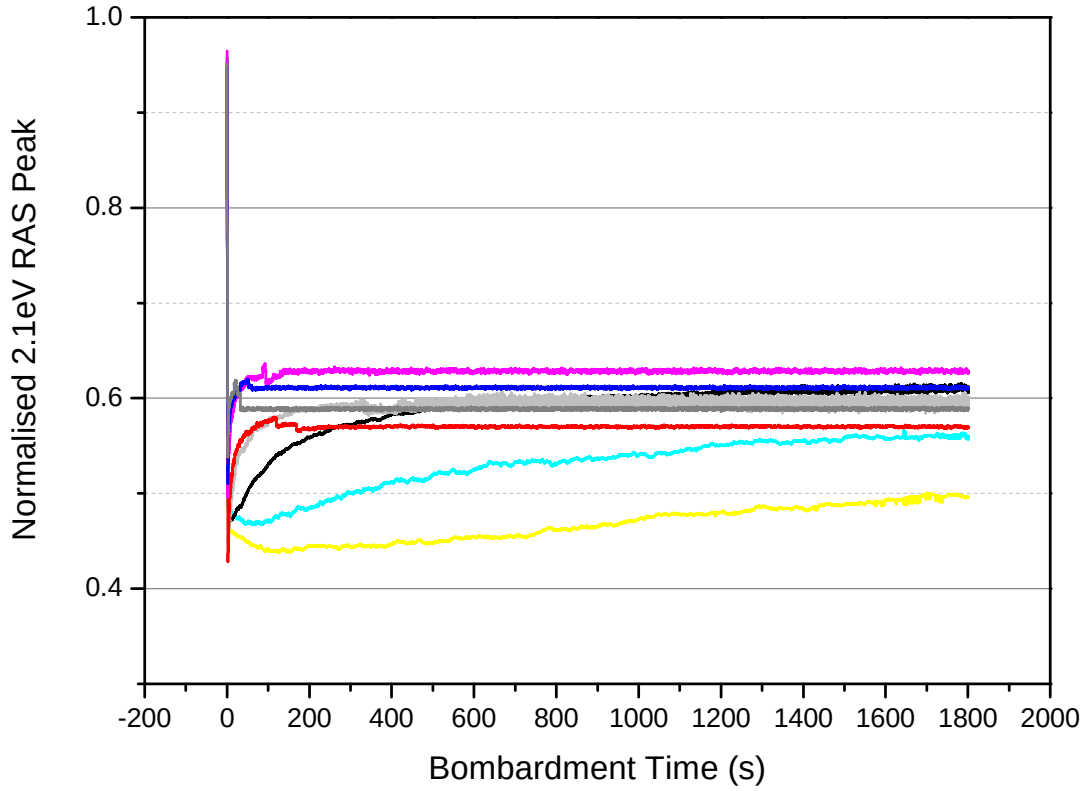

Figure 8.5 The results for peak recovery after 2 seconds of ion bombardment for 130K (yellow), 135K (light blue), 144K (black), 155K (light grey), 160K (red), 165K (pink), 170K (dark blue), and 180K (dark grey).

the same values for each temperature. This is partly due to different rates of diffusion during the bombardment process and also because of flux variation, where the program simulates the flux using probabilities and random numbers which introduce an inherent variation in each run, much like the experimental data.

8.4 Modelling STM Data

It was described in Section 3.4.1 how the RAS intensity was modelled using STM data, by Isted *et al.* [54]. The experimental RAS data was collected by bombarding the sample for a period of time and after ≈2 minutes the signal was recorded. This was repeated for bombardment times of up to 10 seconds at 2 minute intervals.

To simulate this data a 100×100 unit cell lattice (with a step edge) was

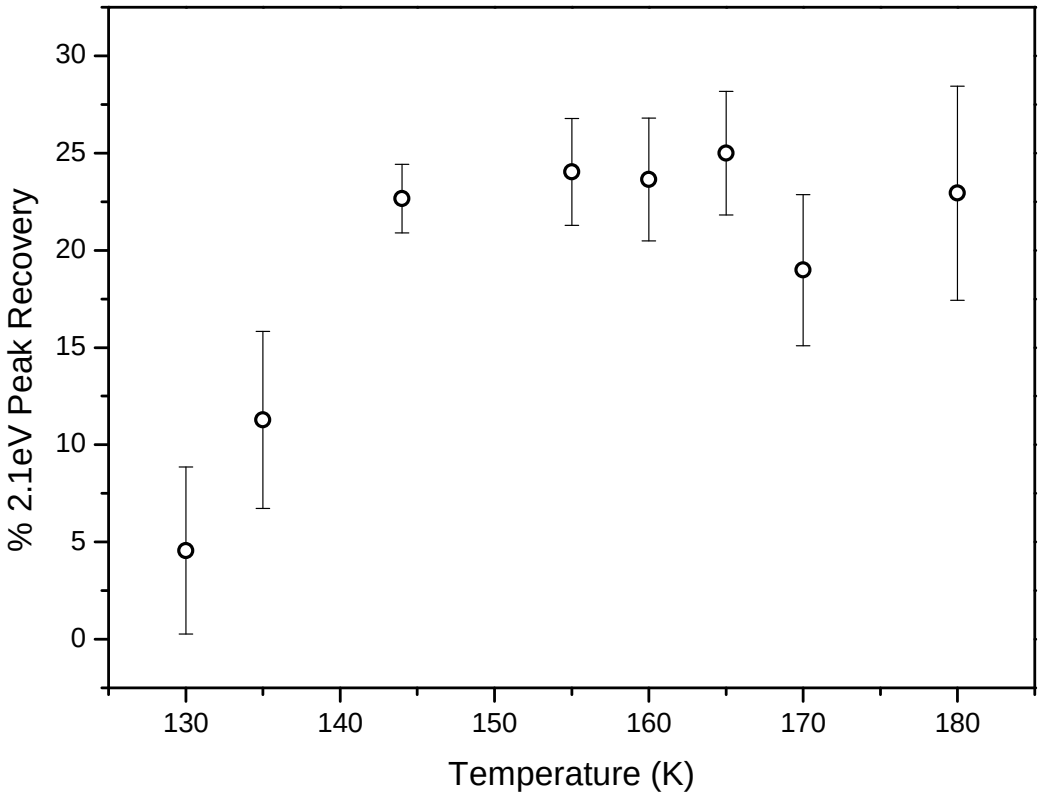

Figure 8.6 Simulation results of percentage of 2.1eV peak recovery with temperature

bombarded at the same intervals (of 2 seconds up to 10 seconds) at a flux of 0.0014 ions/unit cell/second with a patch per defect of 7×7 unit cells. Diffusion was then simulated for 2 minutes and a value of the RAS intensity recorded after this time. The results of this are shown in Figure 8.8.

The simulation results do not perfectly reproduce experimental results but are an improvement on using STM images [54] alone which were collected 30 minutes after the initial ion bombardment, as seen in Figure 3.9. The simulation seems to recover the peak too much which is possibly due to an overestimation of diffusivity, D, on the surface; this is consistent with what was previously found in Section 8.2.

8.5 Calculating the Diffusivity Constant

It was concluded in Sections 8.2, 8.3, and 8.4 that the simulated data was overestimating the surface diffusivity, D. One way to lower diffusivity is by decreasing the diffusion constant, D_0, as $D \propto D_0$ (by inspection of Equation 4.1);

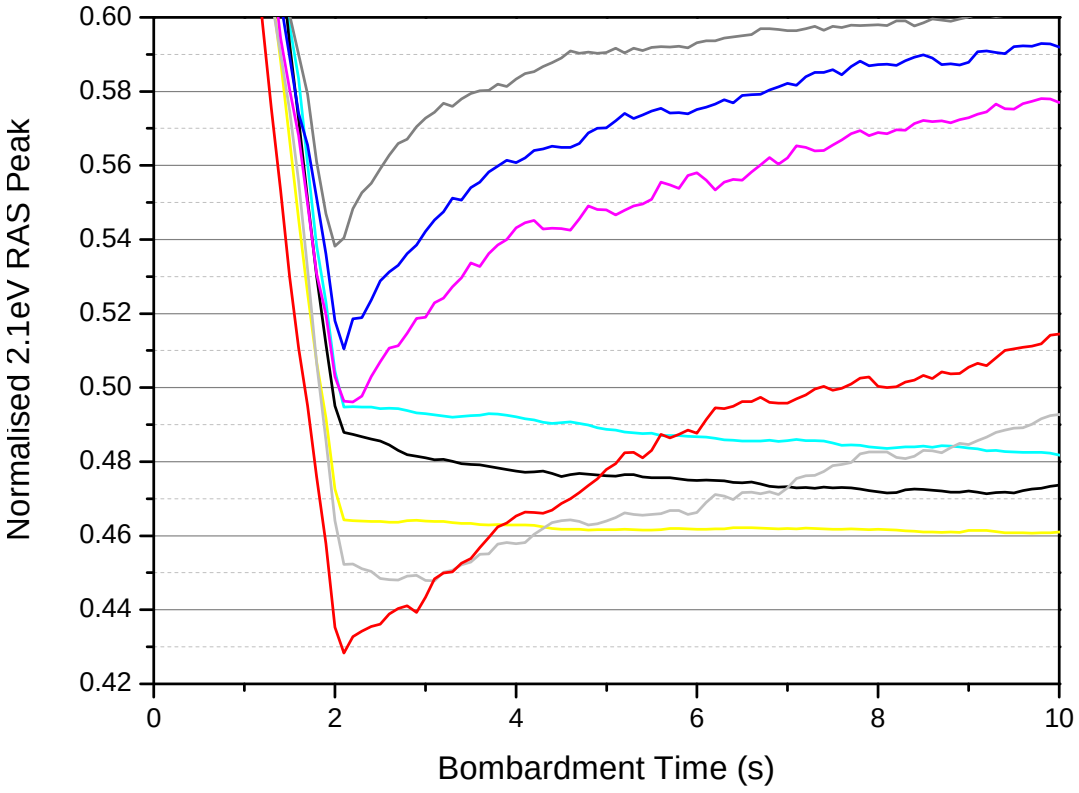

Figure 8.7 Graph showing the results for peak recovery 8 seconds after 2 seconds of ion bombardment for 130K (yellow), 135K (light blue), 144K (black), 155K (light grey), 160K (red), 165K (pink), 170K (dark blue), and 180K (dark grey).

this, however, assumes the surface energy barriers to be correct.

It is possible to calculate a new value for D_0 using the simulation and experimental recovery data. By comparing Figures 8.2 and 8.6 the graphs seem to agree when the simulation temperature (T_S) is ≈130K and the experimental temperature (T_E) is ≈180K. By assuming that when $T_E = 180\text{K}$ and $T_S = 130\text{K}$, D_{0E} (the experimental D_0), can be found by equating D_E and D_S, the experimental and simulation diffusivity. Then by rearranging Equation 4.1 we have

$$D_{0E} = \frac{D_{0S}}{\exp\left(\frac{E}{k_B}\left(\frac{1}{T_S} - \frac{1}{T_E}\right)\right)}, \tag{8.1}$$

where $D_{0S} = 6.29 \times 10^{-4}$ cm^2 s^{-1} [72] (which is the value for D_0 used in the simulation), k_B is the Boltzmann constant, and E is the energy barrier of the process being considered. For $E = 0.33\text{eV}$, which is the energy barrier for a single adatom hopping along a channel, the new value for the diffusion constant

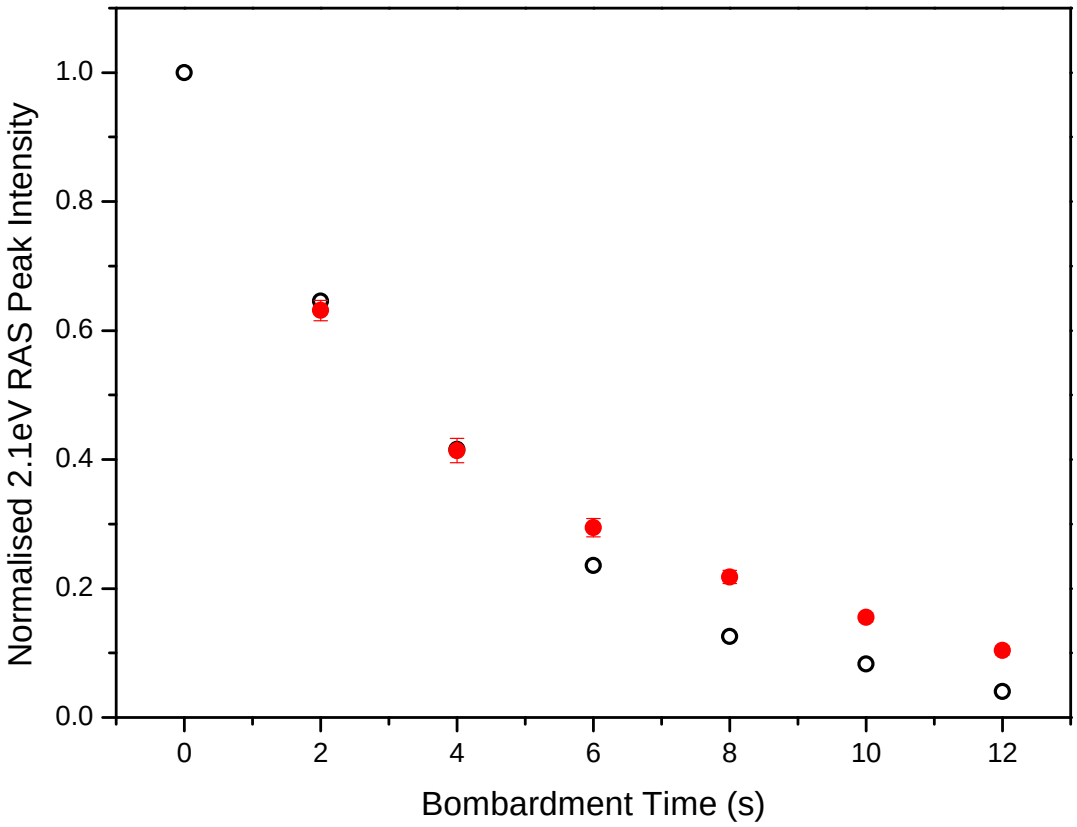

Figure 8.8 The normalised 2.1eV RAS signal after bombarding the surface and leaving to diffuse for 1min for simulation (red filled circles) and experimental (black open circles) results.

D_0 is

$$D_{0E} = 1.77 \times 10^{-7} \mathrm{cm}^2 \mathrm{s}^{-1} \,, \tag{8.2}$$

which is a factor of 10^{-3} lower than the value calculated by Yildirim *et al.* [72]. This value would also be affected if the initial clustering in the first few picoseconds after bombardment, demonstrated by Lane *et al.* [14], is included in the simulation.

8.5.1 Simulating the Ion Bombarded Surface with the New Diffusivity Constant

Figure 8.9 shows the simulated 183K ion bombarded surface with the new value for D_0 (D_{0E}) and a patch per defect of $\Sigma_d = 6 \times 6$ unit cells, and the the D_0 value calculated by Yildirim *et al.* [72] (D_{0S}) with a patch per defect of $\Sigma_d = 7 \times 7$ unit cells, and experimental data [35].

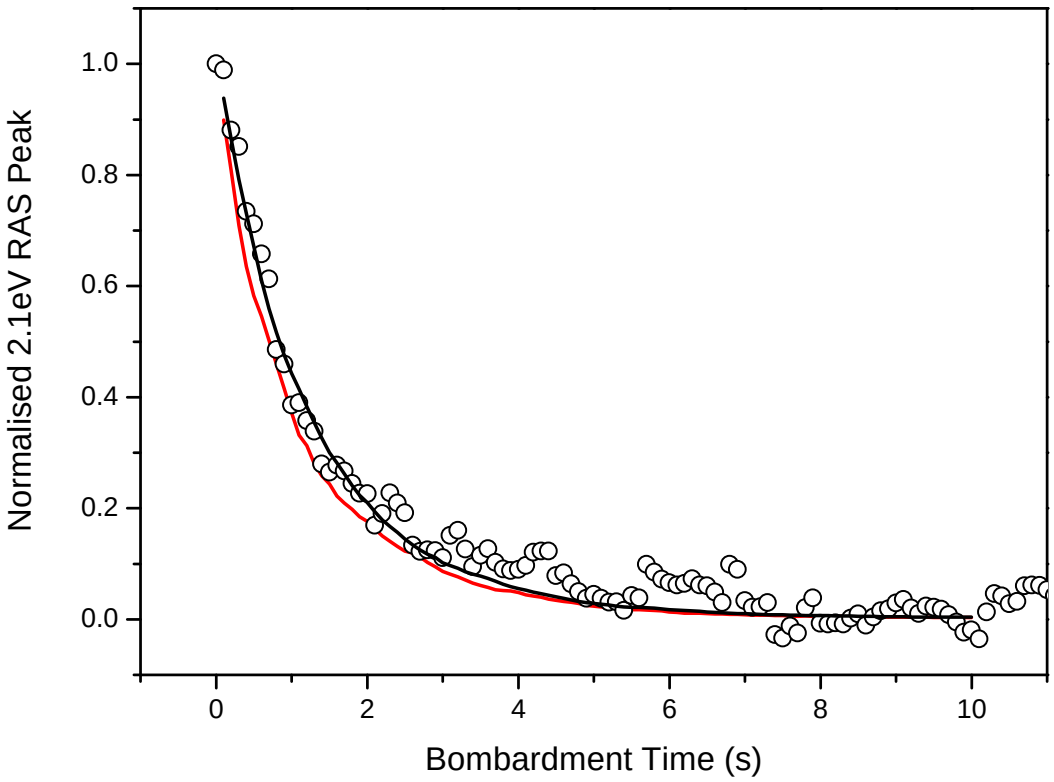

Figure 8.9 The RAS intensity with bombardment time at 183K for simulation data using a 7x7 patch per defect and the Yilidrim *et al.* [72] value for D_0 (red line), simulation data using a 6x6 patch per defect using the new value for D_0 (black line), and experimental data (circles) [35]

Using a value for D_0 calculated above and a patch per defect size of

$$\Sigma_d = 6 \times 6 \text{ unit cells} \tag{8.3}$$

the patch per impact, $\Sigma_I = 190 \pm 2$ unit cells, which was calculated by fitting the Poelsema-Comsa model to the data. This is within 1 error bar of the value calculated using the experimental data in Section 6.3.2 which was $\Sigma_I = 194 \pm 4$ unit cells.

The peak recovery was simulated using the new parameters at 183K, the results of this are shown in Figure 8.10. As can be seen from the graph, the simulation using a patch per defect of $\Sigma_d = 6 \times 6$ unit cells and the new value for D_0 recovers much slower, with a percentage peak recovery of $15 \pm 2\%$. The experimental peak recovery at this temperature is $4 \pm 5\%$ meaning that the recovery is still 2 error bars away from the experimental value. This is an improvement, though, on using the original parameters at 180K which gives a peak recovery of $22 \pm 5\%$ which is

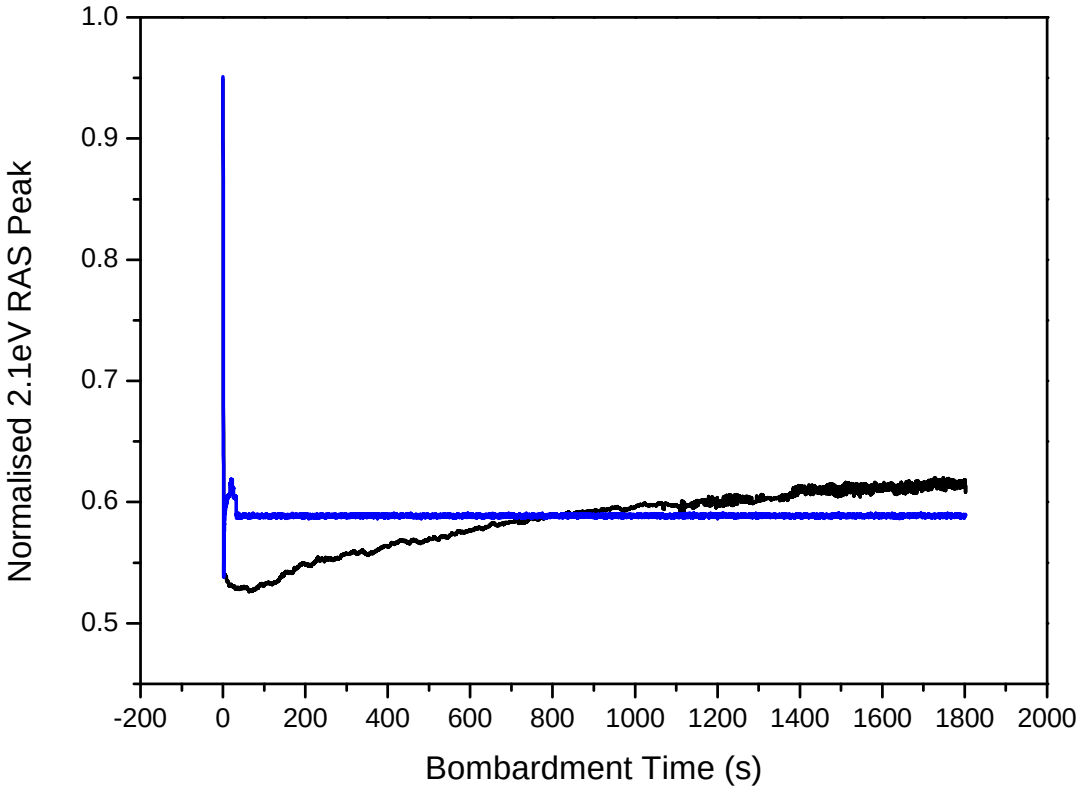

Figure 8.10 Simulated recovery at 180K using using a 7x7 patch per defect and the Yilidrim *et al.* [72] value for D_0 (blue), and using a 6x6 patch per defect using the new value for D_0 (black)

3 error bars away from the experimental value.

The process of finding D_{0E} can be repeated using Equation 8.1 where the recovery of the simulation at 180K is approximately equal to experimental recovery at 205K (this was found by fitting a linear trend to the data in Figure 8.2). Using $T_E = 205\text{K}$, $T_S = 205\text{K}$, and $D_{0S} = 1.77\times10^{-7}\text{cm}^2\text{s}^{-1}$ a new value of the diffusion constant for $E = 0.33\text{eV}$ is

$$D_{0E} = 1.32 \times 10^{-8}\text{cm}^2\text{s}^{-1}\,. \tag{8.4}$$

This new value is close to the previous calculated value for D_0 such that the value seems to be converging.

8.6 Discussion

The recovery of the RAS intensity on the Cu(110) surface has been successfully modelled at temperatures of 130K, 135K, 144K, 155K, 160K, 170K, and 180K. A transition is clearly seen in the data between 144K and 155K where the recovery rate changes from slow to relatively fast. This signifies a process (or processes) being activated at temperatures above 144K which is not dominant below this temperature. By inspecting Figure 4.6, at these temperatures the simulation could be accessing processes 5 and 9 (illustrated in Figure 4.5) which were perhaps not active below 155K.

When comparing experimental and simulation percentage peak recovery data after 30 minutes of surface diffusion, it was clear that the simulation overestimates the amount of recovery on the surface. This is probably due to too much diffusion occurring on the surface.

Experimental data at 144K has also been modelled where the surface was bombarded at specific time intervals and the 2.1eV peak recorded after 2 minutes of surface diffusion. When these were compared the simulation again overestimated recovery on the surface, and therefore the amount of diffusion.

As the analysis of simulation results in comparison with experimental results point to too much diffusion, *i.e.* the diffusivity D is too high, a new value for the diffusivity constant, D_0 was calculated. Using this new value for D_0 the surface was simulated with constant ion bombardment at 183K, for comparison with results in Chapter 6, and the patch per defect optimised to $\Sigma_d = 6 \times 6$ unit cells.

The surface recovery was then simulated with the new value of D_0 at 180K. The surface was seen to recover slower with the new D_0 value, which is closer to experimental results.

Chapter 9

Conclusions and Future Work

9.1 Conclusions

The aims of this thesis were to model the nanoscale kinetics of the ion bombarded Cu(110) surface. This has been achieved through the use of a KMC simulation which allows for longer simulation times than MD alone. The Poelsema-Comsa model was incorporated into the simulation in order to reproduce experimental RAS intensity results. Input parameters from MD simulations were used in the KMC simulation, other parameters such as patch per defect have been optimised using low temperature experimental RAS data.

This thesis has shown that the KMC simulation produced can model the nanoscale kinetics of the surface; this could prove useful as a tool in predicting surface behaviour and nanostructuring. Also shown is the importance of surface diffusion on nanostructuring with the improvements on modelling the surface using STM data [54], and MD data [14] by considering this.

In Chapter 6 the Cu(110) surface during ion bombardment was successfully simulated at temperatures of 183K and 203K using the Poelsema-Comsa model of the RAS intensity. This indicates that the flux, and patch per defect size were correctly calculated using the experimental data. It also indicates that the key diffusion processes were successfully identified for these temperatures and their corresponding energy barriers are correct. At the higher temperature of 223K the simulation did not predict the normalised peak as well as the lower temperature data. This could be due to an inaccuracy in the simulation, possibly

an overestimation of diffusivity, with D_0 being too high.

After analysis of residuals it was concluded that the Poelsema-Comsa model is missing a parameter which was assumed to be diffusion. By analysing the patch per impact over bombardment time, and comparing experimental results with simulation results, it was concluded that diffusion may play a role in the trend seen in the residual data. Though this method for analysing RAS data seems non-trivial, with features in the data still unexplained. More investigation may provide a way of monitoring surface diffusion using experimental RAS data alone.

In Chapter 7 the nanostructuring of the ion bombarded Cu(110) surface was analysed using STM images and KMC simulations. A new technique for image analysis was described along with cluster analysis results. This new technique was deemed more suitable as it considered the whole imaged surface.

The surface was simulated in order to reproduce STM experimental results with the new analysis. The KMC simulation was shown to be more effective in modelling the surface than MD alone, showing that longer times scales were needed to reproduce the experimental STM results. A diffusion parameter seemed to be too high as after 30 minutes of diffusion the simulated surface underestimated the number of small adatom clusters when compared to experimental results. This could be due to the diffusivity constant, D_0 being too high, which is in agreement with previous results.

The number of adatoms which make up different cluster sizes was recorded for various diffusion times. The nanostructure of the surface was seen to change quickly, with other processes occurring more gradually after the first ≈ 10 seconds. This time scale of cluster evolution is interesting as this has implications when experimental measurements of the surface structure are taken, such as when recording RAS data. After damaging the surface, results in this thesis suggest measurements need to be taken quickly in order to obtain a true picture of the surface immediately after ion bombardment.

In Chapter 8 the recovery of the RAS intensity on the Cu(110) surface was successfully modelled at temperatures of 130K to 180K. The data showed a transition at a temperature of $\approx$ 144K where the recovery rate changes from slow to relatively fast.

When comparing experimental and KMC simulation data of percentage peak recovery after 30 minutes of surface diffusion, it was clear that the simulation

overestimates the amount of surface state recovery. This is possibly due to too much diffusion occurring on the surface or too many recombinations. Experimental data at 144K was also modelled and, again, overestimated recovery, and therefore the amount of diffusion.

As the analysis of simulation results in comparison with experimental results point to a diffusion parameter being too large, a new value for the diffusivity constant, D_0 was calculated. Using this new value for D_0 the surface was simulated with constant ion bombardment at 183K, and a new patch per defect optimised to $\Sigma_d = 6 \times 6$ unit cells. The surface recovery was then simulated with the new value of D_0 at 180K. This affected results, and the surface is seen to recover slower with the new D_0 value.

Many of the results in this thesis suggest the diffusivity constant used is too high at these temperatures. This leads to a decreased patch per defect size of $\Sigma_d = 6 \times 6$ unit cells when the simulation was re-optimised. It is also possible the initial placement of adatoms on the surface is not sophisticated enough, with adatoms being placed randomly within an ejection range of the impact site. MD simulations [14] show us that on the nanosecond time scale some diffusion and clustering of the adatoms occur which the KMC simulation does not take account of. This extra initial clustering would likely result in less single adatoms diffusing on the surface.

9.2 Future Work

It would be of interest to reproduce all KMC simulation results with the new value of D_0 calculated in Chapter 8 using a patch size of $\Sigma_d = 6 \times 6$ unit cells. This would possibly confirm the overestimation of diffusion on the surface using the D_0 value calculated by Yildirim *et al.* [72]. The discrepancy in the amount of diffusion could also be due to inaccuracies in the surface energy barriers (where a key diffusion process energy barriers could have been underestimated), as such it would be interesting to explore this further to find where the overestimation originates from.

An improvement to the simulation would be to use results from MD simulations [14] to construct the initial bombarded surface structure. This would possibly lead to less adatom migration as the defects are less active where initially more

adatoms form clusters. This would effect the clustering of adatoms on the surface and would be of interest to simulate the RAS intensity and also investigate the clustering profile after these changes.

To reach higher temperatures in order to recreate experimental RAS results the program needs to perform faster. A way to do this would be to parallelise the program which would allow it to run on multiple cores.

Once the program is parallelised it would be interesting to run the simulation at room temperature, as the RAS intensity is seen to remain constant at these high temperatures. More processes would possibly need to be considered at high temperatures such as the creation of thermal defects, vacancy migration, and cluster diffusion. This could also allow the analysis of the 4eV region in the RAS spectra which evolves on much larger time scales ($\sim$ 1000s) [46].

It would be of interest to simulate another fcc(110) surface such as gold using the surface energy barriers and diffusivity constant which are associated with this surface. The 1.7eV in the RAS spectrum of Ag(110) has shown to be sensitive to surface defects [10, 25, 82] which would make it interesting to use the model created to simulate this peak by changing input parameters.

It has been shown in this thesis that by plotting the patch per impact, Σ_I, with bombardment time may give us a novel way of measuring diffusion on the surface using RAS data alone. There are still unknowns in this method of analysing the data and interpretation does not seem to be trivial. Investigating this further may give a new way of measuring the average nanostructure of the surface using RAS data.

The simulation created could be used to model Cu adatoms being deposited onto the Cu(110), where instead of having a crater with every ion impact, a single adatom could be placed on the surface instead. This could provide a way of simulating the growth of Cu monolayers and island formation on the surface.

The Poelsema-Comsa model used in this thesis places a patch, Σ_d, on each defect. The defect is said to destroy surface states which contribute towards the 2.1eV peak within this patch. The surface states involved are shown in Figure 3.4, but it is not obvious if the occupied band is destroyed over the same area as the unoccupied band. Angle-resolved photoemission spectroscopy [83] currently tells us the quenching area of the occupied band, Σ_o, and inverse photoemission spectroscopy [51] tells us the quenching area of the unoccupied band, Σ_u, whereas

RAS tells us a function of both of these where

$$\Sigma_d = f(\Sigma_o, \Sigma_u)\,. \tag{9.1}$$

It would be of interest to use the simulation to determine this function and find out which band, Σ_u or Σ_o, is dominant (*i.e.* which patch is bigger).

The model created is a step in further understanding the nanoscale structure and kinetics of the surface after ion bombardment. By taking into account higher energy radiation, this further characterisation of the RA response could help provide the information needed to make RAS a suitable technique in monitoring radiation damage in satellites and nuclear reactors.

Appendix A

Residuals

A.1 Experimental Data and Poelsema-Comsa Fit

The residuals for the experimental data and the fit have been analysed and presented here for various temperatures.

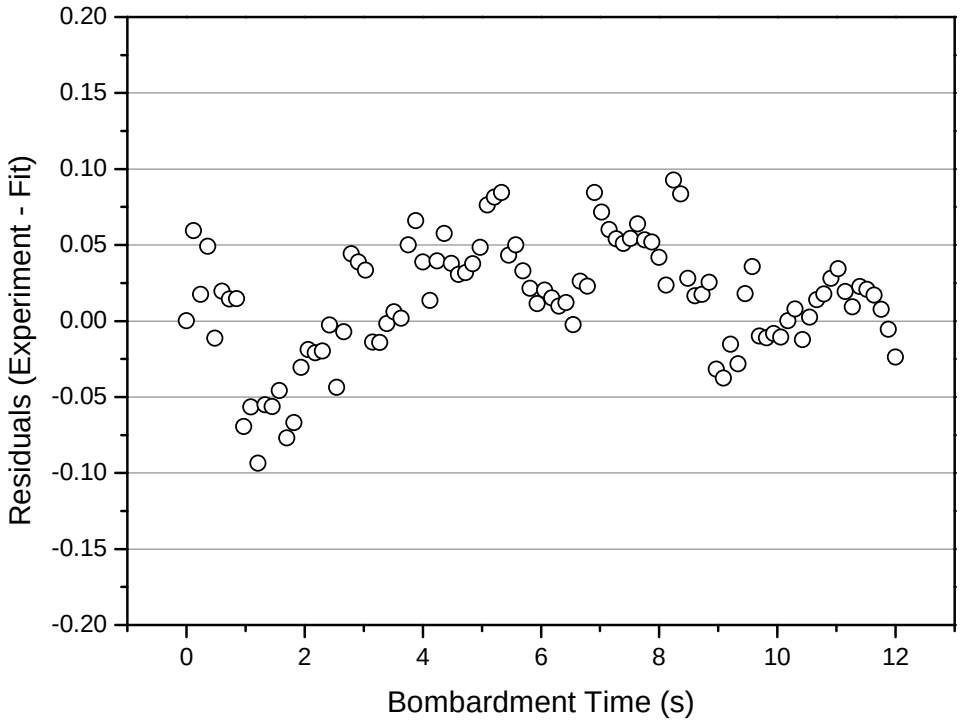

Figure A.1 Residuals of the experiment−the Poelsema-Comsa fit at 183K.

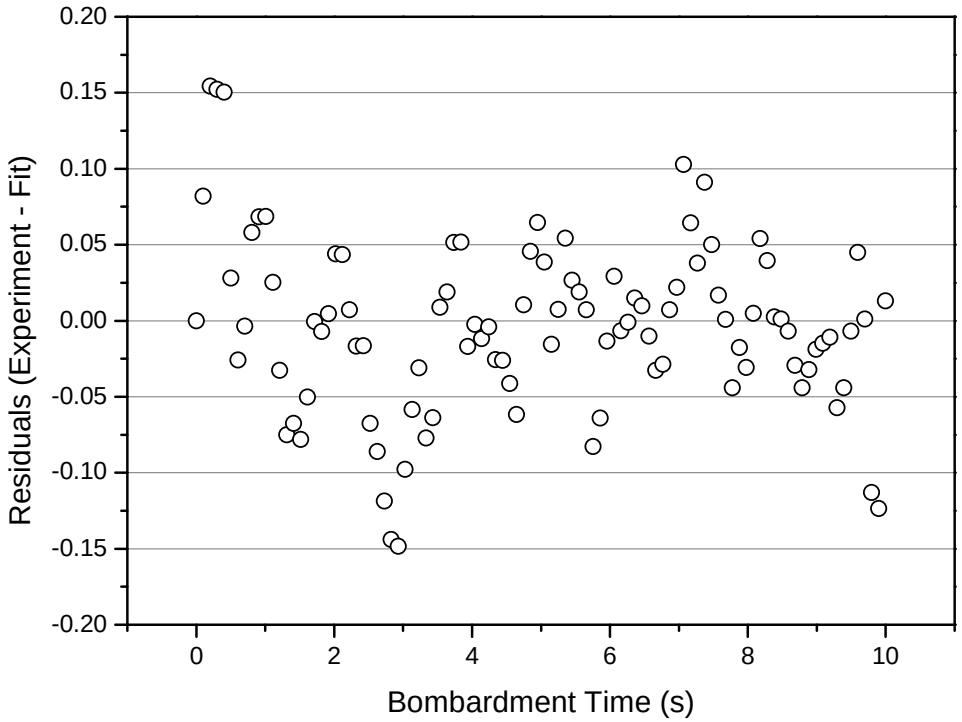

Figure A.2 Residuals of the experiment−the Poelsema-Comsa fit at 203K.

If the fit were perfect then we would expect the residuals to look like noise centred around zero on the y axis. This looks to be the case for the 183K and 203K data in Figures A.1 and A.2 respectively, and perhaps shows a small trend between bombardment times of 0 to 4 seconds. There is, however, an obvious trend is in the 223K and 243K data in Figures A.3 and A.4 respectively.

A.2 Simulation Data and Poelsema-Comsa Fit

The residuals for the experimental data and the fit have been analysed and presented here for various temperatures.

The residuals shown in Figures A.5, A.6, and A.7 show a trend similarly seen in the experiment residuals in Section A.1.

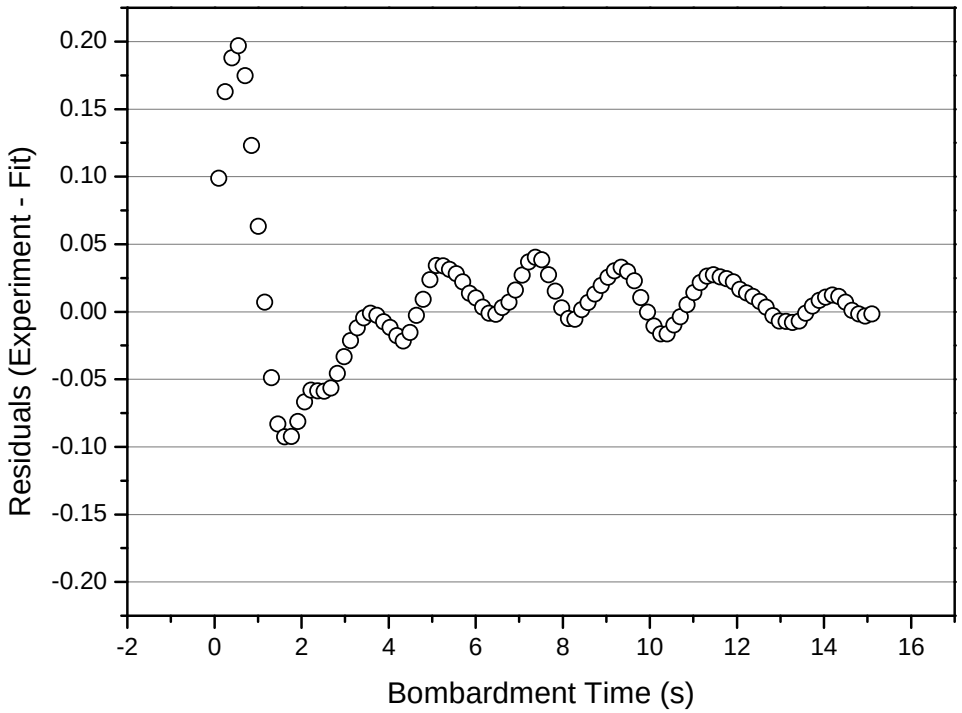

Figure A.3 Residuals of the experiment−the Poelsema-Comsa fit at 223K.

A.3 Experimental Data and Simulation Data

The residuals for the experimental data and the simulation data have been analysed and presented here for various temperatures in Figures A.8, A.9, and A.10.

There is again an obvious trend in the residuals which hints at a missing parameter.

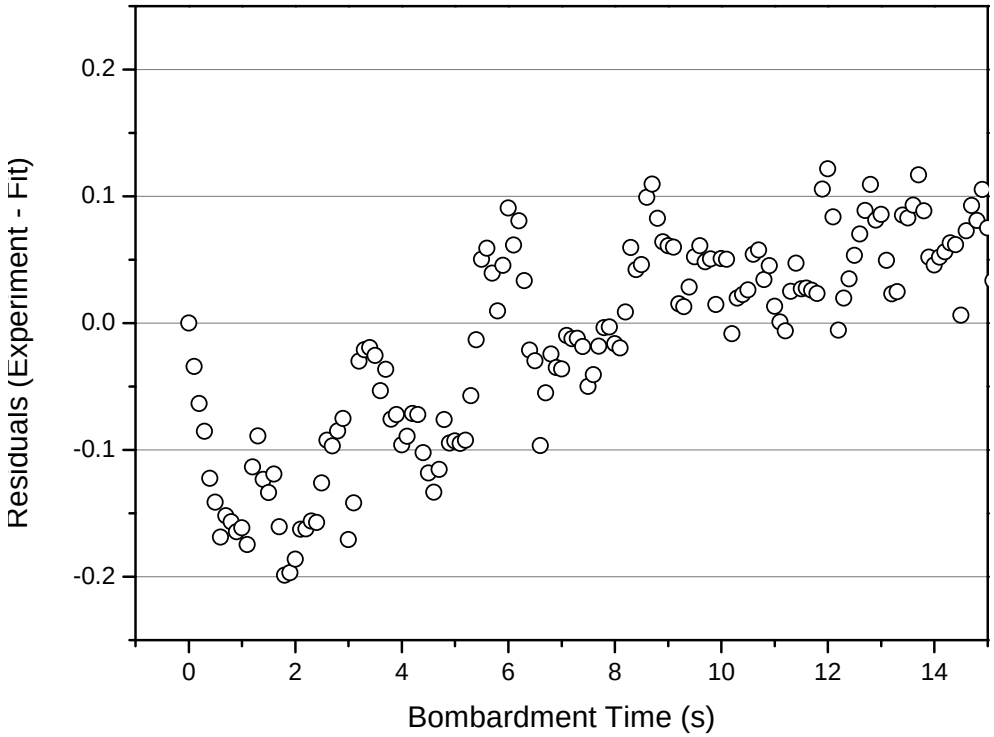

Figure A.4 Residuals of the experiment−the Poelsema-Comsa fit at 243K.

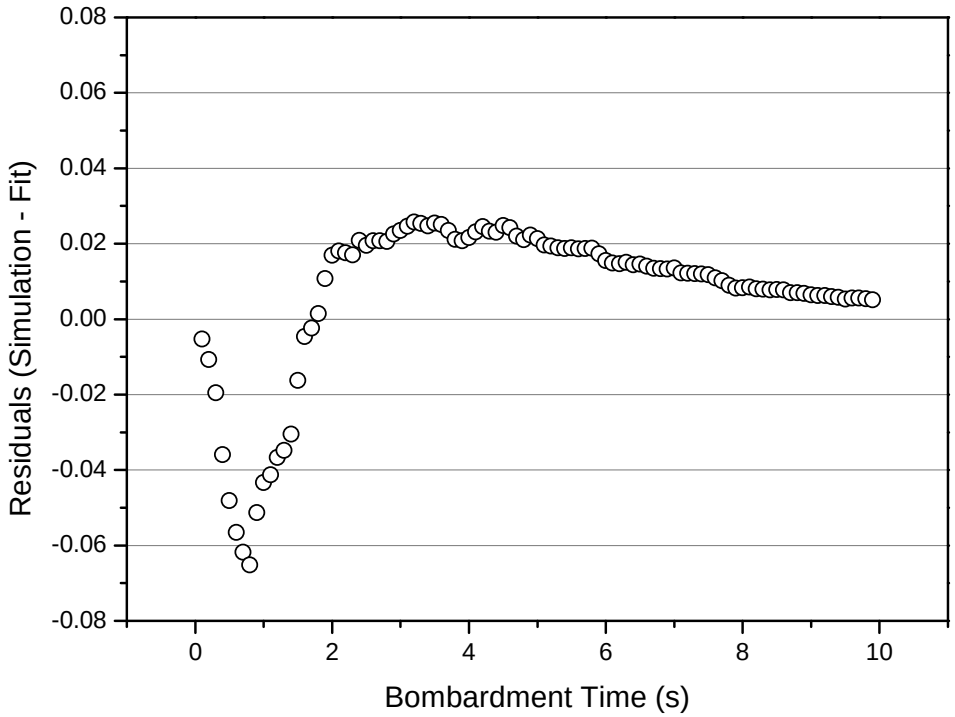

Figure A.5 Residuals of the the simulation−the fit at 183K.

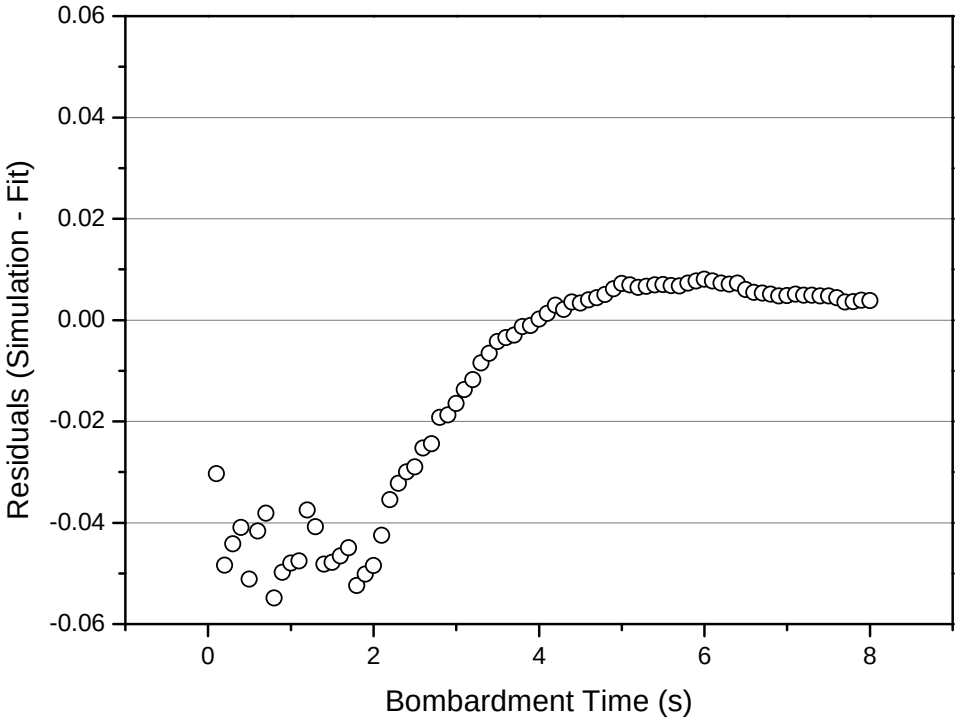

Figure A.6 Residuals of the the simulation−the fit at 203K.

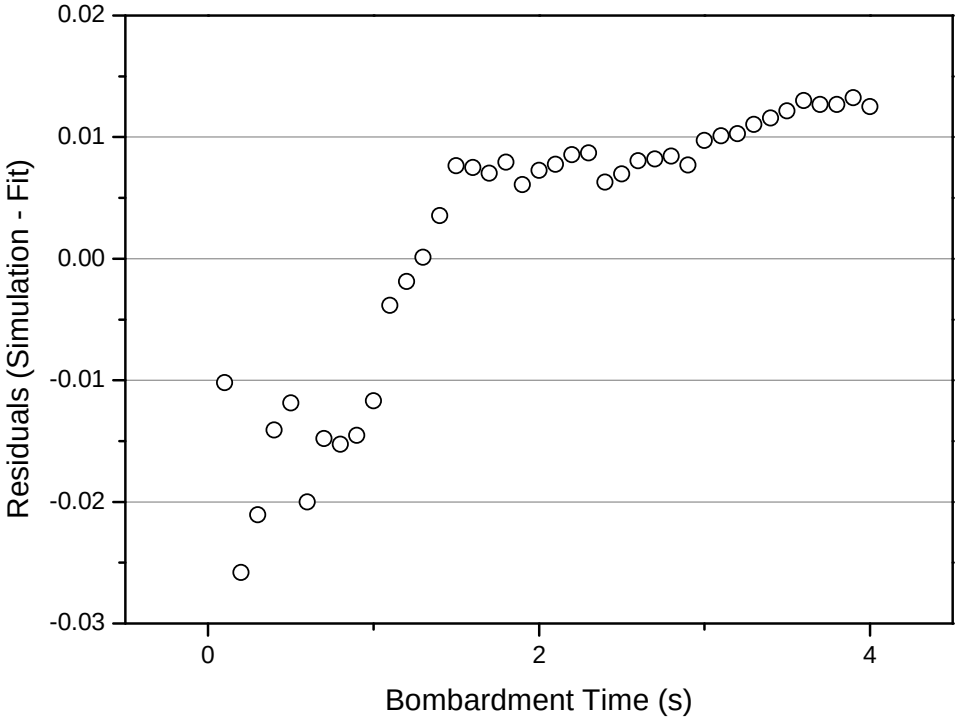

Figure A.7 Residuals of the the simulation−the fit at 223K.

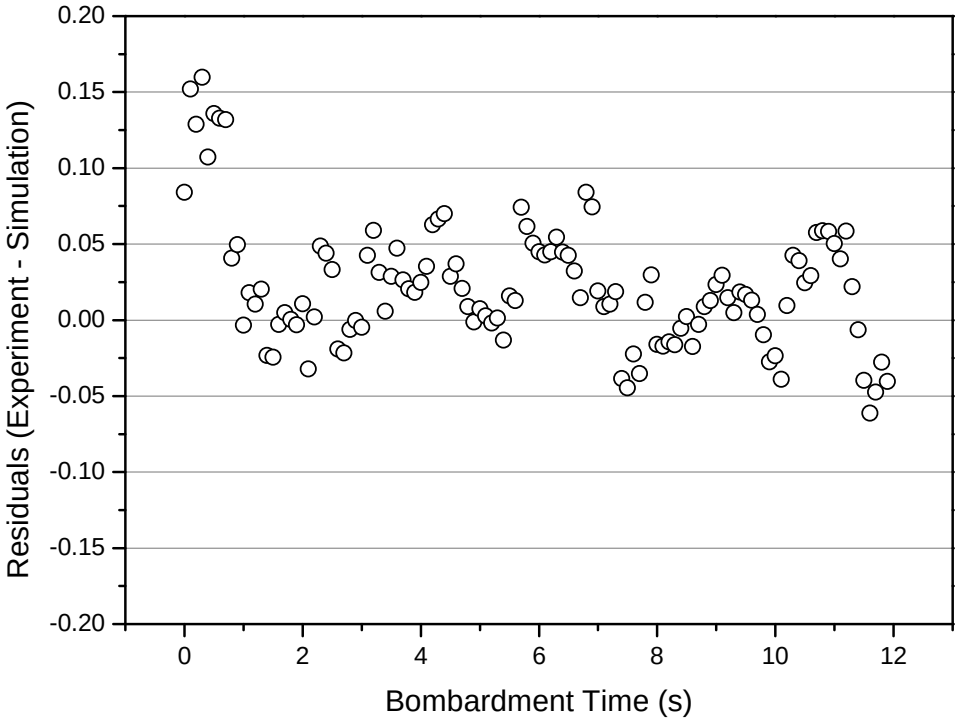

Figure A.8 Residuals of the the simulation−the experimental data at 183K.

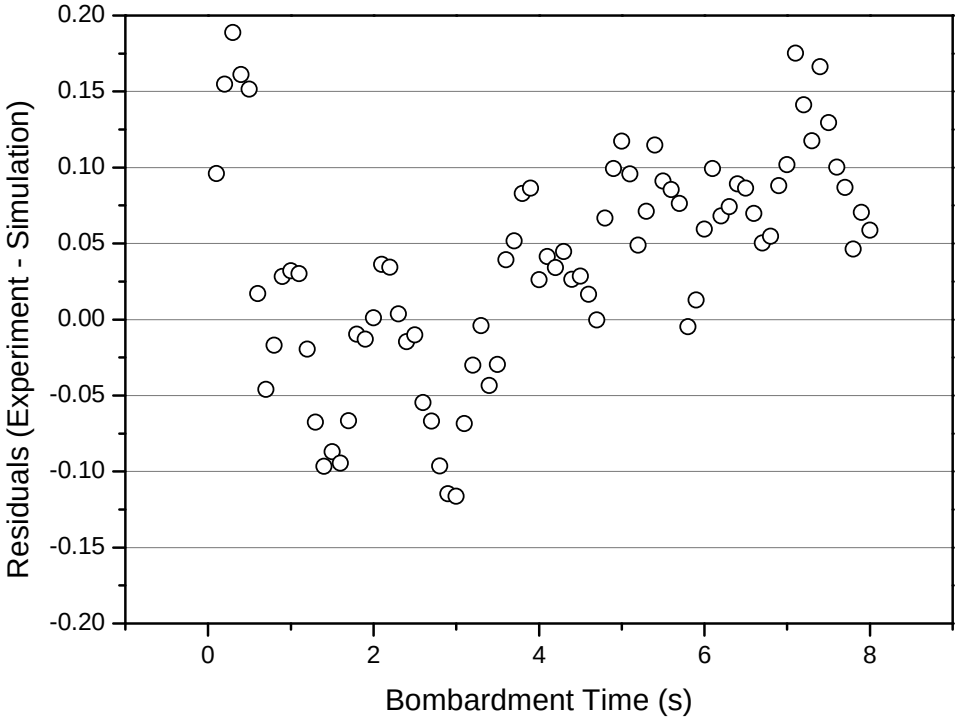

Figure A.9 Residuals of the the simulation−the experimental data at 203K.

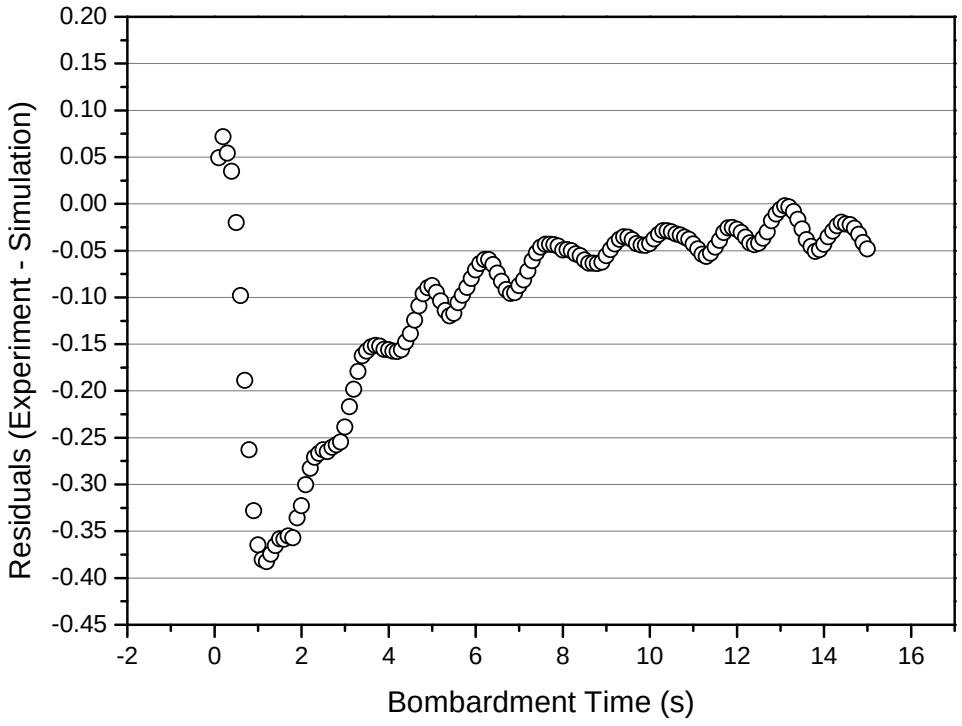

Figure A.10 Residuals of the the simulation−the experimental data at 223K.

Bibliography

[1] A. Zangwill. *Physics at Surfaces*. Cambridge University Press, Cambridge, 1988. ISBN 9780511622564. doi: 10.1017/CBO9780511622564. URL http://ebooks.cambridge.org/ref/id/CBO9780511622564.

[2] M. Prutton. *Introduction to Surface Physics*. OUP Oxford, Oxford, 1994. ISBN 0198534760.

[3] D. P. Woodruff and T. A. Delchar. *Modern Techniques of Surface Science*. Cambridge University Press, Cambridge, 1994. ISBN 9780511623172. doi: 10.1017/CBO9780511623172. URL http://ebooks.cambridge.org/ref/id/CBO9780511623172.

[4] G. Attard and C. Barnes. *Surfaces*. Oxford University Press, Oxford, 1998. ISBN 978 0 19 855686 2.

[5] J. F. McGilp. Optical characterisation of semiconductor surfaces and interfaces. *Progress in Surface Science*, 49(1):1–106, May 1995. ISSN 00796816. doi: 10.1016/0079-6816(95)00034-V. URL http://linkinghub.elsevier.com/retrieve/pii/007968169500034V.

[6] J. F. McGilp. Epioptics: progress and opportunity. *Thin Solid Films*, 313-314:533–536, February 1998. ISSN 00406090. doi: 10.1016/S0040-6090(97)00879-1. URL http://linkinghub.elsevier.com/retrieve/pii/S0040609097008791.

[7] J. E. Epler and H. P. Schweizer. Evolution of monolayer terrace topography during metalorganic chemical vapor deposition of (100) GaAs. *Applied Physics Letters*, 63(9):1228, 1993. ISSN 00036951. doi: 10.1063/1.109780. URL http://scitation.aip.org/content/aip/journal/apl/63/9/10.1063/1.109780.

[8] P. Chiaradia, A. Cricenti, S. Selci, and G. Chiarotti. Differential Reflectivity of Si(111)21 Surface with Polarized Light: A Test for Surface Structure. *Physical Review Letters*, 52(13):1145–1147, March 1984. ISSN 0031-9007. doi: 10.1103/PhysRevLett.52.1145. URL http://link.aps.org/doi/10.1103/PhysRevLett.52.1145.

[9] C. J. Sandroff, F. S. Turco-Sandroff, L. T. Florez, and J. P. Harbison. Recombination at GaAs surfaces and GaAs/AlGaAs interfaces probed by in situ photoluminescence. *Journal of Applied Physics*, 70(7):3632, 1991. ISSN 00218979. doi: 10.1063/1.349210. URL http://scitation.aip.org/content/aip/journal/jap/70/7/10.1063/1.349210.

[10] P. Weightman, D. S. Martin, R. J. Cole, and T. Farrell. Reflection anisotropy spectroscopy. *Reports On Progress In Physics*, 68(6):1251–1341, June 2005. ISSN 0034-4885. doi: 10.1088/0034-4885/68/6/R01. URL http://stacks.iop.org/0034-4885/68/i=6/a=R01?key=crossref.9f3f83b73e7780e0222afa7d75f7703f.

[11] M. Samaras, P. Derlet, H. Van Swygenhoven, and M. Victoria. Computer Simulation of Displacement Cascades in Nanocrystalline Ni. *Physical Review Letters*, 88(12):125505, March 2002. ISSN 0031-9007. doi: 10.1103/PhysRevLett.88.125505. URL http://link.aps.org/doi/10.1103/PhysRevLett.88.125505.

[12] M. Demkowicz, R. Hoagland, and J. Hirth. Interface Structure and Radiation Damage Resistance in Cu-Nb Multilayer Nanocomposites. *Physical Review Letters*, 100(13):136102, April 2008. ISSN 0031-9007. doi: 10.1103/PhysRevLett.100.136102. URL http://link.aps.org/doi/10.1103/PhysRevLett.100.136102.

[13] K. Henriksson, K. Nordlund, and J. Keinonen. Annihilation of craters: Molecular dynamic simulations on a silver surface. *Physical Review B*, 76(24):245428, December 2007. ISSN 1098-0121. doi: 10.1103/PhysRevB.76.245428. URL http://link.aps.org/doi/10.1103/PhysRevB.76.245428.

[14] P. D. Lane, G. J. Galloway, R. J. Cole, M. Caffio, R. Schaub, and G. J. Ackland. Validating molecular dynamics with direct imaging of radiation damage debris. *Physical Review B*, 85(9):094111, March 2012. ISSN 1098-0121. doi: 10.1103/PhysRevB.85.094111. URL http://link.aps.org/doi/10.1103/PhysRevB.85.094111.

[15] M. Wassermeier. Optical spectroscopy of (001) GaAs and AlAs under molecular-beam epitaxy growth conditions. *Journal of Vacuum Science & Technology B: Microelectronics and Nanometer Structures*, 9(4):2263, July 1991. ISSN 0734211X. doi: 10.1116/1.585731. URL http://link.aip.org/link/?JVB/9/2263/1&Agg=doi.

[16] J. R. Power, P. Weightman, S. Bose, A. Shkrebtii, and R. Del Sole. Sensitivity of Reflectance Anisotropy Spectroscopy to the Orientation of Ge Dimers on Vicinal Si(001). *Physical Review Letters*, 80(14):3133–3136, April 1998. ISSN 0031-9007. doi: 10.1103/PhysRevLett.80.3133. URL http://link.aps.org/doi/10.1103/PhysRevLett.80.3133.

[17] S. G. Jaloviar, J. Lin, F. Liu, V. Zielasek, L. McCaughan, and M. G. Lagally. Step-Induced Optical Anisotropy of Vicinal Si(001). *Physical Review Letters*,

82(4):791–794, January 1999. ISSN 0031-9007. doi: 10.1103/PhysRevLett.82.791. URL http://link.aps.org/doi/10.1103/PhysRevLett.82.791.

[18] J. R. Power, T. Farrell, P. Gerber, S. Chandola, P. Weightman, and J. F. McGilp. The influence of monolayer coverages of Sb on the optical anisotropy of vicinal Si(001). *Surface Science*, 372(1-3):83–90, February 1997. ISSN 00396028. doi: 10.1016/S0039-6028(96)01111-9. URL http://linkinghub.elsevier.com/retrieve/pii/S0039602896011119.

[19] P. D. Lane, D. S. Martin, D. Hesp, G. E. Isted, and R. J. Cole. Effects of steps and ordered defects on Cu(110) surface states. *Physical Review B*, 87 (24):245405, June 2013. ISSN 1098-0121. doi: 10.1103/PhysRevB.87.245405. URL http://link.aps.org/doi/10.1103/PhysRevB.87.245405.

[20] D. S. Martin. Optical reflectance anisotropy of the Si/Cu(110) surface alloy. *Journal of physics. Condensed matter : an Institute of Physics journal*, 21 (40):405003, October 2009. ISSN 1361-648X. doi: 10.1088/0953-8984/21/40/405003. URL http://www.ncbi.nlm.nih.gov/pubmed/21832405.

[21] D. E. Aspnes. Application of reflectance difference spectroscopy to molecular-beam epitaxy growth of GaAs and AlAs. *Journal of Vacuum Science & Technology A: Vacuum, Surfaces, and Films*, 6(3):1327, May 1988. ISSN 07342101. doi: 10.1116/1.575694. URL http://link.aip.org/link/?JVA/6/1327/1&Agg=doi.

[22] P. D. Lane, G. E. Isted, and R. J. Cole. Effect of surface defects and adsorbates on the optical anisotropy of Cu(110). *Physical Review B*, 82(7):75416, August 2010. ISSN 1098-0121. doi: 10.1103/PhysRevB.82.075416. URL http://link.aps.org/doi/10.1103/PhysRevB.82.075416.

[23] D. S. Martin, A. Maunder, and P. Weightman. Thermal behavior of the Cu(110) surface studied by reflection anisotropy spectroscopy and scanning tunneling microscopy. *Physical Review B*, 63(15):155403, April 2001. ISSN 0163-1829. doi: 10.1103/PhysRevB.63.155403. URL http://link.aps.org/doi/10.1103/PhysRevB.63.155403.

[24] L. D. Sun, M. Hohage, P. Zeppenfeld, and R. E. Balderas-Navarro. Origin and temperature dependence of the surface optical anisotropy on Cu(110). *Surface Science*, 589(1-3):153–163, September 2005. ISSN 00396028. doi: 10.1016/j.susc.2005.05.059. URL http://linkinghub.elsevier.com/retrieve/pii/S0039602805006102.

[25] G. E. Isted, P. D. Lane, and R. J. Cole. Effect of thermally induced surface defects on the optical anisotropy of Ag(110). *Physical Review B*, 79(20):205424, May 2009. ISSN 1098-0121. doi: 10.1103/PhysRevB.79.205424. URL http://link.aps.org/doi/10.1103/PhysRevB.79.205424.

[26] D. S. Martin, R. J. Cole, and S. Haq. Creating a functionalized surface: The adsorption of terephthalic acid onto Cu(110). *Physical Review B*, 66(15):

155427, October 2002. ISSN 0163-1829. doi: 10.1103/PhysRevB.66.155427. URL http://link.aps.org/doi/10.1103/PhysRevB.66.155427.

[27] L. D. Sun, M. Hohage, P. Zeppenfeld, R. E. Balderas-Navarro, and K. Hingerl. Enhanced optical sensitivity to adsorption due to depolarization of anisotropic surface states. *Physical Review Letters*, 90(10):106104, March 2003. ISSN 0031-9007. doi: 10.1103/PhysRevLett.90.106104. URL http://link.aps.org/doi/10.1103/PhysRevLett.90.106104.

[28] D. E. Aspnes and A. A. Studna. Anisotropies in the Above-Band-Gap Optical Spectra of Cubic Semiconductors. *Phys. Rev. Lett.*, 54(17):1956–1959, April 1985. doi: 10.1103/PhysRevLett.54.1956.

[29] D. E. Aspnes. Above-bandgap optical anisotropies in cubic semiconductors: A visiblenear ultraviolet probe of surfaces. *Journal of Vacuum Science & Technology B: Microelectronics and Nanometer Structures*, 3(5):1498, September 1985. ISSN 0734211X. doi: 10.1116/1.582974. URL http://link.aip.org/link/?JVB/3/1498/1&Agg=doi.

[30] D. E. Aspnes and A. A. Studna. Reflectance difference spectroscopy of (110) GaAs and InP. *Journal of Vacuum Science & Technology A: Vacuum, Surfaces, and Films*, 5(4):546, July 1987. ISSN 07342101. doi: 10.1116/1.574669. URL http://link.aip.org/link/?JVA/5/546/1&Agg=doi.

[31] J. P. Harbison, D. E. Aspnes, A. A. Studna, L. T. Florez, and M. K. Kelly. Oscillations in the optical response of (001)GaAs and AlGaAs surfaces during crystal growth by molecular beam epitaxy. *Applied Physics Letters*, 52(24):2046, 1988. ISSN 00036951. doi: 10.1063/1.99576. URL http://link.aip.org/link/APPLAB/v52/i24/p2046/s1&Agg=doi.

[32] Y. Borensztein, W. L. Mochan, J. Tarriba, R. G. Barrera, and A. Tadjeddine. Large anisotropy in the optical reflectance of Ag(110) single crystals: Experiment and theory. *Phys. Rev. Lett.*, 71(14):2334–2337, October 1993. doi: 10.1103/PhysRevLett.71.2334.

[33] B. F. Macdonald. *Reflection Anisotropy Spectroscopy and Scanning Probe Microscopy Studies with Applications to Liquid Crystal Alignment Layers*. PhD thesis, The University of Edinburgh, 2002.

[34] A. Chambers, R. K. Fitch, and B. S. Halliday. *Basic Vacuum Technology*. Institute of Physics Publishing, 2 edition, 1998.

[35] P. D. Lane. *Nanoscale Surface Modification studied by Reflection Anisotropy Spectroscopy*. PhD thesis, The University of Edinburgh, 2009.

[36] U. Rossow, L. Mantese, and D. E. Aspnes. Interpretation of surface-induced optical anisotropy of clean, hydrogenated, and oxidized vicinal silicon surfaces investigated by reflectance-difference spectroscopy. *Journal of Vacuum Science & Technology B*, 14(4):3070–3074, July 1996.

[37] G. Binnig, H. Rohrer, Ch. Gerber, and E. Weibel. Surface Studies by Scanning Tunneling Microscopy. *Physical Review Letters*, 49(1):57–61, July 1982. ISSN 0031-9007. doi: 10.1103/PhysRevLett.49.57. URL http://link.aps.org/doi/10.1103/PhysRevLett.49.57.

[38] G. Binnig, H. Rohrer, Ch. Gerber, and E. Weibel. Tunneling through a controllable vacuum gap. *Applied Physics Letters*, 40(2):178, 1982. ISSN 00036951. doi: 10.1063/1.92999. URL http://link.aip.org/link/?APL/40/178/1&Agg=doi.

[39] M. F. Crommie, C. P. Lutz, D. M. Eigler, and E. J. Heller. Waves on a metal surface and quantum corrals. *Surface Review and Letters*, 02(01):127–137, February 1995. ISSN 0218-625X. doi: 10.1142/S0218625X95000121. URL http://www.worldscientific.com/doi/abs/10.1142/S0218625X95000121.

[40] M. F. Crommie, C. P. Lutz, and D. M. Eigler. Imaging standing waves in a two-dimensional electron gas. *Nature*, 363(6429):524–527, June 1993. ISSN 0028-0836. doi: 10.1038/363524a0. URL http://www.nature.com/doifinder/10.1038/363524a0.

[41] M. F. Crommie, C. P. Lutz, and D. M. Eigler. Confinement of electrons to quantum corrals on a metal surface. *Science (New York, N.Y.)*, 262(5131):218–20, October 1993. ISSN 0036-8075. doi: 10.1126/science.262.5131.218. URL http://www.ncbi.nlm.nih.gov/pubmed/23787603.

[42] G. A. Fiete and E. J. Heller. Colloquium: Theory of quantum corrals and quantum mirages. *Reviews of Modern Physics*, 75(3):933–948, July 2003.

[43] Ph. Hofmann, K. C. Rose, V. Fernandez, A. M. Bradshaw, and W. Richter. Study of Surface States on Cu(110) Using Optical Reflectance Anisotropy. *Phys. Rev. Lett.*, 75(10):2039–2042, September 1995. ISSN 1079-7114. doi: 10.1103/PhysRevLett.75.2039. URL http://www.ncbi.nlm.nih.gov/pubmed/10059193.

[44] L. D. Sun, M. Hohage, P. Zeppenfeld, R. E. Balderas-Navarro, and K. Hingerl. Surface-induced d-band anisotropy on Cu(110). *Surface Science*, 527(1-3):L184—-L190, March 2003. ISSN 00396028. doi: 10.1016/S0039-6028(03)00024-4. URL http://linkinghub.elsevier.com/retrieve/pii/S0039602803000244.

[45] L. D. Sun, M. Hohage, and P. Zeppenfeld. Optical probe for surface and subsurface defects induced by ion bombardment. *physica status solidi (RRL) - Rapid Research Letters*, 7(4):301–304, April 2013. ISSN 18626254. doi: 10.1002/pssr.201307088. URL http://doi.wiley.com/10.1002/pssr.201307088.

[46] D. S. Martin, R. J. Cole, and P. Weightman. Effects of ion bombardment on the optical and electronic properties of Cu(110). *Physical Review B*, 72

(3):035408, July 2005. ISSN 1098-0121. doi: 10.1103/PhysRevB.72.035408. URL http://link.aps.org/doi/10.1103/PhysRevB.72.035408.

[47] H. Luth. *Solid Surfaces, Interfaces and Thin Films*. Springer-Verlag, 4th edition, 2001.

[48] M. Y. Jiang, G. Pajer, and E. Burstein. Role of Surface Electronic-transitions In Linear and Nonlinear Electromagnetic Phenomena At Noble-metal Surfaces - Beyond Jellium. *Surface Science*, 242(1-3):306–313, 1991.

[49] K. Stahrenberg, Th. Hermann, N. Esser, and W. Richter. Surface optical properties of clean Cu(110) and Cu(110)-(2 x 1)-{O}. *Physical Review B*, 61 (4):3043–3047, January 2000.

[50] P. Heimann, J. Hermanson, H. Miosga, and H. Neddermeyer. Photoemission observation of a new surface state band on Cu(110). *Surface Science*, 85(2):263–268, 1979. ISSN 0039-6028. doi: DOI:10.1016/0039-6028(79)90249-8. URL http://www.sciencedirect.com/science/article/pii/0039602879902498.

[51] R. A. Bartynski, T. Gustafsson, and P. Soven. Observation of an unoccupied surface state on Cu(110) by inverse photoemission. *Phys. Rev. B*, 31(8):4745–4750, April 1985. ISSN 0163-1829. doi: 10.1103/PhysRevB.31.4745. URL http://www.ncbi.nlm.nih.gov/pubmed/9936432.

[52] D. Heskett, D. DePietro, G. Sabatino, and M. Tammaro. Ion bombardment-induced changes in the electronic structure of Cu(110) investigated with inverse photoemission and computer simulations. *Surface Science*, 513(2):405–411, July 2002. ISSN 00396028. doi: 10.1016/S0039-6028(02)01808-3. URL http://linkinghub.elsevier.com/retrieve/pii/S0039602802018083.

[53] B. Poelsema and G. Comsa. *Scattering of Thermal Energy Atoms, Springer Tracts in Modern Physics*, volume 115. Springer, Berlin, 1989. ISBN 0-387-50358-7.

[54] G. E. Isted, P. D. Lane, R. J. Cole, M. Caffio, and R. Schaub. Estimating the range of influence of point defects on Cu (110) surface states. *Physical Review B*, 83(15):155403, April 2011. ISSN 1098-0121. doi: 10.1103/PhysRevB.83.155403. URL http://link.aps.org/doi/10.1103/PhysRevB.83.155403.

[55] D. V. Schroeder. *An Introduction To Thermal Physics*. Addison wesley Longman, 2000. ISBN 0-321-27779-1.

[56] B. Poelsema, L. Verheij, and G. Comsa. "Two-Layer" Behavior of the Pt(111) Surface during Low-Energy Arˆ{+}-Ion Sputtering at High Temperatures. *Physical Review Letters*, 53(26):2500–2503, December 1984. ISSN 0031-9007. doi: 10.1103/PhysRevLett.53.2500. URL http://link.aps.org/doi/10.1103/PhysRevLett.53.2500.

[57] T. Michely and G. Comsa. Temperature dependence of the sputtering morphology of Pt(111). *Surface Science*, 256(3):217–226, October 1991. ISSN 00396028. doi: 10.1016/0039-6028(91)90865-P. URL http://linkinghub.elsevier.com/retrieve/pii/003960289190865P.

[58] S. Rusponi, C. Boragno, and U. Valbusa. Ripple Structure on Ag(110) Surface Induced by Ion Sputtering. *Physical Review Letters*, 78(14):2795–2798, April 1997. ISSN 0031-9007. doi: 10.1103/PhysRevLett.78.2795. URL http://link.aps.org/doi/10.1103/PhysRevLett.78.2795.

[59] U. Valbusa, C. Boragno, and F. Buatier de Mongeot. Nanostructuring surfaces by ion sputtering. *Journal of Physics: Condensed Matter*, 14(35):8153–8175, September 2002. ISSN 0953-8984. doi: 10.1088/0953-8984/14/35/301. URL http://stacks.iop.org/0953-8984/14/i=35/a=301?key=crossref.7e54ea0e220118274445fe62d61fbfe3.

[60] J. Bremer, J. K. Hansen, and O. Hunderi. The effect of sputtering-induced disorder on the surface dielectric tensor of Cu(110). *Surface Science*, 436 (1-3):L735—-L739, August 1999.

[61] B. F. Macdonald and R. J. Cole. RAS as an in situ Monitor of Ion Bombardment. *physica status solidi (a)*, 188(4):1489–1493, December 2001. ISSN 0031-8965. doi: 10.1002/1521-396X(200112)188:4⟨1489::AID-PSSA1489⟩3.0.CO;2-B. URL http://doi.wiley.com/10.1002/1521-396X%28200112%29188%3A4%3C1489%3A%3AAID-PSSA1489%3E3.0.CO%3B2-B.

[62] R. Behrisch, H. H. Anderson, H. L. Bay, M. T. Robinson, H. E. Roosendaal, and P. Sigmund. *Sputtering by Particle Bombardment I*, volume 47 of *Topics in Applied Physics*. Springer Berlin Heidelberg, Berlin, Heidelberg, 1981. ISBN 978-3-540-10521-3. doi: 10.1007/3-540-10521-2. URL http://link.springer.com/10.1007/3-540-10521-2.

[63] G. Stoian, R. van Gastel, H. Wormeester, and B. Poelsema. Measurement of the sputter yield after mild ion erosion of a pristine Cu(001) surface. *Surface Science*, 606(21-22):1618–1622, November 2012. ISSN 00396028. doi: 10.1016/j.susc.2012.06.013. URL http://linkinghub.elsevier.com/retrieve/pii/S0039602812002324.

[64] J. M. Thijssen. *Computational Physics*. Cambridge University Press, Cambridge, 1999. ISBN 0 521 57588 5.

[65] M. Makeev and A. Barabasi. Ion-induced effective surface diffusion in ion sputtering. *Applied Physics Letters*, 71(19):2800, 1997. ISSN 00036951. doi: 10.1063/1.120140. URL http://link.aip.org/link/APPLAB/v71/i19/p2800/s1&Agg=doi.

[66] V. P. Zhdanov. Arrhenius parameters for rate processes on solid surfaces. *Surface Science Reports*, 12(5):185–242, May 1991. ISSN 01675729. doi: 10.1016/0167-5729(91)90011-L. URL http://linkinghub.elsevier.com/retrieve/pii/016757299190011L.

[67] K. Oura, V. G. Lifshits, A. Saranin, A. V. Zotov, and M Katayama. *Surface Science: An Introduction*. Springer-Verlag, Berlin, 2003. ISBN 9783540005452.

[68] D. T. Gillespie. A general method for numerically simulating the stochastic time evolution of coupled chemical reactions. *Journal of Computational Physics*, 22(4):403–434, December 1976. ISSN 00219991. doi: 10.1016/0021-9991(76)90041-3. URL http://linkinghub.elsevier.com/retrieve/pii/0021999176900413.

[69] D. T. Gillespie. Exact stochastic simulation of coupled chemical reactions. *The Journal of Physical Chemistry*, 81(25):2340–2361, December 1977. ISSN 0022-3654. doi: 10.1021/j100540a008. URL http://pubs.acs.org/doi/abs/10.1021/j100540a008.

[70] P. Stoltze. Simulation of Surface-defects. *Journal of Physics-condensed Matter*, 6(45):9495–9517, 1994.

[71] K. Sbiaai, Y. Boughaleb, A. Kara, S. Touhtouh, and B. Sahraoui. Long jumps contribution to the adatom diffusion process near the step edge: The case of Ag/Cu(110). *Physica Status Solidi (B)*, 251(4):838–844, April 2014. ISSN 03701972. doi: 10.1002/pssb.201350324. URL http://doi.wiley.com/10.1002/pssb.201350324.

[72] H. Yildirim, A. Kara, S. Durukanoglu, and T. S. Rahman. Calculated pre-exponential factors and energetics for adatom hopping on terraces and steps of Cu(100) and Cu(110). *Surface Science*, 600(2):484–492, January 2006. ISSN 00396028. doi: 10.1016/j.susc.2005.10.055. URL http://linkinghub.elsevier.com/retrieve/pii/S0039602805012422.

[73] N. Nita, R. Schaeublin, and M. Victoria. Impact of irradiation on the microstructure of nanocrystalline materials. *Journal of Nuclear Materials*, 329-333:953–957, August 2004. ISSN 00223115. doi: 10.1016/j.jnucmat.2004.04.058. URL http://linkinghub.elsevier.com/retrieve/pii/S0022311504002004.

[74] G. J. Ackland, K. DMellow, S.L. Daraszewicz, D.J. Hepburn, M. Uhrin, and K. Stratford. The MOLDY short-range molecular dynamics package. *Computer Physics Communications*, 182(12):2587–2604, December 2011. ISSN 00104655. doi: 10.1016/j.cpc.2011.07.014. URL http://linkinghub.elsevier.com/retrieve/pii/S001046551100261X.

[75] M. W. Finnis and J. E. Sinclair. A simple empirical N -body potential for transition metals. *Philosophical Magazine A*, 50(1):45–55, July 1984. ISSN 0141-8610. doi: 10.1080/01418618408244210. URL http://www.tandfonline.com/doi/abs/10.1080/01418618408244210.

[76] O. Hardouin Duparc. On the origins of the Finnis Sinclair potentials. *Philosophical Magazine*, 89(34-36):3117–3131, December 2009. ISSN 1478-6435. doi: 10.1080/14786430903292423. URL http://www.tandfonline.com/doi/abs/10.1080/14786430903292423.

[77] G. J. Ackland, G. Tichy, V. Vitek, and M. W. Finnis. Simple N -body potentials for the noble metals and nickel. *Philosophical Magazine A*, 56(6):735–756, December 1987. ISSN 0141-8610. doi: 10.1080/01418618708204485. URL http://www.tandfonline.com/doi/abs/10.1080/01418618708204485.

[78] W. E. Wallace and G. J. Ackland. Calculated energies and relaxations of the low-index planes of ordered Cu3Au. *Surface Science*, 275(1-2):L685–L690, September 1992. ISSN 00396028. doi: 10.1016/0039-6028(92)90642-J. URL http://linkinghub.elsevier.com/retrieve/pii/003960289290642J.

[79] A. J. E. Foreman, C. A. English, and W. J. Phythian. Molecular dynamics calculations of displacement threshold energies and replacement collision sequences in copper using a many-body potential. *Philosophical Magazine A*, 66(5):655–669, November 1992. ISSN 0141-8610. doi: 10.1080/01418619208201583. URL http://www.tandfonline.com/doi/abs/10.1080/01418619208201583.

[80] ImageJ. URL http://imagej.nih.gov/ij/.

[81] P. D. Lane. Unpublished work.

[82] K. Stahrenberg, T. Herrmann, N. Esser, J. Sahm, W. Richter, S. Hoffmann, and Ph. Hofmann. Surface-state contribution to the optical anisotropy of Ag(110) surfaces: A reflectance-anisotropy-spectroscopy and photoemission study. *Physical Review B*, 58(16):R10207–R10209, October 1998. ISSN 0163-1829. doi: 10.1103/PhysRevB.58.R10207. URL http://link.aps.org/doi/10.1103/PhysRevB.58.R10207.

[83] A. Damascelli. Probing the Electronic Structure of Complex Systems by ARPES. *Physica Scripta*, T109:61, 2004. ISSN 0031-8949. doi: 10.1238/Physica.Topical.109a00061. URL http://www.physica.org/xml/article.asp?article=t109a00061.xml.